Doctoral Dissertation

博士学位論文

Study on the control of vortex pinning in high-T_c bulk cuprates

高温超電導バルク銅酸化物の磁束ピン止め制御に関する研究

September 2013

平成 25 年度

Graduate School of Marine Science and Technology

Tokyo University of Marine Science and Technology

Doctoral Course of Applied Marine Environmental Studies

東京海洋大学大学院

海洋科学技術研究科

応用環境システム学専攻

Beizhan LI

李　備　戦

CONTENTS

Abstract

We focus on immobilizing magnetic vortices in type-II superconductor — a problem that has plagued scientists trying to engineer real-world applications for decades. The key original finding is that we discovered a method to stabilize magnetic vortices in a wide range of magnetic fields by creating a geometric pinning landscape, i.e. the grid-like nanowalls, in the melt-textured Gd-Ba-Cu-O bulk superconductor. This discovery favor to promotion of the large-scale applications of high temperature superconductors as well as the understanding of the "vortex lattice/pinning landscape" puzzle. Following this key original finding, other fundamental findings include: (1) clarified for the first time two key factors that serve the peak effect; (2) proposed and proved for the first time an efficient in-field pinning model; (3) found for the first time the complementary melting growth and was summarized as the two-steps solidification; (4) proposed and proved a recrystallization mechanism for achieving nano-sized inclusions; (5) clarified the pinning mechanism of the additions of $BaTiO_3$, TiO_2 and BaO_2; (6) found a new efficient dilute addition of ferroelectric $BaTiO_3$; (7) proposed a scenario of how to explain the evolutions of peak effect both in changed magnetic fields and temperatures; (8) found a method on the control of the trapped flux profile; (9) clarified the key factors in making of hybrid magnet with bulks and tapes. The arrangement of this thesis is as follows.

In **chapter 1**, a brief review of the development of superconductivity was given which includes several basic relevant theories and materials. In particular, theories and considerations relevant to the vortex pinning were summarized which include what is the vortex pinning, how to trap vortices, types of vortex pinning as well as current development on the control of vortex pinning. The basic relationship between current-carrying ability and vortex pinning was given. The peak effect was discussed too. We also summarized the development of the melt processing techniques. A prototype application of the type-II superconductor was described based on the bulk HTS synchronous motor made by our laboratory. Last, the motivation of the present work was given.

In **chapter 2**, characterizations techniques such as SQUID, SEM, TG-DTA, XRD, etc were summarized briefly. Synthesis methods of the relevant materials and general process of the top seeded melt growth were described. We also explored the optimal growth parameters involved in both hot and cold seeding method. Especially, we found a method on the control of the trapped flux profile.

In **chapter 3**, the detailed dilute addition effect of $BaTiO_3$ was discussed. Interestingly, two optimized doping levels were found: one is 0.1 mol.% and the other is 0.3 mol.%. These two doping levels show different pinning behaviours. The possible pinning mechanisms were discussed. We proposed a view point that the composition of the doping related precipitations change with changing of growth conditions as well as doping levels.

In **chapter 4**, the detailed dilute doping effect of TiO_2 was described first. Then a comparative study was performed by employing the additions of $BaTiO_3$, TiO_2 and BaO_2, by which a recrystallization of fine inclusions was proposed. Further, based on the aligned peaks in the $J_c - B$ diagram, the hypothesis of the possible geometrical arrangements of fine inclusions was proposed and discussed which was confirmed by the direct observation of the microstructure described in chapter 5. Issues related to in-field pinning were discussed.

In **chapter 5**, we put the "vortex lattice/pinning landscape" puzzle boils down to the task of "stabilizing tunable vortex lattice with only one pinning landscape" and proposed that the most effective pinning may arise from the geometrical arrangement of superconducting defects. The three dimensional one should be arranged semi-continuously in some way. The present understanding of the vortex pinning posed by the three dimensional geometric defect array is never achieved in type-II superconductor whether in bulks, tapes or wires. We obtained for the first time a semi-continuous geometric pinning landscape, i.e. the grid-like nanowalls, which were achieved by inserting nanoparticles into the neatly arranged grain boundaries in textured Gd-Ba-Cu-O bulk superconductor. In contrast to the sharp peaks in the critical current posed by the simple defect array in thin film, strikingly enhanced critical current sustained by nanowalls has been achieved in a wide range of magnetic fields since the grid-like nanowall provides variable spatial periodicities for matching with the variable vortex lattice induced by external fields. This finding highlights the key parameters on the control of vortex pinning in high magnetic field. The present grid-like nanowalls shows great potentials on boosting the large-scale applications of high-T_c superconductor. Another original finding is that we discovered a method of making geometric defect array by exploiting the detailed ripening process of sub-grains, which can be summarized as the "two-steps solidification" procedure. Thanks to the addition of $BaTiO_3$, inserting nanoparticles into GBs has been achieved elaborately in the second step of the "two-steps solidification" procedure.

In **chapter 6**, superimposed effect of bulks and tapes was studied. Key factors involved in the hybrid magnet assembled with bulks and tapes were clarified. The possible practical strategies on the improvement of trapped flux as well as thermal conductance were discussed.

In **chapter 7**, we give a summary of the main findings of this thesis. Possible future perspectives for promotion of current-carrying ability were discussed.

Our study opens a new perspective on engineering of pinning landscape and provides a new basis on the control of vortex pinning. We believe that our contribution will be benefit to boost the large-scale applications of type-II superconductor.

Chapter 1 Introduction

1.1 Historical review

1.1.1 The superconducting materials

Superconductivity was first discovered by H. K. Onnes in 1911. He observed that when mercury was cooled below a critical temperature (T_c), the resistivity of mercury was reduced to zero [1]. He was able to observe this phenomenon because three years earlier he had discovered a method to liquefy helium, allowing him to study materials at very low temperatures. Mercury has a critical temperature of about 4 Kelvin, making the liquefaction of helium very important to this discovery. In the following years, many other elements and alloys were also shown to be superconducting, but the transition temperatures (T_c's) of these materials were all very low (well below 30 K).

In 1986, the cuprate superconductors were discovered by Bednorz and Muller [2]. These materials were not alloys but rather layered perovskite-related cupric oxide materials. The initial material that they discovered was lanthanum barium copper oxide with a critical temperature of 35 K. Within a year, many more materials had been discovered, many of which had critical temperatures above 77 K (which is technologically important due to it being the normal boiling point temperature of liquid nitrogen). Later in 2008 iron-based superconductors were discovered [3].

The material studied in this dissertation was the layered perovskite-related cupric oxide, Gd-Ba-Cu-O, one of the family of RE-Ba-Cu-O materials. We will specifically study the textured bulk superconductors, many of which have magnet applications. Top seeded melt growth (TSMG) technique as well as hot/cold seeding method were employed to process the well textured samples.

1.1.2 Meissner effect

In 1933, W. Meissner and R. Ochsenfeld discovered that a superconductor is fundamentally different from a perfect conductor. Their discovery can be succinctly stated as a superconductor will expel weak magnetic fields even if the magnetic field is static [4]. In 1935 the London brothers proposed a set of equations that theoretically explain the Meissner effect [5]. Equations 1.1 and 1.2 are the relations that the London brothers developed to describe this phenomenon.

$$\frac{dJ}{dt} = \frac{n_s e^2}{m} E \tag{1.1}$$

$$\Delta \times J = \frac{n_s e^2}{mc} B \tag{1.2}$$

Using equation 1.2 and Maxwell's equations, one can isolate the magnetic field *B* and solve a simple differential equation to understand how *B* varies in the sample. Equation 1.3 shows the differential equation and equation 1.4 is the solution for the simple geometry of

a semi-infinite slab with its surface at $x = 0$ in the presence of a magnetic field applied parallel to the surface.

$$\vec{B} = -c\vec{\Delta} \times \vec{\Delta}\frac{4\pi n_s e^2}{mc^2}\vec{B} \;\rightarrow\; \Delta^2 B = \frac{1}{\lambda^2}B \tag{1.3}$$

$$B(x) = Be^{-\lambda x} \tag{1.4}$$

In equations 1.3 and 1.4, λ is a constant, called the London penetration depth, defined as $\lambda = \sqrt{mc^2/4\pi n_s e^2}$ and x is the distance into the superconductor. The flux density within the superconductor vanishes exponentially fast with distance, even if the external magnetic field is constant; this result is consistent with the experimentally observed Meissner effect.

1.1.3 Ginzburg-Landau theory

In 1950, Lev Landau and Vitaly Ginzburg developed a phenomenological macroscopic model in an effort to study superconductivity by using the theory of second order phase transitions [6]. This theory, known as Ginzburg-Landau theory of superconductivity (or GL theory), proposed a complex pseudo-wavefunction ψ that acts as the order parameter and is formulated such that where n_s is the number density of superconducting electrons.

Near T_c, the free energy of the superconductor can be expanded in a power series as a function $|\psi|^2$. Assuming that ψ is varying slowly in space, the free energy near T_c can be written as equation 1.5.

$$f_s = f_n + \alpha|\psi|^2 + \frac{\beta}{2}|\psi|^4 + \frac{1}{2m^*}\left|\left(\frac{\hbar}{i}\nabla - e^*\vec{A}\right)\psi\right|^2 + \frac{H^2}{8\pi} \tag{1.5}$$

In the absence of fields and gradients (the spatially uniform case), equation 1.5 reduces to equation 1.6.

$$f_s - f_n = \alpha|\psi|^2 + \frac{\beta}{2}|\psi|^4 \tag{1.6}$$

If one minimizes equation 1.6 with respect to $|\psi|^2$, one obtains the condensation energy as seen in equation 1.7.

$$f_s - f_n = \frac{\alpha^2}{2\beta} = -\frac{H_c^2}{8\pi} \tag{1.7}$$

In equation 1.7, H_c is the thermodynamic critical field. Ginzburg and Landau then minimized the more general free energy using a variational principle and derived a differential equation for ψ and a corresponding equation for the supercurrent density J. These are described in equations 1.8 and 1.9, respectively.

$$\alpha\psi + \frac{\beta}{2}|\psi|^2\psi + \frac{1}{2m^*}\left(\frac{\hbar}{i}\nabla - e^*\vec{A}\right)^2\psi = 0 \tag{1.8}$$

$$\vec{J} = \frac{e^*\hbar}{2m^* i}(\psi^*\nabla\psi - \psi\nabla\psi^*) - \frac{e^{*2}}{m^* c}|\psi|^2\vec{A} \tag{1.9}$$

GL theory also introduces two new length scales. The first length scale is the coherence length ξ. The coherence length is the characteristic length over which ψ can vary without large energy increases and equation 1.10 is how it is defined.

$$\xi(T) = \frac{\hbar}{|2m^*\alpha(T)|^{1/2}} \tag{1.10}$$

They also defined a new temperature dependent penetration depth $\lambda(T)$ which is logically consistent with the more phenomenological length scale introduced by the London brothers and is defined in equation 1.11.

$$\lambda(T) = \sqrt{\frac{m^*c^2}{16\pi e^{*2}\psi_0^2}} \tag{1.11}$$

Since, $\xi(T)$ and $\lambda(T)$ diverge in the same way as T_c is approached, one can define the GL parameter κ that is dimensionless and approximately temperature independent. This parameter is defined as the ratio of the penetration depth and coherence depth $\kappa = \frac{\lambda(T)}{\xi(T)}$.

By means of this new parameter, it is convenient to classify the types of superconducting materials which allow one to make clear the fundamental basis that account for the current-carrying performance. In addition, by classifying the types of superconductors, one could find what the advantages of each are for the practical applications. In the following section, we give a brief review of these considerations.

1.2 Theory elements

1.2.1 Type-I and type-II superconductivity

The Ginzburg Landau parameter κ will define two fundamentally different types of superconductivity, type-I and type-II, depending on the sign of the normal-superconducting (n-s) interface energy. This classification was first achieved by Abrikosov. The difference between the two types of superconductors is their behavior in the presence of a magnetic field. In small magnetic fields, both type-I and type-II superconductors have a Meissner state behavior, but in the presence of large magnetic fields, type-II superconductor allows flux to enter as quantized vortices [7]. The reason is that type-II superconductors are characterized by a mixed state consisting of superconducting regions encircling normal filaments containing one quantum of magnetic vortex which form a triangular vortex lattice.

A type-I superconductor is one in which the Ginzburg Landau parameter is $\kappa < \frac{1}{\sqrt{2}}$, corresponding to the positive n-s interface energy. A type-I superconductor, in the presence a magnetic field, will have a Meissner state up to the thermodynamic critical magnetic

field H_c. Above this magnetic field, the superconductor is driven into its normal state. This provides a temperature-magnetic field phase space in which the material is either in a superconducting Meissner state or a normal state. This is qualitatively shown in figure 1-1a.

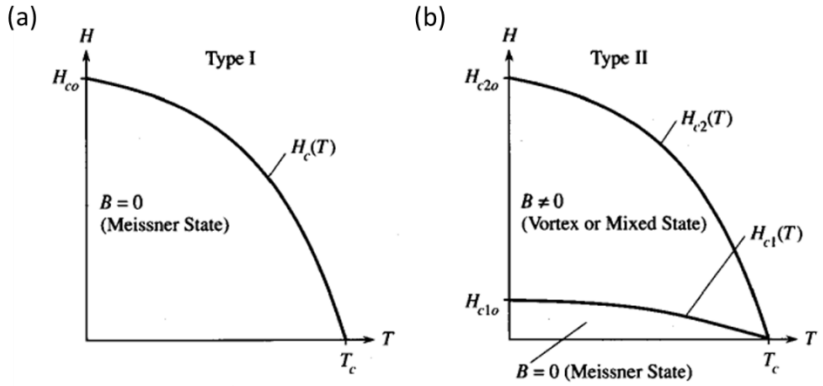

Figure 1-1 (a) Shows a type-I superconductor with only a Meissner state and a normal state. (b) Shows a type-II superconductor that has a Meissner state below H_{c1} and a mixed or vortex state above H_{c1} and below H_{c2} and a normal state above H_{c2}.

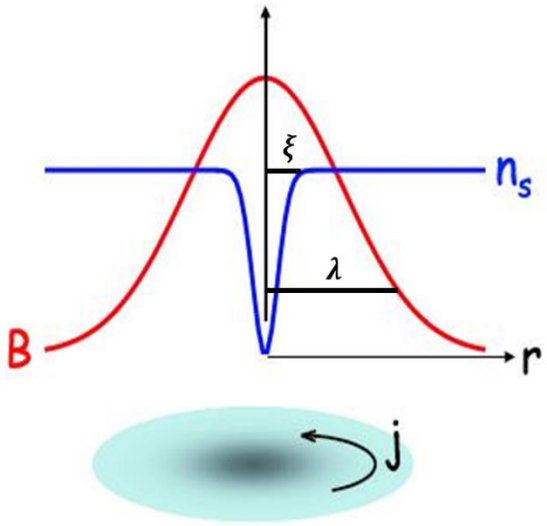

Figure 1-2 Abrikosov-vortex: sketch of magnetic field B(r) and carrier density n_s of an isolated vortex line.

Table 1-1 critical parameters of various superconductors

Superconductor		T_c	$\mu_0 H_c(0)$	$\mu_0 H_{c1}(0)$	$\mu_0 H_{c2}(0)$
		(K)	(mT)	(mT)	(T)
Type-I	Hg (α)	4.15	41		
	In	3.41	28		
	Pb	7.20	80		
	Ta	4.74	83		
Type-II	Nb	9.25	199	174	0.404
	$Nb_{37}Ti_{63}$	9.08	253		15
	Nb_3Sn	18.3	530		29
	Nb_3Al	18.6			33
	Nb_3Ge	23.2			38
	V_3Ga	16.5	630		27
	V_3Si	16.9	610		25
	$PbMo_6S_8$	15.3			60
	MgB_2	39	660		
	$YBa_2Cu_3O_7$	93	1270		
	$(Bi,Pb)_2Sr_2Ca_2Cu_3O_x$	110			
	$Ti_2Ba_2Ca_2Cu_3O_x$	127			
	$HgBa_2CaCu_2O_x$	128	700		
	$HgBa_2Ca_2Cu_2O_x$	138	820		

When the Ginzburg Landau parameter is $\kappa > \frac{1}{\sqrt{2}}$, which corresponds to the negative n-s interface energy, the superconductor is a type-II material. A type-II superconductor has a more complicated temperature-magnetic field phase space as can be seen in figure 1-1b. Again for small applied magnetic fields the superconductor is in a Meissner state. Above the lower critical field, H_{c1}, magnetic flux begins to enter the superconductor. This state is known as the mixed state or vortex state. The magnetic flux enters the superconductor as quantized vortices where the flux quantum is $\Phi_0 = \frac{h}{2e} = 2.07 \times 10^{-7} \mathrm{Oe} \cdot \mathrm{cm}^2$. The vortex has currents circulating in a profile with a radius of order λ and a core that is of order ξ in radius. Figure 1-2 shows a sketch of an isolated vortex.

The superconducting parameters of various superconductors are listed in Table 1-1. Here H_c in type-II superconductors is the thermodynamic critical field, since H_{c1} and H_{c2} are significantly depending on the direction of magnetic field with respect to the crystal axes, the doping state of carriers and the electron mean free path, only the value of H_c in the optimally doped state is given in the table. In this thesis, type-II superconductors will be studied exclusively.

1.2.2 Vortex motion

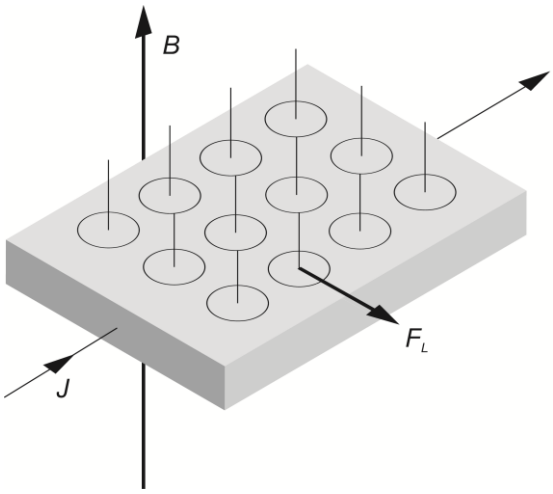

Figure 1-3 Schematic showing relevant vector directions for a type-II superconductor in the mixed state in the presence of an applied magnetic field.

Vortices will enter the superconductor and form a lattice of magnetic flux [8], assuming only intervortex interactions are important. In the presence of an imposed electric current density *J*, the Lorentz force density ($F_L = J \times B$) will cause the vortices to move at velocity *v* that is limited by the effective viscous drag in the superconductor. This vortex motion will induce an electric field as can be seen in equation 1.12.

$$\vec{E} = -\vec{v} \times \vec{B} \tag{1.12}$$

The vortex motion will be perpendicular to the current density and the magnetic field as is depicted in figure 1-3, meaning that ***E*** is parallel to ***J***. Once an electric field is induced, a power loss per unit volume will exist as shown in equation 1.13.

$$P = \vec{E} \cdot \vec{J} \tag{1.13}$$

This power loss is due to the motion of the vortices. If it is possible to reduce the velocity of the vortices by pinning them in place, then the power dissipation will be reduced. To achieve this, one must create potential barriers that keep the vortex motion to a minimum.

1.2.3 Vortex pinning

The first flux that enters a type-II superconductor enters as a single vortex. As the applied field increases, so does the number of vortices. As long as the spacing of the vortices is large compared to the penetration depth it is possible to ignore vortex-vortex interactions. When these conditions are met, the free energy per unit length for the vortex line (ϵ_1) is given by equation 1.14 [9].

$$\epsilon_1 \approx \left(\frac{\Phi_0}{4\pi\lambda}\right)^2 \ln\left(\kappa + {}^1/_2\right) = \frac{H_C^2}{8\pi}\xi^2 \ln\left(\kappa + {}^1/_2\right) \qquad (1.14)$$

Equation 1.14 relates the free energy of the vortex line to the square of the coherence length. This relation implies that defects in superconductors that are not superconducting present an energetically favorable position and can pin the vortex (by regaining the vortex core energy). There are many different types of pinning, but fundamentally they all provide an energetic barrier to prevent the vortex motion.

The motion of a vortex experiencing a Lorentz force is the origin of the dissipation in superconductors. To minimize this dissipation, a pinning force density, F_P as seen in equation 1.15, where d is the size of a non-superconducting particle, must exist that is at least equal to the Lorentz force. When the applied force is equal to the maximum available pinning force, the current density producing that force is the critical current density (J_c). The pinning force density is an important parameter and is related to the critical current density as seen in equation 1.16. [10]

$$F_P = \frac{H_c^2}{2\mu_0}\pi\xi d \qquad (1.15)$$

$$J_c \equiv {}^{F_P}/_B \qquad (1.16)$$

The practical critical current density in commercial superconducting materials is determined by this flux pinning mechanism. This implies that this J_c is not an intrinsic property but is an acquired property determined by the macroscopic structure of introduced defects. That is, the critical current density depends on the density, type of, and arrangement of pinning centers. It is necessary to increase the flux pinning strength in order to increase the critical current density. The depairing current sets the highest J_c value, if it is lower than the required level, the system cannot be used for practical applications. For example, YBCO has a H_c value of 2.4×10^5 A/m (B_c of 0.3 T) and λ of 10^{-7} m at 77 K, which gives an ideal J_c value to be 2.4×10^8 A/cm^2, three orders of magnitude larger than the required values, indicating that YBCO superconductors have intrinsically a high potential in J_c value. In the following sections, the critical current under more practical conditions is introduced.

1.2.4 Types of pinning

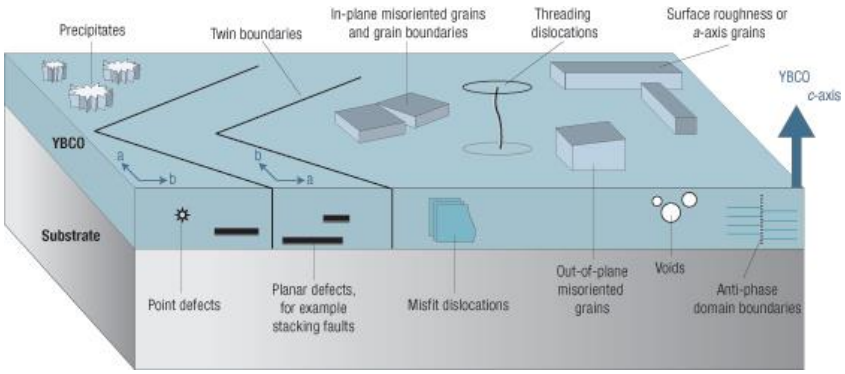

Figure 1-4 Many thin-film defects have been proposed as flux pinning sites in YBCO; anything that locally disturbs the crystalline perfection over a scale of 0.1–1 nm is a candidate. Strain fields associated with defects may also pin vortices. The challenges in engineering defect structures for the best performance are to determine which ones are beneficial, and to tailor their density to produce the desired effect without obstructing current [15].

Vortices can be pinned in many ways. Starting with equation 1.14, if a superconductor is anisotropic there will be intrinsic pinning because it is inversely proportional to the square root of effective mass of the electrons, which will be discussed further in the next section. Secondly, nonsuperconducting material can be introduced into the superconducting matrix by various means to pin the vortices. For example, superconducting materials have been irradiated by energetic heavy ions; this generates columnar pinning sites as the radiation penetrates the sample producing amorphous tracks that increase pinning and decrease flux creep [11]. Also the presence of this type of defects has been shown to increase the irreversibility line, which is also evidence of increased pinning [12]. More recently, microscopic nonsuperconducting regions have been formed in the superconductor during the synthesis process, e.g., as second phase precipitations or strain fields. This allowed one to introduce columnar or isotropic pinning sites to even large scale processes [13,14]. We found that the boundaries between misaligned crystal-grains are important pinning medium which poses generally deep pinning potentials if the boundaries are oriented parallel to the c axis because vortex line can be regulated along the c axis. Figure 1-4 summarized varieties of defects appeared in YBCO thin films.

1.2.4.1 Intrinsic pinning

The layered oxide materials have strong superconductivity in the CuO planes and are weakly linked in the *c* direction. The layered nature of these materials is illustrated in figure 1-5. If a magnetic field is applied in the *ab* plane, the vortices will try to form in the layered structure. In this direction the superconducting order parameter is modulated by the layered crystal structure, as well as the condensation energy. A Lorentz force in the *c*-direction would try to force the vortices to move from *ab* plane to *ab* plane, which is much more difficult, making the intrinsic anisotropy a powerful pinning force in cuprates [9].

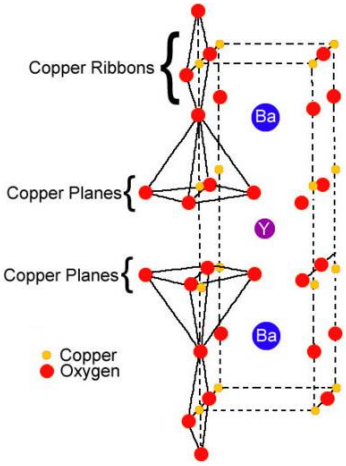

Figure 1-5 A schematic figure of the structure of YBCO. There is strong superconductivity in the CuO planes and weak coupling between CuO-CuO planes.

1.2.4.2 Extrinsic pinning

In spite of the varieties of defect indicated in figure 1-4, columnar defect provides the strongest pinning potential so far. Heavy ion irradiated high T_c cuprates were the first samples with extrinsic columnar strong pinning centers. These studies showed the possibility of strong extrinsic pinning centers with a "tailored" geometry. If one were to consider the angular critical current density of a sample with linear columns created by heavy ion irradiation, it would be angularly selective. There would be a peak in the current density when the applied magnetic field is aligned with the column-like pins. When this condition is met, the vortex is most optimally pinned by pinning the whole length of the vortex.

Later, defects were engineered by introducing oxide materials and second phase rare earth oxides that will act as pinning centers. Different materials will form isotropic pins and others will form correlated disorder such as columns. Adding second phase rare earth oxides will introduce large isotropic pins centers that produce strong pinning. Consequently pins of an isotropic nature will add no extra angular dependence, meaning

that the electronic anisotropy determines the angular profile. Adding other materials such as $BaSnO_3$ or $BaZrO_3$ can create columnar defects. These pinning centers will have angularly selective pinning. This allows one to synthesize a material that is either dominated by isotropic pinning or correlated disorder or a mixture of both. This should produce many unique and interesting properties in the pinning landscape.

In this thesis, we further extend the scope of artificial pinning landscape by making for the first time the geometrical arrangement of nanoparticles in the melt-processed high T_c bulk cuprates. This finding is important. Scientists have spent a lot of time and effort over the past few decades trying to immobilize these vortices, but until now, the results have been mixed. They found ways to pin down the vortices, but these only worked in a restricted range of temperatures and magnetic fields due to finite pinning potentials posed by certain defects. Restricted by material processing technology, major results fall in random defect except making of the simple two-dimensional defect array in thin film. The concept that critical current may be higher if various types of defect act simultaneously is not necessarily correct. Indeed, random and correlated disorders produce rather opposite effects on the vortex topology and dynamics. The former promotes wandering and entanglement, whereas the latter promotes transverse localization. Then the object is not just adding more pinning centers but using the existing ones more effectively. The new paradigm is no longer a simple, 'one vortex/one defect' challenge, but a "vortex lattice/pinning landscape" puzzle. This will be discussed in detail in chapter 5.

1.3 Critical currents

J_c is one of the most important properties for engineering applications of superconductors. Hence one should know what determines J_c values.

1.3.1 Type-I superconductors

In general, before reaching the ideal critical current, the superconductor becomes normal due to the magnetic field (H_i) generated by the applied current (I). H_i at the surface of the wire is given by $H_i = \frac{I}{2\pi r}$, where r is the radius of the wire. When H_i exceeds H_c, the superconducting state is destroyed. The critical current (I_c) is then obtained by $I_c = 2\pi r H_c$. Thus, $J_c = \frac{I_c}{\pi r^2} = \frac{2H_c}{r}$. This indicates that in order to achieve despairing current, we need to reduce the radius of the superconductor down to 2λ, which is much smaller than the radius of practical wires. The ideal critical current density is realized only in thin film or extremely small sized wire, where the thickness is small than λ and is much higher than engineering critical current densities.

1.3.2 Type-II superconductors (case study for Y_2BaCuO_5 inclusions in YBCO)

As the case study for pinning calculation, we treat the melt-textured YBCO in which Y_2BaCuO_5 (Y211) inclusions are finely distributed. Assume that YBCO matrix contains the number, N_p, of Y211 per unit volume and d in size. Then the number of interactions N per unit volume is $N = N_p \frac{d}{a_f}$, where a_f is the spatial periodicity of the vortex line arrangement. a_f is a function of magnetic field (B) and is given by $a_f = 1.075\sqrt{\frac{\Phi_0}{B}} \cong \sqrt{\frac{\Phi_0}{B}}$. In the case of pinning by a large normal conducting particle, F_p is given by equation 1.15. From equation 1.16, J_c is obtained as 1.17.

$$J_c = \frac{NF_P}{B} = \frac{N_P B_c^2}{2\mu_0 B a_f}\pi\xi d^2 = \frac{\pi\xi B_c^2}{2\mu_0\sqrt{\Phi_0}} \cdot \frac{N_p d^2}{\sqrt{B}} \qquad (1.17)$$

At high fields, this equation becomes as 1.18.

$$J_c = \frac{\pi\xi B_c^2}{2\mu_0\sqrt{\Phi_0}} \cdot \frac{N_p d^2}{\sqrt{B}}\left(1 - \frac{B}{B_{c2}}\right) \qquad (1.18)$$

This relation suggests that J_c is proportional to $N_p d^2$, if the Y211 inclusions are dominant pinning centers. $N_p d^2$ corresponds to V_f/d, where V_f is the volume fraction of the Y211 and equal to $N_p d^3$.

It is possible to vary the volume fraction and the average grain size of Y211 inclusions trapped in the YBCO matrix by changing processing conditions in melt processing. It is clear that J_c is proportional to V_f/d, which supports the fact that the n - s interface provides vortex pinning. To improve J_c one also need to reduce the size of the Y211 inclusions.

To this step, the basic relationship between critical current and vortex pinning has been discussed by calculation based on the very simple pinning scenario with normal conducting inclusions only. These normal conducting inclusions are mainly contributed to the critical current in low magnetic field. Shown in figure 1-4 indicates that pinning situations in real material are much complex. Achieving high critical currents in a wide range of magnetic fields is more important for practical applications such as high-field magnets storing large amounts of energy. One noteworthy phenomenon is the peak effect appeared in critical current. We summarize the possible factors that given contributions to the improvement of in-field pinning in the next paragraph.

1.3.3 Peak effect

From a variety of magnetic measurements on 123-based and Bi-based high-T_c superconductors, a general flux pinning diagram was deduced, showing the interplay of the two basic pinning mechanisms, δl- and δT_c-pinning. The δl-pinning mechanism is due to fluctuations of the carrier men free path, which could be induced by the crystalline defects or normal conducting secondary phases and results in the enhancement of J_c in low field regions. The δT_c-pinning is provided by fluctuations of the transition temperature and results in the enhancement of J_c in high field regions (peak effect) [9]. The δT_c-pinning can be provided by a variety of defects; the weakest one of these is the simple oxygen vacancies. Nd/Ba substitution is proved to be stronger source of the δT_c-pinning. Another possible source for the δT_c-pinning is intergrowths of *e.g.* Bi-2201 in Bi-2212 [16]. A common feature is that peak effect is always companied with the reduced transition temperature. Therefore, the formation of the clustered weak superconducting regions in the superconducting matrix becomes a key factor for the appearance of peak effect. The pinning mechanisms behind the peak effect are hitherto mixed and are still wrapped in mystery. One reason is that the significant factor of anisotropic crystal growth was usually ignored by scientists. We proposed that the geometrical arrangement of the clustered superconducting regions originated from anisotropic crystal growth helps to meet the requirement of matching effect occurred between vortex lattices and pinning landscape.

This is the key subject of this thesis. To achieve the geometrical arranged weak superconducting regions in bulk samples, one good way is to make the melt-textured bulk samples. We first give a review of advances of the melt processing techniques developed in the past two decades in the following sections, from which one can obtain an overall scenario on exploring the practical ways for achieving high critical currents by means of the controlled vortex pinning. One would learn that it is really a very complex task since much parameter will be involved in this complex bulk system, for instance the composition of the precursor, varieties of additions, the average size of the starting powders, the growth temperature profiles, etc. The final result highly depends on the optimization of combinations of these parameters. It is also a tantalized task to make clear the varieties of pinning mechanisms that hiding behind the J_c-B diagrams.

1.4 Melt processing of high-T_c cuprates

Polycrystalline samples form mixed crystal grains. Grain boundaries with large misorientations impede the paths of supercurrent, i.e. form weak-links, even when they are free from segregation. Therefore, the first step is to find ways to align those crystal grains into aligned grain arrays with low misorientations. A practical fabrication technique is to produce single domain with well textured microstructure which is desirable for achieving high J_c values basically. Melt-textured superconductors are proved to meet such requirement. A pioneering accomplishment was first made by Jin *et al* with a solidification technique for the YBCO system, known as melt-textured growth as described in the following texts.

1.4.1 Melt-textured growth

Jin *et al.* developed a melt-textured growth (MTG) technique [17]. Schematic illustration of temperature profile of the MTG process is shown in figure 1-6 [18,19].

By using this technique YBCO sample can be well textured. During the cooling stage, preferred grain growth is in the *a-b* plane and thus the grains are aligned into sub-grain arrays with low angles closed to 0 °. Weak links formed by grain boundaries are suppressed. J_c values of ~10^4 A/cm^2 are achieved at 77 K in self-field.

There is a series of complex reactions during the melt-textured process. Figure 1-7 shows quasi-ternary [20] and binary phase diagrams [21,22] of Y-Ba-Cu-O system. Most RE123 systems have the similar phase diagrams as Y123. The complex reactions can be described as follows [23, 24].

Heat the sample to around 1000 ℃, $YBa_2Cu_3O_7$ start to decompose according to the equation 1.19.

$$YBa_2Cu_3O_7 \rightarrow Y_2BaCuO_5 + Ba_3Cu_5O_8 \text{ (Liquid)} \quad (1.19)$$

When the temperature higher than 1300 ℃, the Y211 phase is not stable and decomposes further by the incongruent melting 1.20.

$$Y_2BaCuO_5 \rightarrow Y_2O_3 + \text{Liq (BaO+CuO)} \quad (1.20)$$

During the cooling process, the above mentioned peritectic reactions are reversed. Below 1250 ℃, Y_2O_3 plus liquid (BaO and CuO) convert into Y_2BaCuO_5 according to equation 1.21.

$$Y_2O_3 + \text{Liq (BaO+CuO)} \rightarrow Y_2BaCuO_5 \quad (1.21)$$

When the sample is cooled to around 1000 ^oC, the second peritectic solidification occurred as equation 1.22.

$$Y_2BaCuO_5 + \text{Liq } (3BaCuO_2+2CuO) \rightarrow 2\ YBa_2Cu_3O_x \quad (1.22)$$

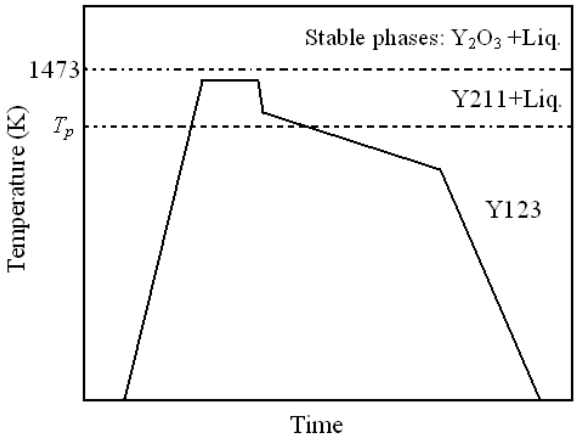

Figure 1-6 Schematic illustration of the modified MTG process [18].

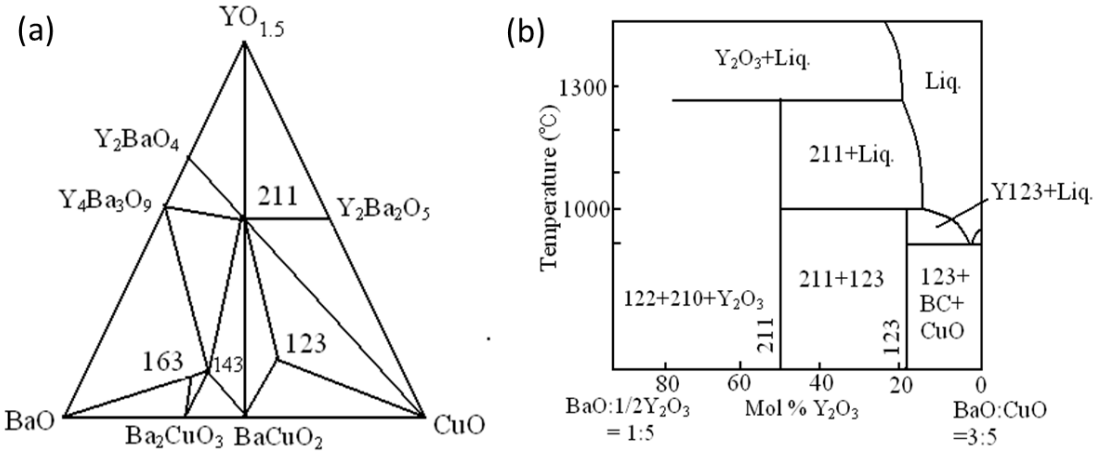

Figure 1-7 Phase diagrams for Y-Ba-Cu-O, (a) is Quasi-ternary, (b) is quasi-binary [20-22].

The final sample consists of oriented Y123 grains and randomly distributed Y211 particles. Subsequently, remarkable progress in melt processing techniques has been made for the YBCO system through modifications of the processing parameters such as by introducing the secondary phases of RE-211, RE-2411, Ag, Pt, etc. With a nondirectional solidification method, mainly by modifying the phases of the starting materials and the thermal schedule for the solidification, the liquid-phase (LP) process [25], quenched and melt growth (QMG) process [26] and melt powder-melt growth (MPMG) process [27] have been developed in succession. In Particular, large repulsive and attractive forces between Fe-Nd-B magnets and MPMG-processed YBCO bulks made it possible to develop prototype devices such as a superconducting magnetic bearing and flywheel, and also to consider various monolithic bulk applications. Melt-textured technique opened a gate for promoting the large-scale applications of bulk high-T_c cuprates and also provided a route for the study of vortex pinning in a bulk system.

1.4.2 Quench and melt growth process

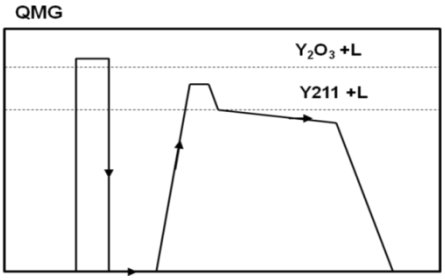

Figure 1-8 Schematic illustration of the QMG process.

After solving the misorientations of crystal grains, scientist hopes to find proper secondary phases for achieving effective pinning centers and recognized further that the distribution of the secondary phases is also the important factor to achieve high current-carrying ability. Then a quench and melt growth (QMG) process was proposed [26]. By means of QMG process, one could learn what the products are generated in the melting state and which kinds of phases are responsible for the vortex pinning after growth of the sample into crystal-like domains. In this way, we could find the possible key parameters for engineering efficient pinning centers with different kinds of additions. Such study has become a long-standing issue in the area of superconductivity. By quench the sample from high temperature 1300 ^{o}C – 1500 ^{o}C, light rear earth system commonly results in the 422 or 211 phase as the major solid phase while Y system only shows the Y_2O_3 phase. To date, those phases are still in the dominant position in REBCO bulk systems. Control the distribution of the secondary phase is another central issue of the melting process. The uniform distribution of fine Y211 particles is desirable in the final superconducting matrix. To date, there are two approaches to reach the Y211+L region. One is the decomposition of the Y123 phase, as in the case of the MTG process, and the other is the reaction of Y_2O_3. The melt MPMG/QMG process [26,27] shown in figure 1-8 is a route for control the distribution of the secondary phase. But the QMG process is not always necessary.

1.4.3 Powder melting process

Instead of using melt quenched powders, it is possible to use a mixture of Y_2O_3/$BaCuO_2$/CuO or a mixture of Y_2BaCuO_5/$BaCuO_2$/CuO as starting materials [28,29]. They are heated to the Y211 + L region and slowly cooled through the peritectic temperature as in the MTG or the final melt growth of the QMG process. The microstructure of the PMP processed samples is essentially identical to that of MTG processed samples, when these powders are heated slowly to the Y211 + L region, because they react and produce Y123 on the way and then decompose into Y211 + L. If very fine powders of Y_2O_3 or Y_2BaCuO_5 are prepared and heated quickly to the Y211 + L region, fine Y211 inclusions can be obtained.

1.4.4 Oxygen-controlled melt growth process

The ionic radii of the light rare earth (RE) elements, such as La, Nd, Sm, Eu and Gd, are close to that of Ba ion. These RE elements form $RE_{1+x}Ba_{2-x}Cu_3O_y$ type solid solutions (RE123ss) when fabricated by melt-textured process in air. With the ionic radius of RE^{3+} increases, the amount of RE substituting for Ba or the x value in $RE_{1+x}Ba_{2-x}Cu_3O_y$ increases. For example, x in $La_{1+x}Ba_{2-x}Cu_3O_y$ superconductors can be up to 0.7 while x in $Gd_{1+x}Ba_{2-x}Cu_3O_y$ usually reaches 0.2. RE123ss has inferior superconductivity compared to the stoichiometric RE123 due to low carrier concentration.

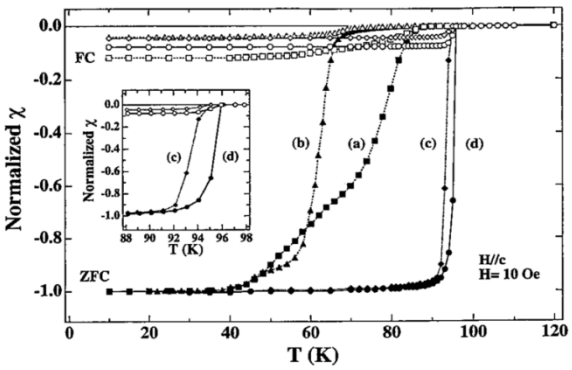

Figure 1-9 Susceptibility χ(T) of Nd-Ba-Cu-O samples melt processed in (a) O_2, (b) in air, (c) 1 % O_2 in Ar, (d) 0.1 % O_2 in Ar [31].

In 1993, Yoo et al. [30] reported that RE-Ba substitution could be largely suppressed when RE123 was fabricated in a reduced oxygen atmosphere, which is termed as oxygen controlled melt-growth (OCMG) process. The thermal profile has almost the same shape as modified MTG process. By OCMG process, one could obtain higher T_c with a sharp transition for RE123 superconductor than that for Y123. Figure 1-9 shows the effect of oxygen controlled during melt processing on the T_c for Nd123 [31]. It is obvious that a reduction of oxygen controlled is effective in increasing of T_c. For OCMG process, the most important factor is to control the oxygen content during the melt-process. However, high pinning performance achieved in air is essential from the viewpoint of the competitive low production cost for promoting the commercialization of RE123 bulk magnet.

OCMG process is effective for Nd, Sm and Eu system and even for any combinations of these three elements. All these OCMG-processed REBCO superconductors were promising since in addition to an enhanced transitions temperature of 94-96 K with sharp transition, they exhibit critical current densities larger than that of a well textured YBCO superconductor in a high-filed region at 77 K and for H//c. In LaBCO, both the onset T_c and the superconducting transition have also been greatly improved with decreased Po_2, but still not to the level of other REBCO superconductors. For GdBCO, however, the benefit of the OCMG process was very small because melt-growth samples in 1% O_2 + Ar showed no significant improvement compared with those processed in air [31]. That is why we select GdBCO as our subject material in this thesis.

1.5 Popular melt growth techniques

Nowadays in addition to optimize the growth conditions, exploring the proper secondary phases is being a main target and two main kinds of melt processes are adopted based on the peritectic reaction of (RE)BCO: one is the top seeded melt growth (TSMG) technique, and the other is the infiltration and growth (IG) process. Scientists hope to make clear what kind of addition can provide the strongest pinning potentials and what kind of parameter is the key for achieving the intensive vortex pinning and thus the high critical currents. During the improvement of melting process, the seeding technique has also been advanced to allow the so-called batch bulks process and the controlled multi-domain bulk growth. In the following sections, we review briefly these optimized techniques.

1.5.1 Top seeded melt growth technique

To well control the orientation of the textured crystal grain, a seed is generally used to nucleate the growth of a single domain. To enhance the mechanical property of superconducting matrix and suppress the coarsening of 211, introducing Ag_2O, Pt or CeO_2 in precursor is effective. Furthermore, introducing dilute additions can improve the pinning performance commonly further. The typical TSMG process is as follows. The starting materials of (RE)BCO, RE-211, Ag_2O, Pt or CeO_2, etc. are thoroughly mixed. The mixture is uniaxially pressed into a pellet. Generally, the Y-stabilized ZrO_2 rods are used to support the pellet. A seed is placed on the top surface of the pre-sintered pellet (hot seeding method) or placed there at room temperature before melt processing (cold seeding method) to nucleate the growth of a single domain. The single domains fabricated by optimized TSMG technique have been published is now up to diameters of 140 mm [32-34]. Recent result shows a diameter of 150mm with a homogeneous flux distribution and a trapped flux density of over 0.8 T at 87 K as shown in Fig. 1-10. They adopted a chemical gradient for achieving the gradient of melting point to meet with the long-time growth. It is worth to mention that hot seeding method is not convenient in process because of the action of opening the door of furnace in high temperature approximately 1040 ℃ and easy cause uncontrolled multi-domain due to opening process. Cold seeding method is mostly adopted currently for avoiding the disadvantages of hot seeding method.

Figure 1-10 The fabricated single domain bulks by employing TSMG technique. The large bulk has a diameter of 150mm. The small one has a diameter of 60mm. Inset illustrate the flux distribution in the large bulk. (Hidekazu Teshima, Nippon Steel, Japan)

1.5.2 Infiltration and growth technique

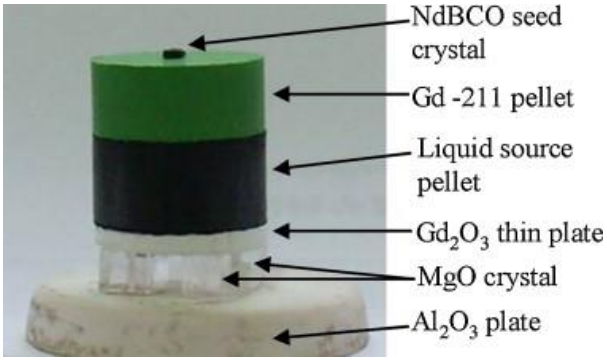

Figure 1-11Arrangement of the sample before infiltration and growth.

Infiltration and growth process involves the infiltration of liquid phases into a pellet of RE-211 and then react to form (RE)BCO below T_p. The arrangement of the two kinds of pellets, seed and supporters is shown in fig. 1-11. IG process allows near net shape fabrication with negligible shrinkage and distortion [35] , e.g. hollow cylinders [36], superconducting foams [37] and fabrics [38, 39]. The major advantages of the IG process contrasted to the TSMG process is the ability of the former provides fine sized spherical RE-211 precipitations in the (RE)BCO matrix, even without addition of compounds such as Pt and CeO_2 [40-42]. It makes the IG process attractive. With a modified IG process, the self-field J_c value is up to 230 kA/cm^2, and 10 kA/cm^2 up to 7 T at 77K in YBCO [43]. However, IG process has the disadvantages of uncertainties in the uniformity of microstructure and J_c [41]. There also has a chemical gradient and causes partially deformation of the sample pallet.

1.5.3 Seed techniques

For melting process, seed crystals or films are necessary for effective growth. The structure of the seed should have similar lattice parameters with RE-Ba-Cu-O superconductors and remains stable during the whole TSMG process. MgO single crystal is a good candidate at the beginning, which has a high melting point of 2800 ˚C, but a large lattice mismatch with (RE)BCO. NdBCO shows the highest melt point (1068 ˚C). NdBCO crystals are usually used as seeds to nucleate the growth of other (RE)BCO bulk superconductors [44]. Nevertheless, the members they could seed in the (RE)BCO are limited because T_p of NdBCO crystals are not high enough except using the hot seeding method [45]. Mg doped (> 0.5 wt%) NdBCO can raise its T_p by 20 ˚C [46], and is proper for seeding single domain growth especially by using a hot seeding method. Recently, a superheating phenomenon was found in films of (RE)BCO/substrate (substrate = MgO, $LaAlO_3$ or $SrTiO_3$). The film can endure a higher temperature then the corresponding single crystal. Yao et al. reported that Nd-123/MgO film has a superheating upper limit at about 1098 ˚C [47]. Xu et al. found that the YBCO buffered Nd-123/YBCO/MgO film can endure a high temperature up to 1120 ˚C [48]. Thin film seed and cold seeding method allow one to make many samples one time or to study the impact of grain boundaries in a multi-seeded sample with controlled oriented domains. Most of our samples were grown by seeding with NdBCO thin films.

1.6 Applications of bulk (RE)BCO materials

Bulk (RE)BCO superconductors can be applied to three general categories of engineering, including levitation devices (maglev, flywheels, seismic isolation and etc.), rotate machines (motors and generators), trapped flux devices (sputtering systems, separators, drag delivery system, magnetic resonance and etc.). As an example, we exhibit a motor made by our laboratory.

Bulk HTS has the ability to trap a large magnetic field. The maximum value of trapped flux density is approximately four times of the conventional Nd-Fe-B magnet. It permits its use as permanent magnet in a motor or generator. For the most part, initial experiments with bulk HTS motors have allowed the entire motor to be situated in a liquid-nitrogen bath. To date, the applications mostly involve the cryogenic pumping. In 2007, our laboratory developed a complete closed-cycle thermosyphon (TS) cooling system by using neon gas, and successfully cooled down the bulks below 40 K, and improved these TS in 2009. A two-phase closed-cycle TS is in testing [49]. With the improved TS, the cooling of the eight Gd-123 bulks comprised in the motor shrank from 2100 minutes to less than 400

minutes with a cooling power of about 50 W at 30 K. Figure 1-12(a) shows the schematic view of the bulk HTS synchronous motor and the peripheral systems. Figure 1-14(b) is the picture of our real system. Recently, thanks to the bulks doping with magnetic Fe-B alloy particles (MP) and improvement of TS, we found the decay of the trapped flux of the Gd-123 field poles after 5 hours synchronous operation at 35 K was 7.2 % for Gd-123 bulk without MP and 4.1 % for the Gd-123 with MP. More than 50 % reduction of the flux decay at 35 K compared to that at 77 K [49, 50].

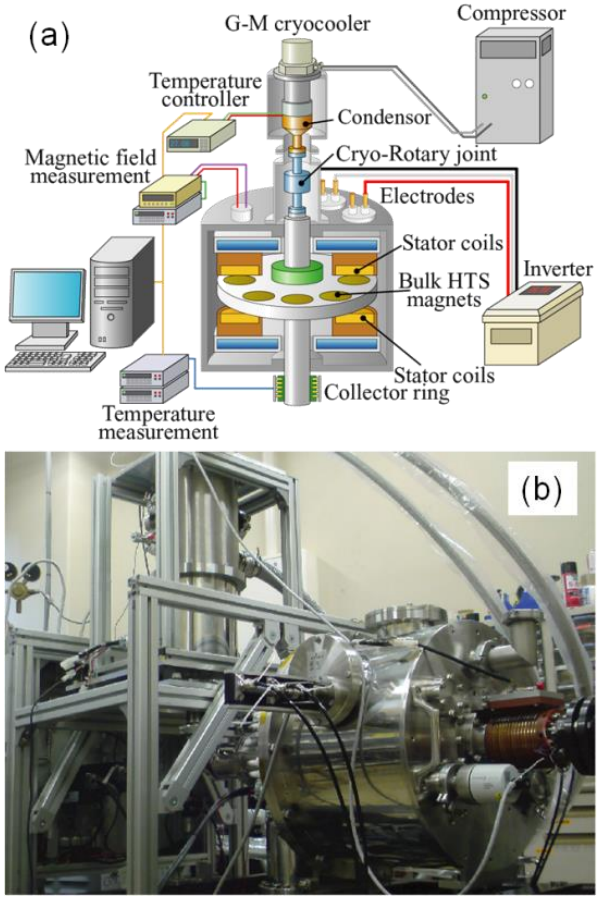

Figure 1-12 (a) Schematic view of the bulk HTS synchronous motor and the peripheral systems (M. Miki). (b) The picture of the real system [49].

Seen from the characterizations mentioned above, high trapped flux density and large size of the melt-textured bulk superconductors allow itself to be a good candidate for replacing the conventional permanent magnet in many developed conventional permanent magnet based devices. We believe that continuous development of the growth techniques as well as the optimized strategies of engineering pinning centres make the melt-textured RE-123 bulk superconductor to exhibit high potentials in applied superconductivity in future.

1.7 Motivation of the present work

Our target is to develop high efficient motors and generators by employing the type-II bulk superconductors in which the high critical current density and high pinning property are necessary. To date, high critical current density is mainly achieved in zero magnetic fields in previous studies. This high performance is suppressed exponentially with increasing of external magnetic field. It is desirable to maintain this high performance in high magnetic field since the type-II superconductors are worked in magnetic field in Maglev, motors and generators, etc. Some results show high pinning performance in low temperature and high magnetic field, but the fundamental reasons behind this phenomenon remain in mystery. No available clear scenario could be followed on making high quality samples with high pinning performance. The prototype applications of type-II superconductor are thus carried out mostly in laboratory. To promote the large-scale practical applications of type-II superconductor, our target in the thesis is to make high quality melt-textured bulk samples, make clear the fundamental relationships between current-carrying ability/vortex pinning and pinning landscape, and find the ways toward the high current-carrying ability and the strong trapped flux performance in melt-textured Gd-Ba-Cu-O bulk superconductor.

References

[1] H. K. Onnes, *Proceedings of the Koninklijke Akademie Van Wetenschappen Te Amsterdam* 14 (1911) 113.

[2] J. G. Bednorz and K. A. Muller, *Zeitschrift Fur Physik B-Condensed Matter* 64 (1986) 189.

[3] Y. Kamihara, T. Watanabe, M. Hirano, and H. Hosono, *J. Am. Chem. Soc.* 130 (2008) 3296.

[4] W. Meissner and R. Ochsenfeld, *Naturwissenschaften* 21 (1933) 787.

[5] F. London and H. London, *Proceedings of the Royal Society of London Series AMathematical and Physical Sciences* 149 (1935) 0071.

[6] V. Ginzburg and L. Landau, *Zh. Eksp. Teor. Fiz.*, 20 (1950) 1064.

[7] A. A. Abrikosov, *Soviet Physics JETP-USSR* 5 (1957) 1174.

[8] I. Maggioaprile, C. Renner, A. Erb, E. Walker, and O. Fischer, *Phy. Rev. Lett.* 75 (1995) 2754.

[9] G. Blatter, M. V. Feigelman, V. B. Geshkenbein, A. I. Larkin, and V. M. Vinokur, Rev. Mod. Phys. 66 (1994) 1125.

[10] T. Takizawa, M. Murakami, *Critical Currents in Superconductors*, (2005) ISBN: 4-902385-11-2.

[11] M. Konczykowski, F. Rullieralbenque, E. R. Yacoby, A. Shaulov, Y. Yeshurun, and P. Lejay, *Phy. Rev. B* 44 (1991) 7167.

[12] L. Krusin-Elbaum, J. R. Thompson, R. Wheeler, A. D. Marwick, C. Li, S. Patel, and D. T. Shaw, *Appl. Phy. Lett.* 64 (1994) 3331.

[13] A. Goyal, et al., *Super. Sci. Tech.* 18 (2005) 1533.

[14] S. Kang, et al., *Science* 311 (2006) 1911.

[15] S. R. Foltyn, L. Civale, J. L. MacManus-Driscoll, Q. X. Jia, B. Maiorov, H. Wang and M. Maley, *Nature Mater.* 6(9) (2007) 631-642.

[16] B. Zhao, W. H. Song, X. C. Wu, J. J. Du, Y. P. Sun, H. H. Wen, and Z. X. Zhao, *Physica C* 361 (2001) 283.

[17] S. Jin, T. H. Teifel, R. C. Sherwood, M. E. Davis, P. B. van Dover, G. W. Kammlott, R. A. Fastnacht, and H. D. Keith, *Appl. Phys. Lett.* 52 (1988) 2074.

[18] K. Salama, V. Selvamanickam, L. Gao, and K. Sun, *Appl. Phys. Lett.* 54 (1989) 2352.

[19] H. Hojaji, K. A. Michael, A. Barkatt, A. N. Thorpe, F. W. Matthew, I. G. Talmy, D. A. Haught and S. Alterescu, *J. Mater. Res.* 4 (1989) 28.

[20] W. Zhang, and K. Osamura, *Adv. Supercond.* 3 (1991) 437.

[21] T. Aselage and K. D. Keefer, *J. Mater. Res.* 3 (1988) 1279.

[22] M. Murakami, *Supercond. Sci. Technol.* 5 (1992) 185.

[23] Wai Lo, D. A. Cardwell, C. D. Dewhurst, H-T. Leung, J. C. L. Chow and Y. H. Shi, *J. Mater. Res.* 12 (1997) 2889.

[24] Wai Lo, D. A. Cardwell and J. C. L. Chow, *J. Mater. Res.* 13 (1998) 1141.

[25] Salama K, Selvamanickam V, Gao L and Sun K *Appl. Phys. Lett.* 54 (1989) 2352.

[26] M. Murakami, M. Morita, K. Doi and K. Miyamoto, *Jpn. J. Appl. Phys.* 28 (1989) 1189.

[27] H. Fujimoto, M. Murakami, S. Gotoh, N. Koshizuka, S. Tanaka, *Advances in Superconductivity II* edited by T. Ishigura and K. Kajimura (Tokyo: Springer) (1990) p285.

[28] Z. Lian, Z. Pingxian, J. Ping, W. Keguang, W. Jingrong and W. Xiaozu, Supercond. *Sci. Technol.* 3 (1990) 490.

[29] Z. Lian, Z. Pingxian, J. Ping, W. Keguang, W. Jingrong and W. Xiaozu, *IEEE Trans. Mag.* 27 (1991) 912.

[30] S. I. Yoo, N. Sakai, H. Takaichi, T. Higuchi and M. Murakami, *Appl. Phys. Lett.* 65 (1994) 633.

[31] M. Murakami, N. Sakai, T. Higuchi and S. I. Yoo, *Supercond. Sci. Technol.* 9 (1996) 1015.

[32] N. Sakai, S. Nariki, K. Nagashima, M. Miryala, M. Murakami, I. Hirabayashi, *Physica C* 460 (2007) 305.

[33] S. Nariki, N. Sakai, M. Kita, M. Fujikura, M. Murakami, I. Hirabayashi, *Supercond. Sci. Tech.* 19 (2006) S500.

[34] N. Sakai, K. Inoue, S. Nariki, A. Hu, M. Murakami, I. Hirabayashi, *Physica C*, 426-431 Part 1 (2005) 515.

[35] E.S. Reddy, T. Rajasekharan, *J Mater. Res.* 13 (1998) 2472.

[36] E.S. Reddy, T. Rajasekharan, *Supercond. Sci. Tech.* 11 (1998) 523.

[37] E.S. Reddy, G.J. Schmitz, *Supercond. Sci. Tech.* 15 (2002) L21.

[38] E.S. Reddy, J.G. Noudem, M. Tarka, G.J. Schmitz, *Supercond. Sci. Tech.* 13 (2000) 716.

[39] E.S. Reddy, G.J. Schmitz, *Supercond. Sci. Tech.* 15 (2002) 727.

[40] S. Meslin, K. Iida, N.H. Babu, D.A. Cardwell, J.G. Noudem, *Supercond. Sci. Tech.* 19 (2006) 711.

[41] K. Iida, N.H. Babu, Y. Shi, D.A. Cardwell, *Supercond. Sci. Tech.* 18 (2005) 1421.

[42] S. Meslin, J.G. Noudem, *Supercond. Sci. Tech.* 17 (2004) 1324.

[43] N.D. Kumar, T. Rajasekharan, K. Muraleedharan, A. Banerjee, V. Seshubai, *Supercond. Sci. Tech.* 23 (2010) 105020.

[44] D.A. Cardwell, N.H. Babu, *Physica C* 445 (2006) 1.

[45] H.T. Ren, L. Xiao, Y.L. Jiao, M.H. Zheng, *Physica C*, 412-414 Part 1 (2004) 597.

[46] Y. Shi, N.H. Babu, D.A. Cardwell, *Supercond. Sci. Tech.* 18 (2005) L13.

[47] S.B. Yan, L.J. Sun, T.Y. Li, L. Cheng, X. Yao, *Supercond. Sci. Tech.* 24 (2011) 075007.

[48] H. H. Xu, Y. Y. Chen, L. Cheng, S. B. Yan, D. J. Yu, X. Yao, http://arxiv.org (2011).

[49] B. Felder, M. Miki, Z. Deng, K. Tsuzuki, N. Shinohara, M. Izumi, H. Hayakawa, *IEEE T. Appl. Supercon.* 21 (2011) 2213.

[50] M. Miki, B. Felder, K. Tsuzuki, Z. Deng, N. Shinohara, M. Izumi, T. Ida, H. Hayakawa, *IEEE T. Appl. Supercon.* 21 (2011) 1185.

Chapter 2 Characterization Techniques and Experimental Procedure

In this chapter, several pieces of equipment and general experimental procedures that were employed are briefly described. The details of measurement conditions as well as sample preparation procedures are described as follows.

2.1 Characterization techniques

2.1.1 Differential thermal analysis

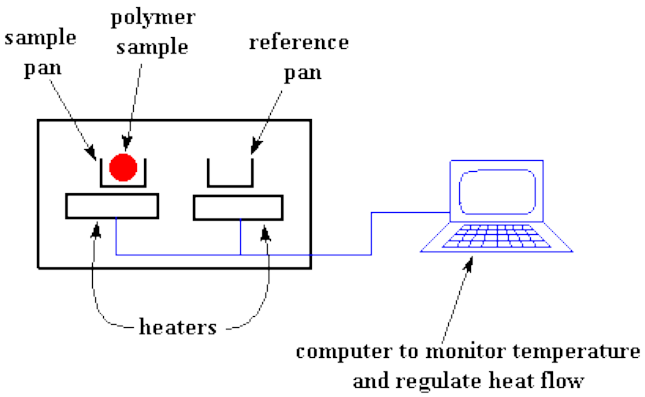

Figure 2-1 Schematic diagram of differential temperature analysis (DTA) system

Differential thermal analysis is a thermoanalytic technique, similar to differential scanning calorimetry. In DTA, the material under study and an inert reference are made to undergo identical thermal cycles, while recording any temperature difference between sample and reference [1]. This differential temperature is then plotted against time, or against temperature (DTA curve or thermogram). Changes in the sample, either exothermic or endothermic, can be detected relative to the inert reference. Thus, a DTA curve provides data on the transformations that have occurred, such as glass transitions, crystallization, melting and sublimation. The area under a DTA peak is the enthalpy change and is not affected by the heat capacity of the sample. A DTA curve can be used only as a finger print for identification purposes but usually the applications of this method are the determination of phase diagrams, heat change measurements and decomposition in various atmospheres.

A DTA consists of a sample holder comprising thermocouples, sample containers and a ceramic or metallic block; a furnace; a temperature programmer; and a recording system. The key feature is the existence of two thermocouples connected to a voltmeter. One thermocouple is placed in an inert material such as Al_2O_3, while the other is placed in a sample of the material under study. As the temperature is increased, there will be a brief deflection of the voltmeter if the sample is undergoing a phase transition. This occurs because the input of heat will raise the temperature of the inert substance, but be incorporated as latent heat in the material changing phase [2]. The schematic diagram is

shown in figure 2-1.

In our case, TG-DTA is a commercial system (MAC Science, WS002 system). Figure 2-2 is the photograph of our instrument. The detailed parameters are listed in table 2-1.

Figure 2-2 Photograph of our TG-DTA system (MAC Science, WS002).

Table 2-1 Measurement conditions for TG-DTA system (MAC Science, WS002)

Description	Specifications
Equipment	MAC Science: System WS002
Sample weight	About 10 mg
Crucible material	Al_2O_3
Heating rate	
T≤800 ℃	20 K/min
T≥800 ℃	5 K/min
Maximum temperature	1200 ℃
Materials used for calibration	Au
Sampling interval	5.0 sec/sampling
Thermocouple	Pt-Rh

2.1.2 X-ray powder diffraction

Powder diffraction is a scientific technique using x-ray diffraction (XRD) to characterize the crystal structure, crystallite size, and preferred orientation in polycrystallite or powdered solid samples [3]. In an idea case, it reveals every possible crystalline orientation equally in the sample, producing smooth diffraction rings around the beam axis rather than discrete Laue spots observed in single crystal diffraction. Following Bragg's law and a corresponding particular reciprocal lattice vector in the sample crystal, each ring appears by intensity proportional to the number of such planes. In practice, some effects of textures should be eliminated to achieve true randomness by rotating the sample orientation. Relative to other methods of analysis, powder diffraction allows for rapid, non-destructive analysis of multi-component mixtures without the need for extensive sample preparation.

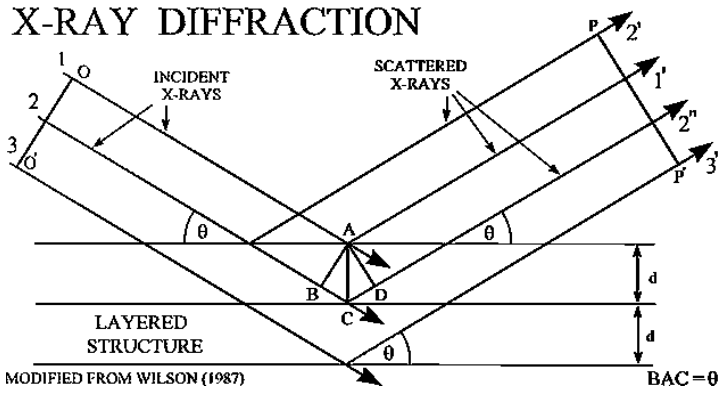

Figure 2-3 Reflection of x-rays from planes of atoms in a solid.

Equation 2.1 is equivalent to the usual form of Bragg law according to fig. 2-3. The reciprocal lattice provides a simple graphical representation satisfying the Bragg law.

$$2d_{hkl}\sin\theta = n\lambda \tag{2.1}$$

The structure factor depends on the atomic position which are represented by the cell vector $\vec{\boldsymbol{r}}_n$, $\vec{\boldsymbol{r}}_n = x_n\vec{\boldsymbol{a}}_1 + y_n\vec{\boldsymbol{a}}_2 + z_n\vec{\boldsymbol{a}}_3$, where x_n, y_n, z_n are the numbers between zero and unity. In a crystal of which Bravais lattice is body-centered, there must be an identical atom with coordinates x_n+1/2, y_n+1/2, z_n+1/2. Then the structure factor is given by:

$$F_{hkl} = \left[1 + e^{\pi i(h+k+i)}\right]\sum_{n/2} f_n e^{2\pi i(hx_n+ky_n+lz_n)} \tag{2.2}$$

and hence

$$F_{hkl} = \begin{cases} 2\sum_{n/2} f_n e^{2\pi i(hx_n+ky_n+lz_n)}, & h+k+l = \text{even} \\ 0, & h+k+l = odd \end{cases} \tag{2.3}$$

In the powder method, a monochromatic beam falls upon a powder sample containing

an enormous number of tiny crystallites having completely random orientations. For a set of planes *hkl*, the total diffracted power comes from the multiplied intensity in the orientation range and the element of area. It is expressed by:

$$P = I_0\left(\frac{e^4}{m^2c^4}\right)\frac{V\lambda^3 mF_T^2}{4v_a^2}\left(\frac{1+\cos^2 2\theta}{2\sin\theta}\right) \tag{2.4}$$

Where

$$F_T = \sum_n f_n e^{-\frac{B\sin^2\theta}{\lambda^2}} e^{2\pi i(hx_n+ky_n+lz_n)} \tag{2.5}$$

The flat faced sample is symmetrically placed relative to the primary and diffracted beams, the power per unit length of diffraction circle at a distance **R** is:

$$P' = \frac{P_0}{16\pi R}\left(\frac{e^4}{m^2c^4}\right)\frac{\lambda^3 mF_T^2}{2\mu v_a^2}\left(\frac{1+\cos^2 2\theta}{\sin\theta\sin 2\theta}\right) \tag{2.6}$$

If extinction is absent and the sample is a completely randomly oriented, the areas of the diffraction peaks on a diffractometer pattern are a direct proportion to the P' in the equation 2.6. The most widespread use of x-ray powder diffraction is for the identification of crystalline compounds by their diffraction pattern.

In this study, the XRD measurements were performed by using a commercial system (MAC Science; M18XHF-SRA). The details of experimental conditions are shown in table 2-2. Some specific uses are listed in table 2-3.

Table 2-2 Measurement conditions of X-ray diffraction.

Description	Specifications
Equipment	MAC Science Co. Ltd.: M18XHF-SRA
X-ray generator	18 kW
Target	Cu $K_{\alpha 1}$(λ=1.5405 Å)
Monochromatic	Used
Voltage	40 kV
Current	200 mA
Sampling width	0.0200 deg.
Scanning speed	0.5 deg/min.

Table 2-3 Specific uses of X-ray powder diffraction

1) Phase identification
2) Crystallinity
3) Lattice parameters
4) Expansion tensors, bulk modulus
5) Phase transitions
6) Crystal structure refinement and determination
7) Size and strain broadening
8) Comparison of X-ray and neutron scattering
9) Aperiodically-arranged clusters

2.1.3 Trapped field mapping system

Figure 2-4 Photograph of the automatic Hall probe measurement system.

The trapped flux distribution was measured with an automatic Hall probe measurement system (F. W. Bell, BHT-921) as shown in fig. 2-4. The bulks under study were usually cooled to 77 K in the presence of magnetic field 1 T ~ 5 T applied parallel to the c-axis in a superconducting magnet (see fig. 2-5). The trapped flux was measured after field cooling in thirty minutes. Hall sensor was positioned ~ 0.5 mm above the surface of the polished samples.

Figure 2-5 5 T superconducting magnet.

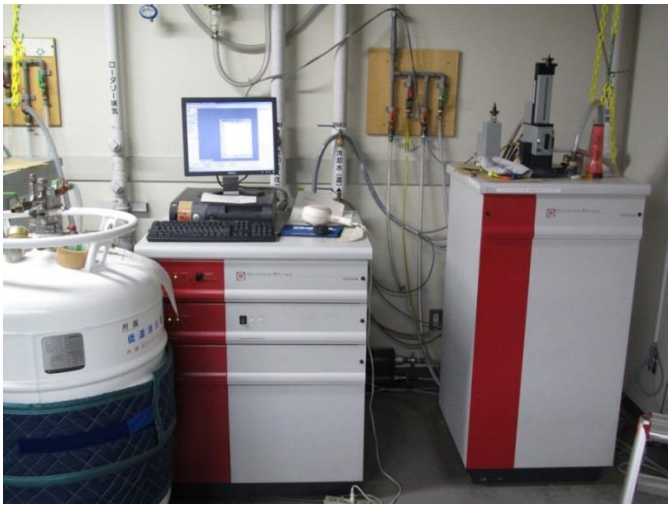

Figure 2-6 MPMS-XL-7 in Institute for Solid State Physics, University of Tokyo.

2.1.4 SQUID magnetometry

The magnetic measurements in this study were performed with a SQUID–based magnetometer in Institute for Solid State Physics, University of Tokyo, as shown in fig. 2-6. These instruments are very sensitive to changes in magnetic flux (a fraction of a flux quantum). We used a commercially available device from Quantum Design Inc. The model is MPMS-XL-7 with a 7 tesla magnet. The smallest magnetic moment the MPMS can measure is ~10^{-7} emu and an extended range option allows measurements to 300 emu. At the center of the magnet, the magnetic field is uniform to within 0.01% over a 4 cm axial distance. The lowest temperature achievable is 1.9 K with an accuracy of 0.01 K.

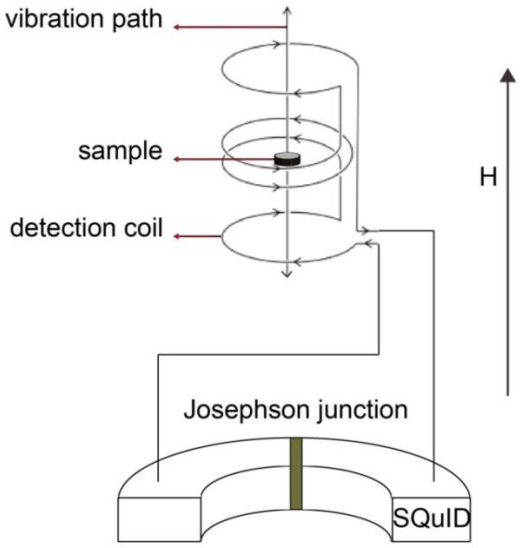

Figure 2-7 Schematic drawing of an MPMS system using a SQUID sensor.

Figure 2-7 is a schematic drawing of the elements of a SQUID magnetometer. The SQUID device itself uses the principle of Josephson junctions [4]. A superconducting ring with one or two thin insulating layers, creating weak links to form parallel Josephson junctions, comprises the main component of the SQUID sensor. If a constant bias current is maintained in the SQUID, the measured voltage will oscillate with the changes of phase in the two junctions. This phase change is directly related to the change in magnetic flux. The measured voltage and instrument sensitivity are calibrated by using samples that have a known magnetic moment, such as a Ni sphere or Pd metal susceptibility standard. Once the instrument has been calibrated, the measured induced voltages can then be used to accurately measure magnetic moments of unknown samples. The sample is mounted on a sample rod and centered between a set of detection coils that are coupled to the SQUID sensor by superconducting wires.

The system of detection coils and superconducting wires form a dc flux transformer that helps reduce the problems of external fields. It is a continuous superconducting wire that is wound to form a transformer at one end and as a second derivative coil in the sample space, as one can see in fig. 2-8. The longitudinal pickup coil has three sections. The top and bottom sections each have a coil wound in a clockwise sense and the middle section is a coil with two turns wound a counterclockwise manner. With this second-derivative configuration, the pickup (sample detection) coil is insensitive to a uniformly varying magnetic field, but it is sensitive to a magnetic moment that is translated through it. The resulting output voltage from the SQUID detection system is then compared to and fit to the scan pattern produced by a perfect dipole.

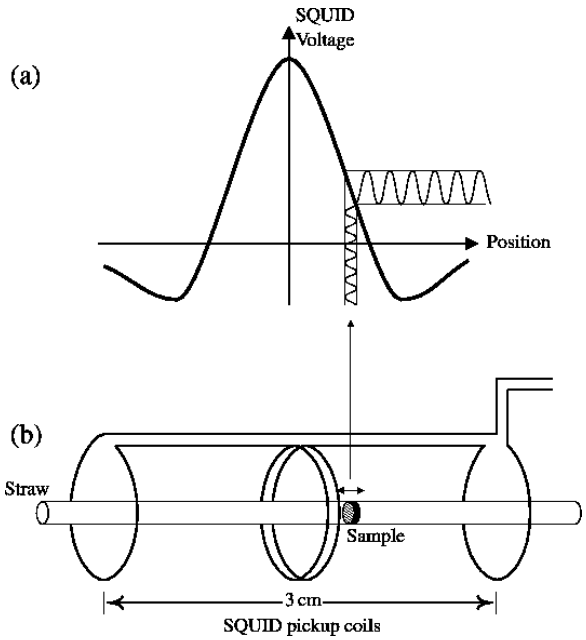

Figure 2-8 An illustration of a flux transformer. (a) shows the ideal SQUID response for a dipole and (b) shows the movement of the sample within the SQUID pickup coils.

2.1.5 Scanning electron microscope

A scanning electron microscope (SEM) is a type of electron microscope that produces images of a sample by scanning it with a focused beam of electrons. The electrons interact with atoms in the sample, producing various signals that can be detected and that contain information about the sample's surface topography and composition. The electron beam is generally scanned in a raster scan pattern, and the beam's position is combined with the detected signal to produce an image. SEM can achieve resolution better than 1 nanometer. Specimens can be observed in high vacuum, in low vacuum, and (in environmental SEM) in wet conditions.

The most common mode of detection is by secondary electrons emitted by atoms excited by the electron beam. The number of secondary electrons is a function of the angle between the surface and the beam. On a flat surface, the plume of secondary electrons is mostly contained by the sample, but on a tilted surface, the plume is partially exposed and more electrons are emitted. By scanning the sample and detecting the secondary electrons, an image displaying the tilt of the surface is created.

Microstructure observations were performed by using a SEM in the Institute for Solid State Physics, University of Tokyo. The model is JEOL JSM-5600 as shown in fig. 2-9. Specific parameters are listed in table 2-4. By means of the accessory of Oxford Inca Energy 200 energy dispersive spectrometry (EDS) system, chemical compositions of the focused area of sample can be obtained. The relevant parameters are listed in table 2-5.

Table 2-4 Specific parameters of JSM-5600

1)	3.5 nm resolution
2)	Accelerating voltage from 0.5 to 30 kV
3)	Magnification from x18 to x300,000
4)	Secondary and backscattered electron imaging modes
5)	Goniometer stage for specimens up to 15 cm in diameter
6)	Deben X/Y/rotation axis stage
7)	Transmitted electron adapter for analysis of thin films, sections and particles
8)	90 degree tilt rotary adapter for 360 degree views of specimens
9)	Digital image acquisition (640 x 480, 1280 x 960 or 2560 x 1920 pixels)
10)	Real time video capability

Table 2-5 Specific parameters of Oxford Inca Energy 200

1)	138 eV resolution Pentafet detector
2)	SATW window for detection of Boron and all heavier elements
3)	Autocolumn for control of SEM functions from Inca console
4)	Software for qualitative, semi-quantitative and quantitative analyses
5)	SmartMap of a "virtual specimen" allowing mapping of any element from stored data

Figure 2-9 JEOL JSM-5600 in Institute for Solid State Physics, University of Tokyo.

2.2 Experimental procedure

2.2.1 Synthesis of $GdBa_2Cu_3O_{7-\delta}$ powder

Gd_2O_3 (3N), $BaCO_3$ (3N) and CuO (3N) act as the starting material with a molar ratio of 1:4:6 and were mixed thoroughly in a mortar and pestle. The mixture was pre-calcined at 870 ℃ for 20 hours in a conventional box furnace. Further calcined at 890 ℃ for 15 hours, single phased Gd-123 was obtained. We found that single phased Gd-123 can be synthesized from 890 ℃ to 920 ℃. By means of analysis of XRD pattern, we found that the average particle size increase with increasing of the sintering temperature since the main peak is broadened when using a high temperature and even split at 920 ℃ as shown in the enlargement in fig. 2-10. The colors of the powder are changed from dark to light as shown in fig. 2-11.

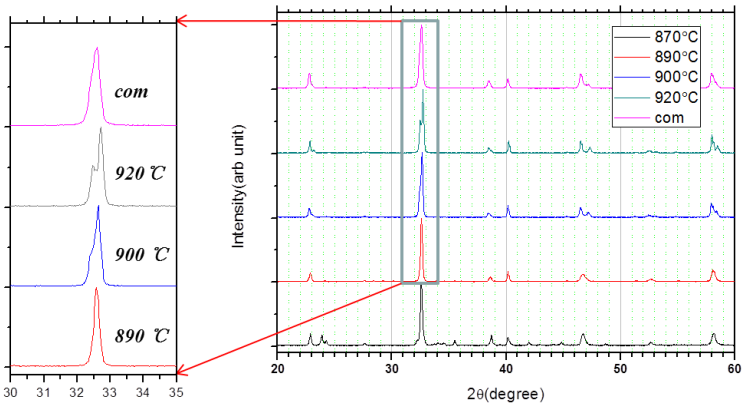

Figure 2-10 XRD patterns for the powders calcined at different temperatures. Com is an abbreviation of the word commercial.

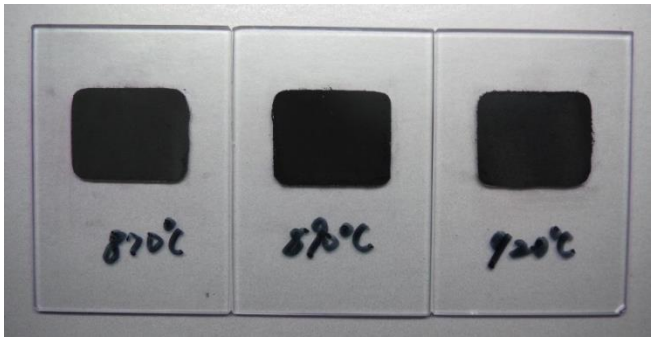

Figure 2-11 Color of the powder calcined at different temperatures.

2.2.2 Synthesis of Gd_2BaCuO_5 powder

Gd_2O_3 (3N), BaO_2 (3N) and CuO (3N) act as the starting material with a molar ratio of 1:1:1 and were mixed thoroughly in a mortar and pestle. The mixture was calcined three times at 840 ℃, 870 ℃ and 890 ℃ for 10 hours respectively. By means of the third calcination, single phased green Gd-211 powder is obtained.

2.2.3 General process of top seeded melt growth

Precursor for TSMG was mixed in nominal composition of Gd-123 + 40 mol% Gd-211 + 10 wt% Ag_2O + 0.5 wt% Pt + *x* mol% additives. The mixed powders were uniaxially pressed into 20 mm in diameter pellets and consolidated by cold isostatic pressing. The green pressed pellet was placed onto Y-stabilized ZrO_2 supporting rods inside a conventional box furnace.

The principle of melt growth is that $GdBa_2Cu_3O_{7-\delta}$ (Gd-123) compounds decompose into Gd_2BaCuO_5 (Gd-211) solid inclusions and Ba-Cu-O liquid phase by the peritectic melting as descried in equation 1.19. During the solidification, the Gd-211 and liquid phase convert again to Gd-123 as seen in equation 1.22.

The melting process was performed in a modified furnace under ambient atmosphere.

The thermal pattern was shown in figure 2-12. In brief, the sample was heated to 1100 ℃ within 10 h, kept there for 30 minutes, then cooled down to 1030 ℃ and subsequently held for 1 h. Before cooling down to the starting growth temperature (T_{g1}) 1010 ℃, a melt-textured Mg-doped $NdBa_2Cu_3O_{7-\delta}$(001) seed crystal was placed on top surface of the pellet to control the crystallization. In order to avoid cracking of the seed arising from the large temperature difference, Two-step hot-seeding method was employed: firstly put the seed on the doorsill of the furnace, heat for 5 min, and then place the seed on the surface of the partially melted pellet. During the growth, 130 ~ 150 hours undercooling with a rate of 0.3 ℃/ h was employed. In this way, single domains with ~ 17 mm in diameter can be obtained.

This process can be simplified by using cold seeding method as described in chapter 1. It is worth to mention that thanks to TSMG techniques and cold seeding method batch process of large sized bulk sample can be obtained. In particular, cold seeding method also allows one to grow the controlled multidomain samples with controlled shapes and orientations of the multidomains. The mass production of superconducting bulk magnet is running toward commercialization.

2.3 Exploring optimal growth parameters

2.3.1 Using hot seeding method

We first explored the effect of starting growth temperatures on the trapped flux performance by using the hot seeding method. Mg-doped Nd-123 crystal acts as seed. Temperature profile is shown in fig. 2-12. The composition of the precursor is Gd-123 + 40 mol% Gd-211 + 10 wt% Ag_2O + 0.5 wt% Pt. A single domain can be obtained by using the starting temperature 1010 ℃, but one can see that small multidomains appear at the bottom in fig. 2-13. Those small multidomains prevent the full growth of the main single domain. These multidomains come from the disadvantages of hot seeding method, because serious thermal loss cannot be avoided by opening the door of a furnace for seeding process. These multidomains also imply that the set starting growth temperature seems too low for achieving a well growth of a single domain. We measured the trapped field of this sample. It shows a maximum value of ~ 1.5 T in trapped flux density. Optimal growth conditions are necessary to be explored further.

After changing the starting growth temperature, we found that a higher starting growth temperature of 1015 ℃ is the best choice. For achieving the optimized trapped field, cooling rate should be modified too. The final optimal growth conditions are shown in fig. 2-14. The sample was processed first by using a slow cooling rate of 0.25 ℃/h and followed by a fast cooling rate of 0.42 ℃/h. Figure 2-15 shows the single domain obtained

by using the optimal temperature profile, which has been grown fully but still shows a secondary domain in the bottom. By reducing the time of seeding process, such secondary domain can be eliminated as shown in fig. 2-16. By such modification, trapped field was improved significantly up to 0.29 T as shown in figure 2-17. It also shows a good reproducibility for the higher trapped flux density. Optimization of the growth conditions is a good way towards the high trapped flux performance at the beginning of this study.

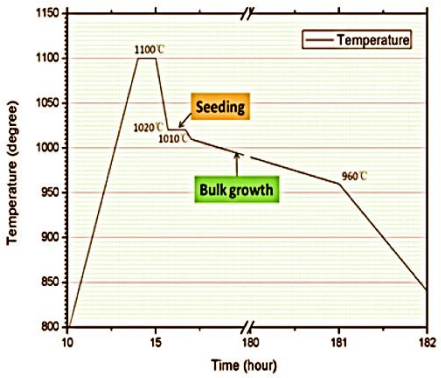

Figure 2-12 Temperature profile adopted by using the general hot seeding method.

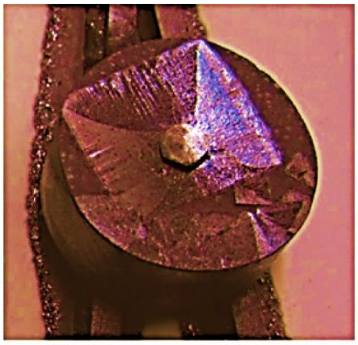

Figure 2-13 A single domain obtained by using the temperature profile in fig. 2-12.

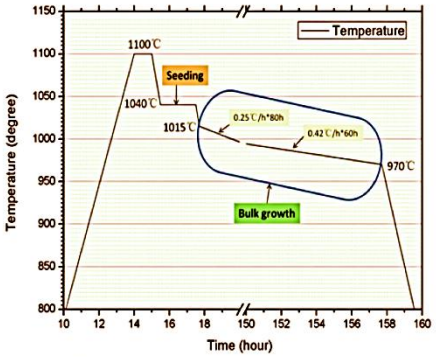

Figure 2-14 The optimal temperature profile adopted by using the general hot seeding method.

Figure 2-15 A single domain obtained by using the optimal temperature profile in fig. 2-14.

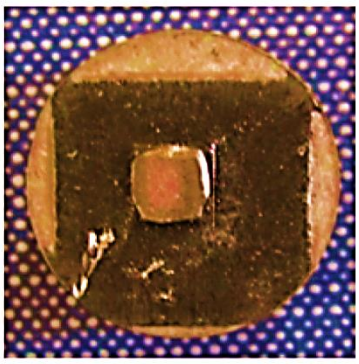

Figure 2-16 Single domain obtained by using the optimal temperature profile with an optimized seeding process.

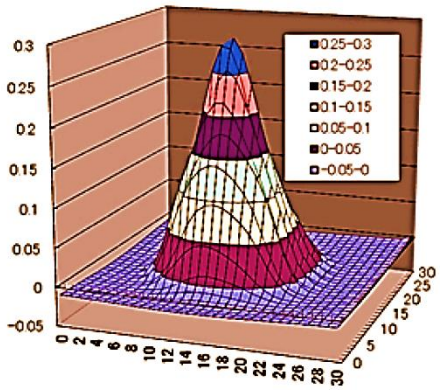

Figure 2-17 Trapped field mapping above the sample shown in fig.2-16 with a gap of 0.5 mm at 77 K.

Slow cooling rate helps to optimize the full growth of sub-grains of matrix. It is known that the quality of the textured matrix can be improved by reducing the weak links, cracks as well as pores. Slow growth in high temperature and followed by fast growth in relative low temperature meet the requirement of high quality crystal growth. In particular, superconducting property such as the transition temperature generally can be optimized too. In addition to the main consideration mentioned above, such a temperature profile meets the actual crystal growth rate. That is, the growth becomes fast and fast with decreasing of temperature even one use the definite cooling rate. Using the fast cooling rate in the later growth stage promotes the short growth time and reduces the cost.

2.3.2 Using cold seeding method

We also explored the growth conditions by using a cold seeding method. First we made a textured Mg-doped Nd-123 sample with multdomains as shown in fig. 2-18. It was crashed into small rectangle crystals. Those crystals were used as seeds. The seed was put on top of the pellet in a conventional box furnace and then the arrangement was subject to the melting growth. Three growth conditions are examined. First, the maximum value of temperature (T_{max}) was set to 1060 ℃. Growth window was set from 1036 ℃ to 998 ℃ in 130 hours. The seed was melted completely and failed on texturing of a single domain as shown in fig. 2-19a. Adjusting T_{max} to 1057 ℃, and using a growth window of 1020 ℃ ~ 960 ℃ in 150 hours, the seed is melted partially and small textured multidomain was observed as shown in fig. 2-19b. Changing T_{max} to 1050 ℃, and using a growth window of 1010 ℃ ~ 970 ℃ in 140 hours, the seed is still melted partially and full textured radiate domains were observed as shown in fig. 2-19c.

By comparing the hot and cold seeding method, we conclude that the pellet can be grown into single domain with a starting growth temperature 1010 ℃ ~ 1020 ℃. The optimal value is 1015 ℃. Cooling rate of 0.25 ℃/h ~ 0.42 ℃/h is available for single domain growth and results in high trapped flux performance. Nd-123 seed will be melted partially above 1050 ℃. Perfect single domain should be obtained easily if there are some available seeds with higher melting point above 1060 ℃. Nd-123 thin films met such requirement due to superheating phenomenon occurred during the melting process as described in chapter one.

In following section, we give our experimental result of the samples grown by employing the thin film seed and the cold seeding method. Thanks to these techniques, the samples can be grown in the unique growth conditions which are possible for comparing other important parameters that affect the final trapped flux performance. As an example, the trapped flux profile can be controlled by using different starting powders and different additions as described in the following section.

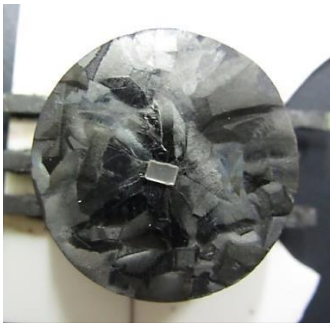

Figure 2-18 Image of the Mg-doped Nd-123 textured by using MgO seed.

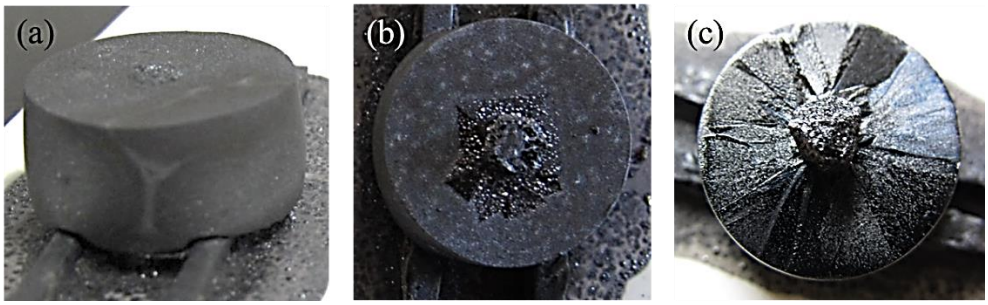

Figure 2-19 Images of samples after grown in different cold-seeding growth conditions.

2.4 How to control the trapped flux profile

After explored the optimal growth conditions, we studied the possible relevant parameters that may affect the trapped flux profiles. We found that the average particle size of the starting material is an important factor. As mentioned above, the average particle size of Gd-123 powder becomes larger and larger when the mixture was calcined at higher temperatures. We compared the trapped flux of samples grown from different Gd-123 powders such as the home-made Gd-123 powder and the commercial Gd-123 powder by using simultaneously a cold seeding method with Nd-123 thin film seed [Nd123 (500nm)/MgO(001)].

We found that the Nd-123 thin film can endure a highest temperature of 1097 ℃. The cold seeding method provides the high comparability since perfect single domain can be obtained by employing a batch process. T_{max} and T_{g1} were set to be 1097 ℃ and 1015 ℃ respectively. The cooling rate was set to be 0.3 ℃/h. Figure 2-20 shows the two bulks grown from different Gd-123 powders. The home-made one was synthesized at 920 ℃ and provided a large average particle size visually discernible. Highlighting the importance of liquids and the role of Pt, we adopted the following compositions:

Precursor (a): Gd123 (home-made) + 0.4 Gd211 +10 wt% Ag_2O+ 0.1 BaO_2

Precursor (b): Gd123 (commercial) + 0.4 Gd211 +10 wt% Ag_2O+ 0.5 wt% Pt

Figure 2-21 shows the trapped flux profiles. One can see that fig. 2-21a exhibits a concave shape and fig. 2-21b shows a convex shape. The maximum of trapped flux density

varies largely. It is 0.33 T (total trapped flux: 21.9 μWb) for the sample (a) as shown in fig. 2-21a and 0.18 T (total trapped flux: 22.0 μWb) for the sample (b) as shown in fig. 2-21b. The large average particle size and rich liquid supply result in better vortex pinning in the center part since pushing effect has been suppressed. Gd211 mainly maintains the shape of the sample as well as reduces the liquid loss in high temperature. It is worth to note that layered and pyramid-shaped crystal morphology is observed around the seed in fig 2-20a. This observation attracts our attention since it reveals a significant phenomenon of liquid transportation. More detailed information will be discussed in chapter 5. For the sample (b), the convex shape comes from the pushing effect due to fine Gd-123 particle.

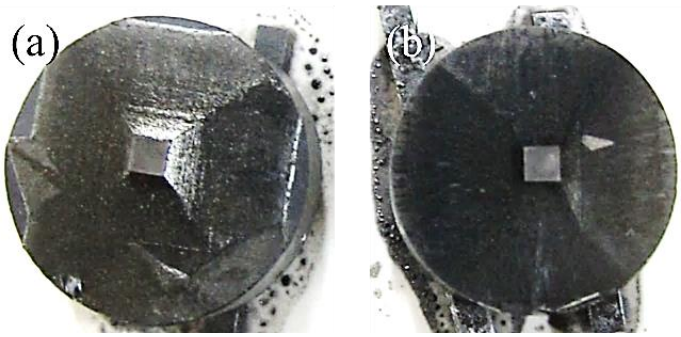

Figure 2-20 Single domain grown from (a) home-made Gd123 and (b) commercial Gd-123.

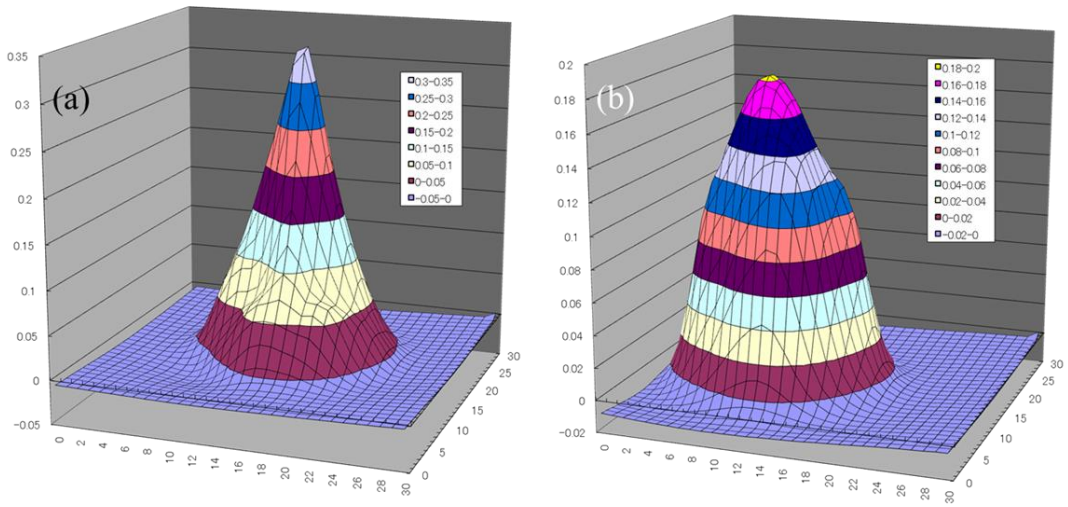

Figure 2-21 Trapped flux profile mapped on the sample grown from (a) home-made Gd123 and (b) commercial Gd-123.

References

[1] H.K.D.H.Bhadeshia "*Thermal analyses techniques. Differential thermal analysis*". University of Cambridge, Material Science and Metallurgy.

[2] R. Bud, D. Jean, "*WarnerInstruments of Science: An Historical Encyclopedia*", Science Museum, London and The National Museum of American History, Smithsonian Institution, (1998) ISBN 0815315619.

[3] B.D. Cullity, "*Elements of X-ray Diffraction*", Addison Wesley Mass, (1978) ISBN 0-201-01174-3.

[4] B. D. Josephson, *Physics Letters **1*** (1962) 251.

Chapter 3 Addition Effect of Barium Titanate on the Enhancement of Vortex Pinning

3.1 Introduction

From chapter 1, we have known that vortex pinning performance of type-II bulk superconductors is a critical factor for achieving high critical currents density (J_c) required for practical applications. Various nano-sized structural disorders are effective pinning centers for impeding thermally activated giant vortex motion, by which large J_c and high irreversibility field (B_{irr}) are achieved [1-3]. We are more interested in the in-field pinning performance since many applications of type-II superconductor are worked under magnetic field such as in Maglev, motors and generators. Generally, the high pinning performance is only achieved in self-field. Although the so-called peak effect is well known in high-T_c cuprates, the possible reasons behind this phenomenon is still not so clear, which obstructs the promotion of applications of type-II superconductor since there is no available definite strategies can be used. Therefore, one of our target is to make clear those possible reasons and then to give practical strategies to overcome those problems. That is, finding the possible key parameters for the control of vortex pinning. To get the possible entrance, we first explored the general strategies for achieving high pinning property by introducing tiny particles into the superconducting matrix. It is necessary to learn first the history of this research area as described in the following texts.

Introducing secondary phases into the superconducting matrix is an effective way to enhance the vortex pinning performance [3-5]. Bulk RE-123 superconductors grown by employing the TSMG process are able to trap vortex densities up to more than 2 T at 77 K, which is typically four times of that measured above a conventional Nd-based permanent magnet [6-7]. Nevertheless, owing to the large crystal defects, such as pores, cracks, and grain boundaries, the J_c values in those bulks are about three orders of magnitude lower than the predicted ones. It is necessary to do optimization further. Hence, extensive studies have been made on the melt-processed RE-123 bulks in the past two decades [8-9]. A few effective methods have been developed to improve the pinning performance. Such as the addition of secondary phases of RE_2BaCuO_{11} (RE-211) or $RE_2Ba_4MCuO_{11}$ (RE-2411, M = Zr, U, Mo, W, Ta, Hf, Nb and etc.) provides average strong pinning strength [10-12]; The mixed ternary light rare earth LRE-123 (LRE = Nd, Eu, and Gd) systems bring out more effective pinning performance because of the increased local tensions and LRE/Ba solid solutions [13]; introduce a little amount of ZrO_2 into Gd-123/Ag system further improve the vortex pinning [14]; some ferromagnetic Fe-B alloy particles also show such effectiveness [15]. All these features indicate that vortex pinning performance exhibits some kind of superimposed effect within certain chemical doping range. Finer effective additions compensate significantly the inadequate pinning posed by the interfaces between large defect and matrix. We can imagine this phenomenon as filling sand into rubble.

Inspiring by the ferromagnetic material doping, we hope to enhance the vortex pinning performance by introducing the multiferroic material $BiFeO_3$. This doping strategy has never been done by others. Bi is an important element in Bi-based serial high-T_c superconductors, while Fe atom exhibits magnetic property. Therefore, introducing perovskite $BiFeO_3$ into the Gd-123/Ag system should be effective imaginably for the enhancement of vortex pinning. We have performed the synthesis of $BiFeO_3$ and introduced this home-made material into the Gd-123/Ag system. However, the result is not so prominent although the enhancement of vortex pinning was observed in both low and middle field for the doping level of 0.2 mol% and 0.3 mol%. We then performed another doping strategy by employing a typical ferroelectric material.

In this chapter, we focus on the improvement of vortex pinning by employing the TSMG process together with the cold seeding method. A new kind of addition, namely barium titanate $BaTiO_3$ (BTO), was introduced into the matrix of Gd-123. BTO is a typical ferroelectric material with a perovskite structure and a high melt point of 1625˚C. Dilute doping strategy was adapted to study the extrinsic vortex pinning. By means of this strategy, one could achieve some useful information for understanding the complexity of vortex pinning in high-T_c bulk superconductor. In the initial stage of this thesis, we hope to find the key factors associated with the total pinning performance whether in self-field or in intermediate field. In addition, the dilute addition effect of BTO in this superconducting system is never reported in previous literatures. We want to make clear that whether such ferroelectric material could give positive contributions on vortex pinning. If it is positive, then we hope to know that what kind of elements is responsible for, since two possibilities may occur during the melt growth. One is that BTO may maintain stable due to its high melting point and acts as a core pinning centers with possible enhanced strains due to its ferroelectricity. The other is that BTO may decompose and react with the superconducting matrix. The products will lift up the chemical fluctuations and contribute to δl pinning if the products belong to non-superconducting phases or δT_c pinning if the products are weak superconducting phases. In this way, we learned some key factors for the control of vortex pinning. To ensure each bulk grown in the same condition, a batch process was used by employing the cold seeding method.

3.2 Experimental details

3.2.1 Synthesis of $BaTiO_3$

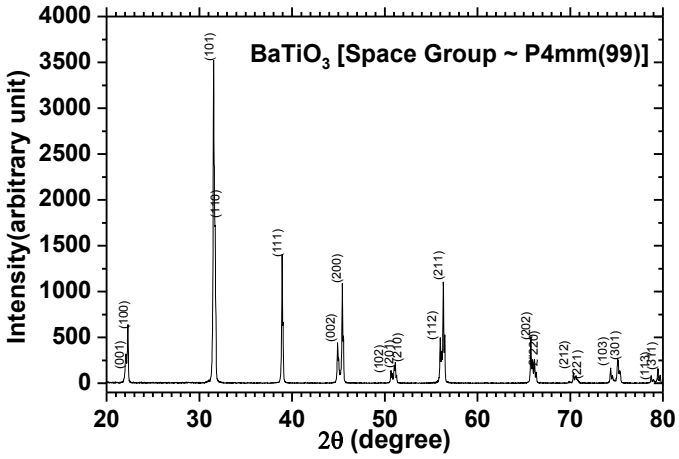

Figure 3-1 X-ray diffraction pattern of the synthesized $BaTiO_3$ powder shows a single phase with a tetragonal structure, P4mm.

$BaTiO_3$ powder was prepared following the solid-state synthesis by firing a mixture of $BaCO_3$ (Furuuchi chemical Co. Ltd., 99.9 %) and TiO_2 (Furuuchi chemical Co. Ltd., 99.9 %) at high temperature. They were mixed in a stoichiometric composition of $BaTiO_3$ and thoroughly ground using a mortar and pestle, then calcined at 1150 ˚C for 4 h [16]. X-ray diffraction pattern shows that a ferroelectric phase of BTO was successfully synthesized without visible impurities as shown in fig. 3-1. In order to make finer particles, a ball-milling treatment was carried out for 1 h by using Y_2O_3-ZrO_2 balls. The ground powder was sifted through a multistage vibrating sieve. The smallest size of the mesh is 32 μm.

3.2.2 Precursor preparation

Commercial powders of Gd-123 (TOSHIMA Co. Ltd., 99.9 %), Gd-211 (TOSHIMA Co. Ltd., 99.9 %), Ag_2O (TOSHIMA Co. Ltd., 99.9 %) and Pt (ISHIFUKU Co. Ltd.) were used as the starting materials. Gd-211 and Gd-123 powders were mixed as precursor in a molar ratio of Gd-211: Gd-123 = 0.4: 1. 10 wt.% Ag_2O and 0.5 wt.% Pt to the weight of precursor were weighed and added to the precursor to improve the mechanical properties and hinder the coarsening of Gd-211 respectively. The precursor was then equivalently divided into five samples. Various amounts of BTO in molar ratio to Gd-123 were separately added to the samples. The final compositions are as follows: Gd-123 + 0.4 Gd-211 + 10 wt.% Ag_2O + 0.5 wt.% Pt + x mol% $BaTiO_3$ (x = 0.0, 0.1, 0.2, 0.3 and 0.4). In order to make a uniform distribution of BTO particles, ethanol was added and then

thoroughly stirred and dried, the mixtures were uniaxially pressed into pellets of 20 mm in diameter and 10 mm in thickness with a pressure of 20 MPa.

3.2.3 Melting process

Five green pressed pellets were placed onto Y-stabilized ZrO_2 supporting rods. MgO crystal with a size of 2 mm × 2 mm × 0.5 mm covered by Nd-123 thin film [Nd-123 (500 nm) / MgO (100)] was placed on the top center of each pellet to nucleate the growth of a single grain, which were then melt grown in air in a conventional box furnace. The sample arrangement was heated to 83 ˚C above the peritectic temperature (T_p) in 6 hours, maintained there for 50 minutes, then cooled rapidly to 2 ˚C above T_p in 30 minutes and slowly cooled by 25 ˚C with a cooling rate 0.25 ˚C/h, cooled to 100 ˚C with a cooling rate 20 ˚C/h, finally, furnace cooled to room temperature [17]. Each sample can be grown into a single domain. The samples were cut into rectangular plate and oxygenated in a tubular furnace by the standard oxygenation method [18-19].

3.2.4 Characterization methods

For the magnetization measurements, rectangular plate of 2 mm × 2 mm × 1 mm was cut along the c-axis at the same position for each bulk, which has a distance of 2 mm away from the bottom surface of the seed. Superconducting properties were measured by a SQUID magnetometer (Quantum Design, MPMS-XL). The DC magnetization measurement was performed under the magnetic field applied parallel to the c-axis. Transition temperature T_c and the transition width ΔT_c were evaluated from the zero-field-cooled (ZFC) magnetization curves. Magnetization hysteresis loops with magnetic field up to 5 T at a constant sweep rate of 0.07 $Tmin^{-1}$ were obtained at 77 K. J_c values were deduced from the magnetization hysteresis loops by using the extended Bean's critical state model [20]. Thanks to scan electron microscopy (SEM; JSM5600), microstructure analysis was made along the a axis or c axis. The total element ratios of the local regions were determined by energy dispersive X-ray spectroscopy (EDX).

3.3 Results and discussions

3.3.1 Critical current and pinning property

Ion substitutions are generally to cause sophisticated weak superconducting phases in bulk cuprates and are reflected as an appearance of peaks (δT_c pinning) in the diagram of J_c - B curves. While the core pinning (δl pinning) effect is usually reflected as a high J_c value in J_c - B curves under the self-field if vortex lines are pinned by various defects or different kinds of non-superconducting phases. The J_c - B curves measured at 77 K for BTO doped Gd-123 bulks are shown in Fig. 3-2(a). In order to study the contributions of those two kinds of pinning mechanism, the normalized volume pinning force densities, $f_p = F_p/F_{p,max}$, as a function of the reduced fields, $h = B/B_{irr}$, have been deduced from the M - H curves. The result shows that all peak positions h_0 locate above 0.4. Since $h_0 \sim 0.5$ suggests a characteristic of δT_c pinning, the present result indicates the coexistence of δl pinning and δT_c pinning and δT_c pinning is in the dominant position. Therefore, the δl pinning curves have been fitted by using exponential functions for each specimen as shown in Fig. 3-2(b). Then the characteristics of δT_c pinning were deduced by subtract δl pinning curves from Fig. 3-2(a) and were shown in Fig. 3-2(c). The doping ratio dependences of both the onset T_c and the transition width ΔT_c were shown in Fig. 3-2(d). Combining Fig. 3-2(c) and Fig. 3-2(d), a doping law was achieved: the lower the peak, the narrower the transition width. The correctness of the dominance of δT_c pinning was confirmed again by those strict consistencies.

In contrast to the reference, each sample with the non-zero BTO addition shows an enhanced J_c from 0 T to 5 T as shown in Fig. 3-2(a), indicating that BTO is an effective addition for the enhancement of vortex pinning in Gd-123 bulk system. Interestingly, two optimized doping levels were observed in the samples with different doping amounts. One is the bulk doped with 0.1 mol% BTO (abbreviated as 0.1-BTO, other samples will be also marked in this way hereafter), which gives a significant increase of J_c both at zero and middle field. The other is 0.3-BTO, which is active at self-field but shows a reduction at the middle field as shown in Fig. 3-2(b) and (c).

A highest J_c (B = 0) value of 3.8×10^4 Acm^{-2} was achieved in 0.1-BTO, a similar value also appeared in 0.3-BTO. Correspondingly, a lowest onset T_c and a widest ΔT_c appeared in 0.1-BTO, while a narrowest ΔT_c appeared in 0.3-BTO. It indicates that BTO particles have reacted with Gd-123 and formed weak superconducting phases during the melting process in 0.1-BTO.

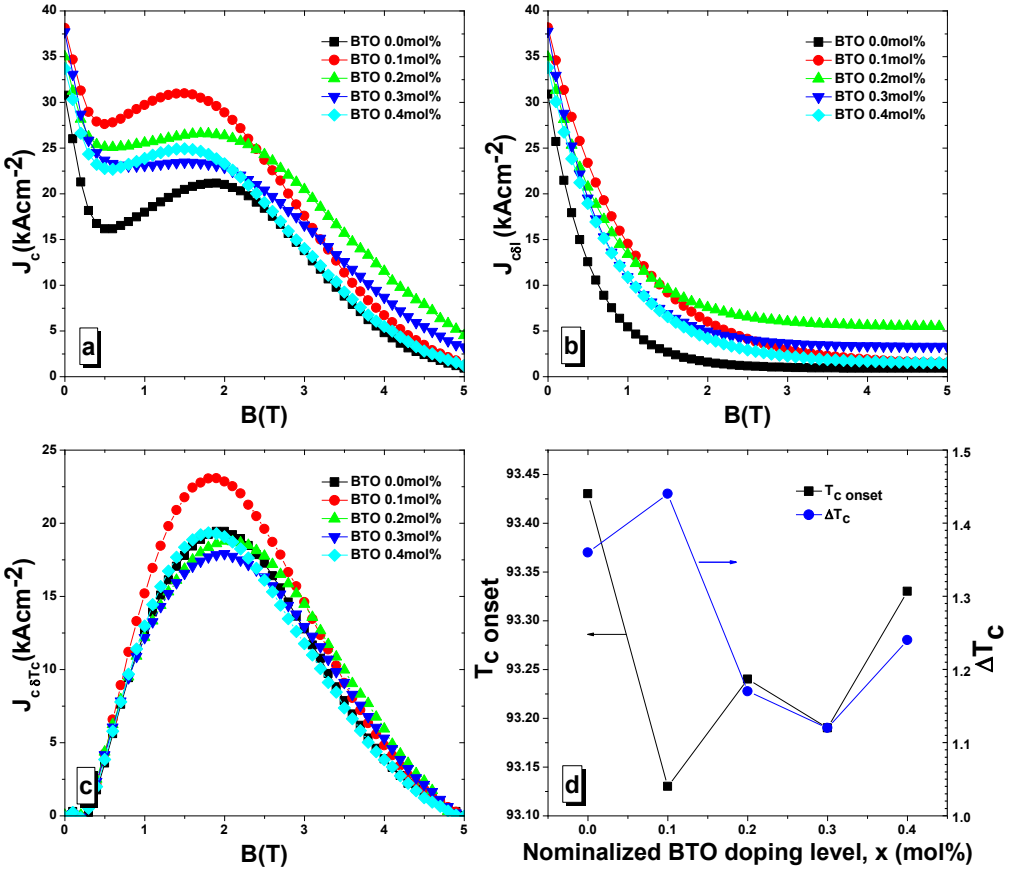

Fig. 3-2 (a). J_c as a function of applied field at 77 K with *B*//c-axis; (b) the calculated $J_{c\delta l}$ – *B* curves based on (a); (c) the deduced $J_{c\delta Tc}$ – *B* curves. (d) The doping ratio dependence of both the onset T_c and ΔT_c.

However, according to the previous results in ref. 18, J_c can be enhanced by doping with BaO_2, $BaCO_3$ or $BaCuO_3$ in the range of 5 - 15 mol%, and leads to a decreased T_c and narrow transition width ΔT_c. Gd/Ba solid solutions had been suppressed by a relatively larger doping amount. But considering our doping amount is one order of magnitude lower than their doping level, such suppression cannot explain the enhanced peak effect in 0.1-BTO. Therefore, more detailed factors are needed to be considered.

It is known that T_c of HTSs is extremely sensitive to the carrier (hole) density. Our results show that there are at least two kinds of pinning mechanism account for BTO doped bulks due to the sophisticated ion substitutions, which can be denoted as $Gd_{1+x}Ba_{2-x+y}Cu_{3-y}Ti_yO_{7-\delta}$ (x, y and δ marked as the variation of ion substitutes or vacancies). Nishi *et al.* have studied a system with a nominal composition of $YBa_2Cu_{3-x}Ti_xO_{7-y}$. They found that Cu sites substituted with a little amount (10^{-3}) of Ti and this causes an increase of T_c. The highest T_c was realized at x = 0.001 [21]. We also have done the experiment of TiO_2 doping in this bulk system (see chapter 4). The addition of TiO_2 particles in the range of 0.0 - 0.3 mol% in Gd-123 bulks leads to the increased T_c too. Muralidhar *et al.* studied the Ti doping effect in NEG-123 system and found that 0.1 mol% is the optimal doping

amount, whereas the onset T_c has a slight dropping with the increase of doping amount in the range of 0 mol% - 0.35 mol% [22]. In our interpretation, the slight dropping of T_c should be mainly attributed to the formation of NEG/Ba solid solution. On the other hand, Ti^{4+} has almost the same size with $Cu^{2+/3+}$ and tends to sit at $Cu^{2+/3+}$ site in RE-123 system [9]. It means that Gd^{3+}/Ba^{2+} sites were substituted by Ba^{2+} cause the decreasing T_c, while $Cu^{2+/3+}$ sites substituted by Ti^{4+} lead to an increased T_c. The final T_c will be determined by the combinations of those two kinds of ion substitution with the local lattice of Gd-123.

Based on the above scenario, we reinvestigate the pinning properties of 0.1-BTO according to Fig. 3-2. An interesting phenomenon is the highest peak in Fig. 3-2(c). It suggests that small doping amount of BTO caused an enhancement of superconducting chemical fluctuations, and reassured with both the lowest T_c and the widest ΔT_c in Fig. 3-2(d), which is originated from the enhanced Gd^{3+}/Ba^{2+} solid solution. On the other hand, such a small doping amount also leads to an enhancement of atom disturbed regions due to the entrant of Ti^{4+} and contribute to δl pinning, thereby, a highest J_c(B = 0) has been achieved in 0.1-BTO.

Diko *et al*. proved that the optimized substitution in CuO chain is x = 0.0013 in the nominal composition of $YBa_2(Cu_{1-x}M_x)_3O_{7-y}$ [23]. In this concentration，the mean distance $\lambda \geq 2\xi$, all CuO layers will be occupied by the dopant atoms and the spacing of these layers in the c-direction would be 1.2 nm. Those atom disturbed regions serve effective pinning centers and further raise J_c. Therefore, two kinds of ion substitution in the matrix with the addition of BTO will effectively contribute to J_c both at self and middle field in 0.1-BTO. The long distance of large pinning centers could be linked by those atom disturbed regions under zero fields or by the destroyed mediate superconducting phases of Gd^{3+}/Ba^{2+} solid solutions under middle field, respectively. The density of atom disturbed regions increases with increasing of BTO, it may cause a mean distance $\lambda \leq 2\xi$, and consequently, the vortex lines are not pinned, then the core pinning effect decreased above 0.1-BTO. On the other hand, Gd^{3+}/Ba^{2+} solid solutions were suppressed with more BTO doping, the superconducting chemical fluctuations were suppressed above the doping level of 0.1 mol%, hence, J_c shows a decrease at middle magnetic field with more additions, e. g. 0.2-BTO and 0.3-BTO, as shown in Fig. 3-2(c), which may relate to the tolerance of Gd-123 matrix. Correspondingly, the trend of the transition width ΔT_c decreased in those two specimens. In other words, the formed chemicals are mainly non-superconducting phases when the doping amount exceed 0.1 mol%. Those non-superconducting particles will mainly contribute to δl pinning. Therefore, 0.3-BTO can be looked as the optimized doping level in such a condition. While for 0.2-BTO, the active doping effect is that it has a largest B_{irr}.

Based on the above analysis, we stress that the BTO doping effect belongs to a novel pinning phenomenon, which is not simply consistent with BaO_2 doping and/or TiO_2 doping.

The difference between the above two procedures is Gd^{3+}/Ba^{2+} sites and $Cu^{2+/3+}$ sites were substituted simultaneously by the entrant of Ba^{2+} and Ti^{4+}, respectively. Those two kinds of ion substitution do not only cause a competition of superconducting properties but also lead to a novel pinning effect. In 0.1-BTO, Ti^{4+} substitutions mainly contribute to the δl pinning, while Gd^{3+}/Ba^{2+} solid solutions mainly contribute to the δT_c pinning. The unique growth condition and the same oxygen annealing allow us to regard that the contribution of oxygen vacancies to those two pinning mechanisms are no difference for all samples. After deviated from this optimized doping, the enhanced pinning is mainly attributed to the formed non-superconducting phases.

It is worth to note that $BaTiO_3$ is a perovskite ferroelectric. It has a similar structure with the subunit of Gd-123 and a high melting point of 1625 ˚C. It means that BTO could enter the crystal lattice of Gd-123 as a whole unit cell. Which might be the reason of the heights of peaks are almost the same with each other except 0.1-BTO in Fig. 3-2(c). Mounce *et al*. suggest that Abrikosov vortex lattice, characteristic of the mixed state of superconductors, becomes unstable under a high magnetic field (~5T) if there is charge trapped on the vortex core [24]. Their result gives us an additional evidence for such assumption. The in-field (>4T) J_c values show that the higher the doping amount, the lower the B_{irr}, in the range of 0.2 - 0.4 mol% (see Fig. 3-2(b)). It obeys the law of the charged core pinning dissipated model. Hence, ferroelectric BTO should be partially survived in the melting process if the doping amount exceeds the tolerance of Gd-123 and give a contribution to the enhanced core pinning. For further understanding of this issue, new evidences are needed to be found.

3.3.2 Pinning property for specimens closed to the seed

In order to clarify the possible influence of the seeds and to confirm the above mentioned scenario, we further measured the magnetic properties of the second set of rectangular tablets with a size of 2 mm × 2 mm × 2 mm, which were the residues of the first batch tablets. These residues are positioned below seed 0 mm (touch seed directly). We focus on the bulks with the doping amount of 0.0 mol%, 0.1 mol% and 0.3 mol%. The temperature dependences of normalized magnetic moment for all specimens were shown in Fig. 3-3. The J_c - B curves of the second batch tablets were shown in Fig. 3-5. As can be seen in Fig. 3-3, the onset T_cs of the second batch specimens are below 93 K for all of the samples, while the transition widths are obviously broad than those of the first batch samples. The reason is the elements Mg and Nd of seed have entered into the bulk due to ionic diffusion in the melting process, which deteriorates the superconducting properties of Gd-123. The deterioration further leads to a reduction of J_c at 77 K, hence, J_c (B = 0) values in Fig. 3-4 are all lower than that in Fig. 3-2(a) for each corresponding bulk.

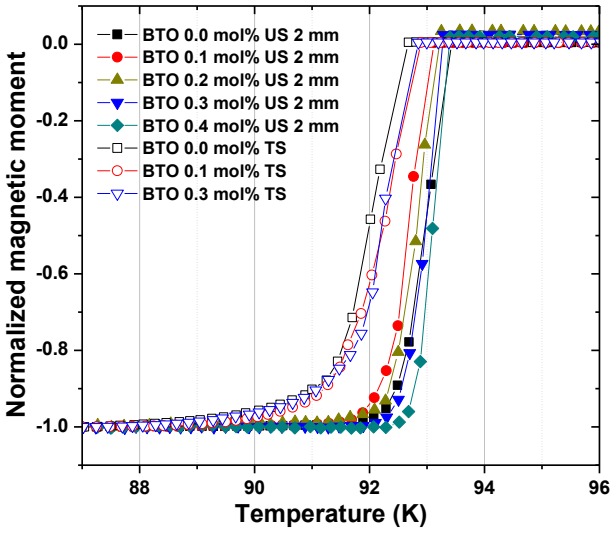

Fig. 3-3. Superconducting transition curves of all of the single domain samples cut from bulks with static magnetization measurement. US and TS in the legend are used to denote the samples positioned below the seed 2 mm and 0 mm, respectively.

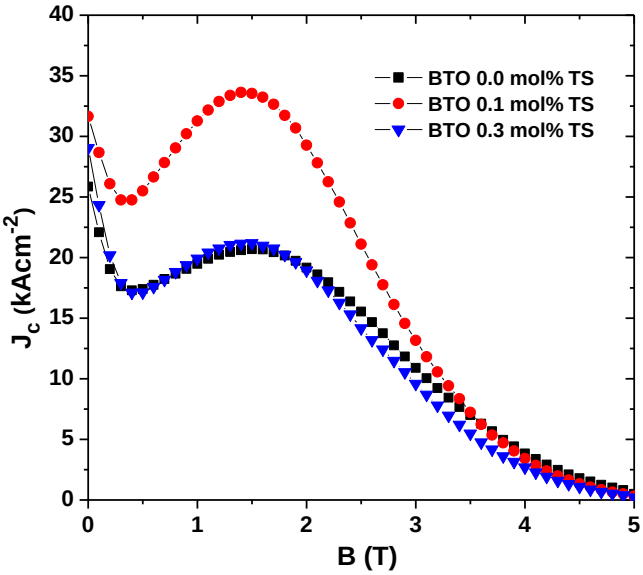

Fig. 3-4. J_c - B curves of the second batch tablets at 77 K.

The peak heights of the pure specimen of second batch (marked as 0.0-BTO-TS, other second set samples are also marked in this way hereafter) and 0.3-BTO-TS are almost the same as 0.0-BTO. It indicates that the influence of ionic diffusion of the seed on δT_c pinning is not prominent. It also proves the correctness of the existing of BTO or non-superconducting phases above 0.1 mol%, which mainly contribute to the core pinning, and Thereby, J_c (B = 0) value of 0.3-BTO-TS is larger than that in 0.0-BTO-TS. The lower J_c (B = 0) value in 0.3-BTO-TS in contrast to that in 0.1-BTO-TS is attributed to the ions diffusion of seed.

Another interesting phenomenon is the appearance of the significant peak effect in

0.1-BTO-TS as shown in Fig. 3-4, which is even higher than that in 0.1-BTO due to the ions diffusion and also has the largest value of J_c (B = 0). It confirms that 0.1 mol% BTO is with no doubt the optimized doping level and contributes to the both pinning types in Gd-123 system. At this point, an issue emerging: BTO has decomposed or not? If BTO has decomposed, it should have a similar pinning property with the double dopants of Ti and Ba, This work will be described in chapter 4. Considering the easy locally dislocated crystallization of Gd-123 as well as the similarity between the structure of BTO and the subunit of Gd-123, we conclude that BTO might enter the local dislocated crystal lattice of Gd-123 as a whole unit cell, Ti tends to occupy the CuO chain sites, but without broken CuO_2 layer, the properties of the new phases depend on the doping amount. Above 0.1 mol%, B_{irr} decreases with the increasing doping amount of BTO, which should relate to the charged pinning core due to the ferroelectricity of BTO.

3.3.3 Microstructure observations

The microstructure characteristics of BTO doped specimens were studied by means of scanning electron microscopy at the same magnification for the a-b plane and a high resolution for the a-c plane as shown in Fig. 3-5. The area for each sample was randomly selected and electron beams are perpendicular to the a-b planes for Figs. 3-5(a)–(e). Corresponding to the superconducting properties, the microstructure characteristics show that both clusters and the largest mean particle size of Gd-211 appeared in 0.0-BTO, as shown as the white circles in Fig. 3-5(a). This feature has made that the bulk has the lowest J_c. A similar phenomenon was also found in 0.4-BTO, but the mean size of Gd-211 was smaller than that in 0.0-BTO. While, for 0.1-BTO, 0.2-BTO and 0.3-BTO, there is no visible clusters, the mean particle size of Gd-211 is approximately same for each other, but smaller than that observed in (a) and (e), which is consistent with the J_c measurement. It indicates that Gd-211 could be made more fine by doping with proper amount of BTO in the range of 0.1 mol% - 0.3 mol%.

The cross point of the white lines in Fig. 3-5(e) shows a particle contains a small amount of Ti identified by EDX. However, the atom population of Ti is rather low. In order to find the particles contained more quantity of Ti, the a-c plane was also checked. As we have expected, it was achieved in the particles located at the white lines cross point in Fig. 3-5(f). The final nominal composition could be approximately written as $7GdBaCu_2O_{5-z}$ + $4BaTiO_3$. It reveals that the doped particles were surrounded by liquid phases and could be saved in the melting process. However, due to the low resolution of the equipment we not found the pure BTO particle.

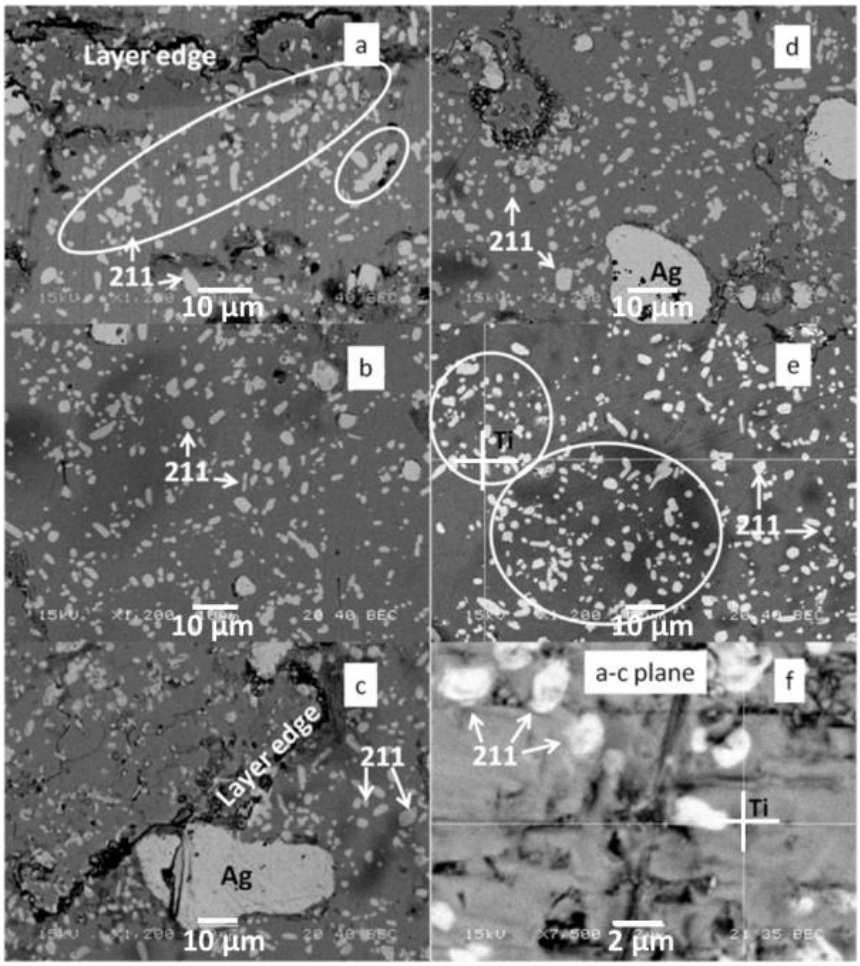

Fig. 3-5. Scanning electron micrographs of the specimens cut from the position under the seed. The scanned surface is in the a-b plane for (a) 0.0-BTO, (b) 0.1-BTO; (c) 0.2-BTO, (d) 0.3-BTO, (e) 0.4-BTO and a-c plane for (f) 0.4-BTO.Clusters were indicated by white circles. The black coarse irregular lines in both (a) and (c) are layer edges not cracks. Gd-211 and Ag were marked by white Arabic numbers “211” and black words “Ag” respectively. The cross point of the white lines in both (e) and (f) indicates two particles containing Ti.

3.4 Conclusion

The enhanced pinning effect has been achieved in the Gd-123 HTS bulks fabricated by using the cold seeding TSMG technique with different amounts of $BaTiO_3$ additive. Two optimal doping levels have been found out. One is the 0.1 mol% BTO, which has the largest J_c value under around remnant field and 1.5 T. The other optimal addition is 0.3 mol% BTO, which has almost the same J_c value compared to that of 0.1 mol% BTO around zero field. Present result indicates that BTO addition provides a novel pinning phenomenon, which may reveal the possible synergies of lattice mediation and interstitial BTO formation for the enhancement of flux pinning. BTO unit cell itself can be interstitial between Ba-O layers of Gd123 structure. Such BTO units may play a role of crystal defect and/or a new pinning center in the crystal lattice of Gd-123, which provides a doping dependent vortex pinning properties.

Equivalently, Gd^{3+}/Ba^{2+} and $Cu^{2+/3+}$ were substituted simultaneously by the entrant of Ba^{2+} and Ti^{4+}, respectively. Those two kinds of ion substitutions cause a competition of superconducting property (e.g. T_c) and lead to a novel pinning effect (e.g. the two optimized doping amounts). In 0.1-BTO, Ti^{4+} ions occupy $Cu^{2+/3+}$ sites of CuO chain and contribute to the δl pinning by the atom disturbed region, while Gd^{3+}/Ba^{2+} solid solutions mainly contribute to the δT_c pinning. For 0.3-BTO, The enhancement of J_c around self-field was mainly caused by the non-superconducting phases which may include the survived $BaTiO_3$ particles.

Microstructure observations show that Gd-211 particles are finer with proper BTO doping amount ranging from 0.1 mol% to 0.3mol%. But the pure $BaTiO_3$ particles have not been found because of the low resolution of EDX. As a whole, without any pre-treatment, the total J_c for each specimen is not very prominent due to the relatively larger mean size of commercial Gd-211, but the doping effect of ferroelectric BTO is considerable prominent. The higher peak in 0.1-BTO-TS compared to that in 0.1-BTO further stressed the important role of BTO.

References

[1] D. Larbalestier, A. Gurevich, D. M. Feldmann and A. Polyanskii, *Nature* 414 (2001) 368.

[2] L. Civale, A. D. Marwick, T. K. Worthington, M. A. Kirk, J. R. Thompson, L. Krusin-Elbaum, Y. Sun, J. R. Clem and F. Holtzberg, *Phys. Rev. Lett.* 67 (1991) 648.

[3] T. Haugan, P. N. Barnes, R. Wheeler, F. Meisenkothen and M. Sumption, *Nature* 430 (2004) 867.

[4] M. Murakami, H. Fujimoto, S. Gotoh, K. Yamaguchi, N. Koshizuka and S. Tanaka, *Physica C: Superconductivity* 185-189 (199) 1321.

[5] M. Muralidhar and M. Murakami, *Physica C* 309 (1998) 43.

[6] M. Tomita and M. Murakami, *Nature* 421 (2003) 517.

[7] G. Fuchs, G. Krabbes, K. H. Müller, P. Verges, L. Schultz, R. Gonzalez-Arrabal, M. Eisterer and H. W. Weber, *J. Low Temp. Phys.* 133 (2003) 159.

[8] R. Cloots, T. Koutzarova, J. P. Mathieu and M. Ausloos, *Supercond. Sci. Technol.* 18 (2005) R9.

[9] M. Muralidhar, T. Masaru and J. Milos, *Superconductor,* ed A. M. Luiz: InTech (2010) 203.

[10] D. A. Cardwell, Y. H. Shi, N. H. Babu, S. K. Pathak, A. R. Dennis and K. Iida, *Supercond. Sci. Technol.* 23 (2010) 034008.

[11] N. H. Babu, E. S. Reddy, D. A. Cardwell and A. M. Campbell, *Supercond. Sci. Technol.* 16 (2003) L44.

[12] C. X. Xu, A. M. Hu, M. Ichihara, N. Sakai, I. Hirabayashi and M. Izumi, *Supercond. Sci. Technol.* 19 (2006) 1285.

[13] M. Muralidhar, N. Sakai, N. Chikumoto, M. Jirsa, T. Machi, M. Nishiyama, Y. Wu and M. Murakami, *Phys. Rev. Lett.* 89 (2002) 237001.

[14] A. M. Hu, C. X. Xu, M. Izumi, I. Hirabayashi and M. Ichihara, *Appl. Phys. Lett.* 89 (2006) 192508.

[15] Y. Xu, M. Izumi, K. Tsuzuki, Y. F. Zhang, C. X. Xu, M. Murakami, N. Sakai and I. Hirabayashi, *Supercond. Sci. Technol.* 22 (2009) 095009.

[16] L. Simon-Seveyrat, A. Hajjaji, Y. Emziane, B. Guiffard and D. Guyomar, *Ceram. Int.* 33 (2007) 35.

[17] M. Muralidhar, K. Suzuki, A. Ishihara, M. Jirsa, Y. Fukumoto and M. Tomita, *Supercond. Sci. Technol.* 23 (2010) 124003.

[18] C. X. Xu, A. M. Hu, N. Sakai, M. Izumi and I. Hirabayashi, *Supercond. Sci. Technol.*

18 (2005) 229.

[19] Y. Xu, A. Hu, C. Xu, N. Sakai, I. Hirabayashi and M. Izumi, *Physica C* 468 (2008) 1363.

[20] D. X. Chen and R. B. Goldfarb, *J. Appl. Phys.* 66 (1989) 2489.

[21] Y. Nishi, S. Moriya and S. Tokunaga, *J. Mater. Sci. Lett.* 7 (1988) 359.

[22] M. Muralidhar, M. Jirsa and M. Tomita, *Physica C* 470 (2010) 592.

[23] P. Diko, V. Antal, K. Zmorayová, M. Šefčiková, X. Chaud, J. Kováč, X. Yao, I. Chen, M. Eisterer and H. W. Weber, *Supercond. Sci. Technol.* 23 (2010) 124002.

[24] A. M. Mounce, S. Oh, S. Mukhopadhyay, W. P. Halperin, A. P. Reyes, P. L. Kuhns, K. Fujita, M. Ishikado and S. Uchida, *Nat. Phys.* 7 (2011) 125.

Chapter 4 Vortex Pinning Behaviors Mediated by the Addition of Barium Dioxide, Titania and Barium Titanate

4.1 Introduction

From chapter 3, we have learned the very special characteristics of the dilute addition of barium titanate, the complexity of Gd-123/Ag system as well as key factors contributed to peak effect for instance the weak superconducting phases. In particular, our interest was lifted up by the two optimized doping levels which may imply a significant route on the control of vortex pinning. One question naturally emerging: why the vortex pinning behavior is so sensitive to the doping levels? It is necessary to consider a little more since the doping levels are very low. The dopant is occupied thousandth of the superconducting matrix in molar ratio only. A plausible conclusion is that the doping related products change with changing of doping levels. Our main consideration comes from the structural effect of barium titanate due to its perovskite crystal structure. It has the same structural unit with RE-123 as shown in fig 1-5. Ion substitutions occurred in a novel way by diffusing ions with weak bond to each other and result in chemical fluctuations both for superconducting matrix and dopant. In other words, we have a sense that the magnitude of pinning potential posed by one defect is highly related to its characteristic of conductance. Different doping levels bring out different products with different conductance characteristics. Generally, the higher peak effect is emerging together with the reduced transition temperature as well as the increased weak superconducting phase. It is also correct in the reversed description. Therefore, a dilute doping with Ti element only was performed and stressed in this chapter. Gd/Ba solid solutions are well known as weak superconducting phases. We hope to find what will happen in the bulk system when eliminating the mediation of Ba element. As our expectations, enhanced transition temperature and reduced peak effect were obtained simultaneously, and then we confirmed the correctness of our sense mentioned above.

In addition to the dilute Ti doping, a comparative study was performed by employing the addition of $BaTiO_3$, BaO_2 plus TiO_2 and BaO_2, by which we could find keys to control vortex pinning. For example, BaO_2 has a low melting point and will be melted during the melt processing, while Cu site have been occupied with the addition of TiO_2. In contrast, the addition of $BaTiO_3$ exhibits its special characteristic in aspect of this consideration. Experimental procedures and results are described in the following texts.

4.2 The addition effect of TiO_2

To highlight the structural effect of the addition of $BaTiO_3$ and give deeper understanding of vortex pinning, we performed the dilute addition effect of TiO_2 in the range of 0.1 – 0.3 mol.%.

4.2.1 Experimental procedure

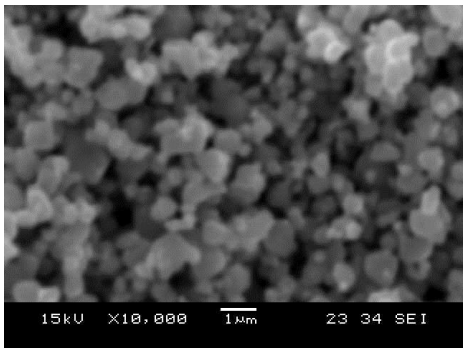

Figure 4-1 SEM micrograph of TiO_2 particles. The particle size is ranging from100 nm to 1500 nm after ball-milling process.

In order to reduce the particle size of commercial TiO_2 powder, the ball-milling treatment has been conducted for four hours by using Y_2O_3-ZrO_2 ball. Scanning electron microscope (SEM; JSM 5600) indicated the size of the particle is in the range from 100 nm - 1500 nm as shown in Fig. 4-1. Commercial powders of Gd-123 (3N), Gd-211(3N), Ag_2O (3N) and Pt were used as the starting materials for TSMG process. Gd-211 and Gd-123 powders were mixed as precursor with a molar ratio of Gd-211 : Gd-123 = 0.4 : 1. Different amounts of TiO_2 in molar ratio to Gd-123, 10 wt.% Ag_2O and 0.5 wt.% Pt were weighed and added to the precursor.

The precursor composition is as follows: Gd-123 + 0.4 Gd-211 + 10 wt.% Ag_2O + 0.5 wt.% Pt + x mol.% TiO_2 (x = 0.0, 0.1, 0.2 and 0.3). The mixtures were uniaxially pressed into pellets of diameter 20 mm and in 10 mm thickness under a pressure of 20 MPa. The pellets were placed onto Y-stabilized ZrO_2 supporting rods and then melt grown in air in a conventional box furnace by using hot seeding method. Nd-123 single crystals were used as seeds. The temperature profile is shown in fig. 2-14. The prepared pellet was heated to 1100 ˚C for 14 hours, maintained there for 1 hour, then, was cooled rapidly to 1040 ˚C in 30 minutes and maintained there for 2 hours for seeding. The samples were further rapidly cooled to 1015 ˚C, then we started single grain growth from 1015 ˚C to 995 ˚C with a cooling rate 0.25 ˚C/h and from 995 ˚C to 970 ˚C with a cooling rate 0.45 ˚C/h, respectively. Eventually, it was cooled to 20 ˚C in 10 hours. The process of post-annealing in oxygen was performed as follows: the oxygen pressure was 0.1 MPa; the sample was heated to 450 ˚C in 5 h, hold there for 40 h and the temperature was slowly decreased to 350 ˚C in 140 h, 300 ˚C in 30 h and cooled down to room temperature.

For the dc magnetization measurement, the rectangular tablet of 2 mm × 2 mm × 1 mm was cut from each sample. Superconducting properties were measured by using a SQUID magnetometer (Quantum Design, MPMS-XL). The measurement was performed

under the magnetic field applied parallel to the *c*-axis. Both the onset of critical temperature T_c and the transition width ΔT_c were evaluated from the results by zero-field cooling. The hysteresis loops up to 5 T at a constant sweep rate of 0.07 $Tmin^{-1}$ were obtained at 77 K. The critical current density J_c value was deduced from the magnetization hysteresis loop by using the extended Bean's critical state model.

4.2.2 Results and discussions

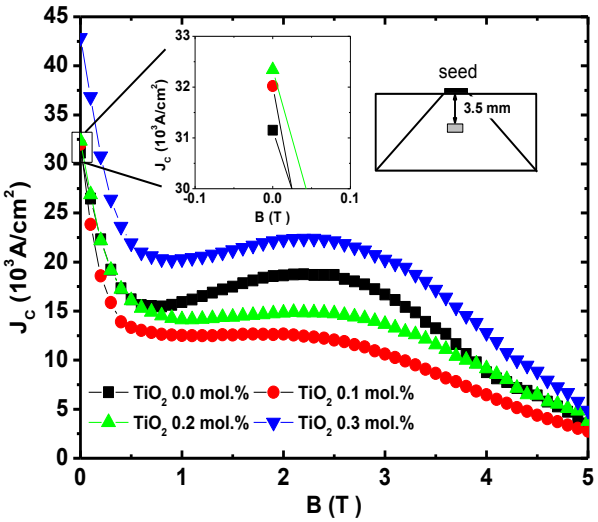

Figure 4-2 The critical current density as a function of magnetic field for the samples with different compositions of TiO_2. The left inset shows the enlarged J_c - B profile for x = 0.0, 0.1 and 0.2. The right inset illustrates the position of the samples in the bulk.

Fig. 4-2 shows the critical current density J_c as a function of applied field for the samples cut from a part under the seed with a distance of 3.5 mm. J_c value under zero-field increases from x = 0.0 to x = 0.2 as shown in the inset of Fig. 4-2. The J_c values in the sample with 0.3 mol.% TiO_2 exhibits the enhancement from 0 T to 5 T, indicating that TiO_2 is an effective additive for the enhancement of vortex pinning in Gd-123 bulk superconductors. Fig. 4-3 shows the transition curves for the samples in Fig. 4-2. The transition temperatures for different addition levels are higher than that of 93.5 K appeared in the reference sample without addition. The onset T_c is 93.9 K for x = 0.2. When x = 0.3, the onset T_c is also reached to a higher value of 93.8 K. Therefore, TiO_2 addition shows an ability of enhancing the superconductivity. In this regard, the optimal addition level is 0.2 mol.%.

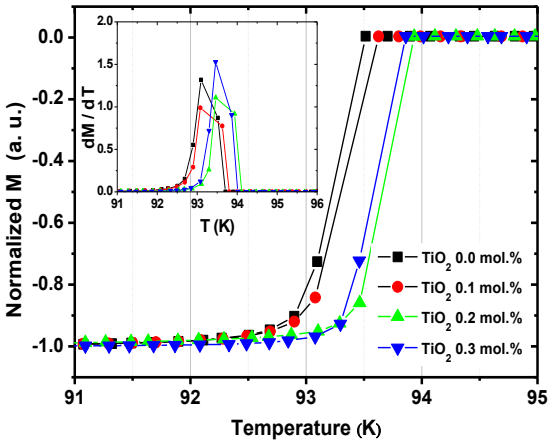

Figure 4-3 The normalized dc magnetization as a function of temperature for the samples with different addition levels of TiO_2. The inset illustrates the differential magnetization of the transition curves.

Table 4-1 Ionic radius of the relevant elements in different ion valence

Gd	+3, 0.938 Å		
Ba	+2, 1.35 Å		
Cu	+2, 0.73 Å	+3, 0.54 Å	
Ti	+2, 0.86 Å	+3, 0.67 Å	+4, 0.605 Å

Different additives such as BaO_2, ZrO_2, ZnO, NiO, SnO_2, Co_3O_4, Fe_3O_4, Ga_2O_3 and Fe-B alloy [8, 10, 11, 16-21] usually lead to a decrease of T_c in the bulk RE-123. The present results show that TiO_2 dilute addition provides a positive contribution to the transition temperature in addition to the enhanced pinning effect. In contrast to the addition effect of $BaTiO_3$ described in chapter 3, the peak effect is suppressed with the addition of TiO_2, but the self-field pinning is enhanced, confirmed the relationship between the in-field pinning effect and the conductance of the doping related products.

We know that a higher T_c generally appears when large RE ions are substituted by smaller RE ions. Ionic radius of Ti is closed to Cu for the same ion valence as shown in table 4-1. Ti tends to occupy the Cu site in the Cu-O chain and leads to an analog change of O-Cu-O bond angle and forms high T_c superconducting phases. Owing to the deterioration of the formation of cooper pair, the ionic substitution with Cu site in CuO_2 plane, such as Zn and Ni addition, leads to a reduction of T_c. We propose that the presently doped Ti does not occupy the above mentioned sites since the superconducting transition temperature increases. Nishi *et al*. have studied a system with a nominal composition of $YBa_2Cu_{3-x}Ti_xO_{7-y}$ and they found that the Cu sites substituted with a little amount (10^{-3}) of Ti cause an increase of T_c [1]. The consistency between their results and our results indicates that the Ti occupies the Cu site preferentially in the CuO chain during the melting growth.

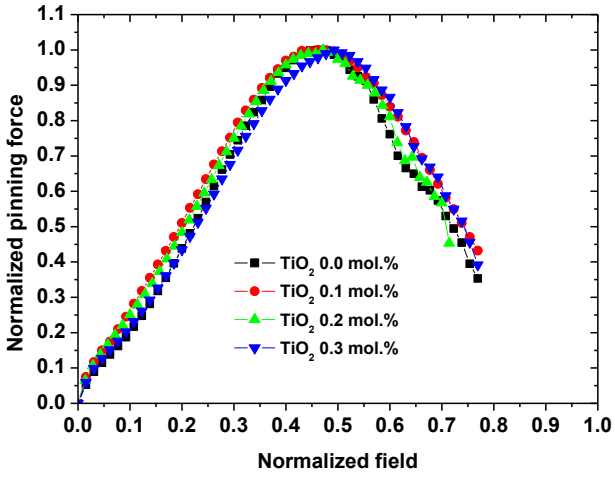

Figure 4-4 The normalized pinning forces versus normalized magnetic fields for the samples with different TiO_2 additions.

The peak effect in $J_c - B$ curves for RE-123 superconductors is originated from the clustered weak superconducting phases for example the Gd/Ba solid solutions. With increasing the external field, those clustered weak superconducting phases are forced into non-superconducting phases and contribute to the so-called δT_c pinning. In this case, the transition width is broadened due to a large gradient of superconducting phase. However, the transition widths are almost the unique in the present samples as shown in the inset in fig. 4-3, which proves that the TiO_2 addition is able to improve the superconductivity homogeneously. In order to study the pinning mechanisms, the normalized pinning forces versus normalized fields are shown in fig. 4-4. The irreversibility fields were estimated from the magnetization hysteresis loops. It shows that all peak positions h_0 locate above 0.4. Since h_0 ~ 0.5 suggests a characteristic of δT_c pinning, the present result shows δl pinning and δT_c pinning coexist, and δT_c pinning is dominant. This was also confirmed by a large transition width (~ 1 K) as shown in inset of Fig. 4. Therefore, despite the low peak heights in 0.1 and 0.2 mol.% doping samples, δT_c pinning is still main pinning mechanism in magnetic field. It can be understood as follows. TiO_2 addition suppresses the formation of weak superconducting phases and leads to the suppressed peak effect in Fig. 4-2. On the other hand, the peak position and B_{irr} in fig. 4-2 are located above 2 T and 6 T, which is higher than the general value of about 2 T and 5 T, respectively. As a result, the pinning force peak positions are located at higher values in fig. 4-4. In other words, the increased T_c brings about the clustered strong superconducting phases which transformed into non-superconducting phases under high magnetic field and thus results in the above mentioned phenomenon. Another noteworthy feature here is the plateau-like in-field pinning behavior.

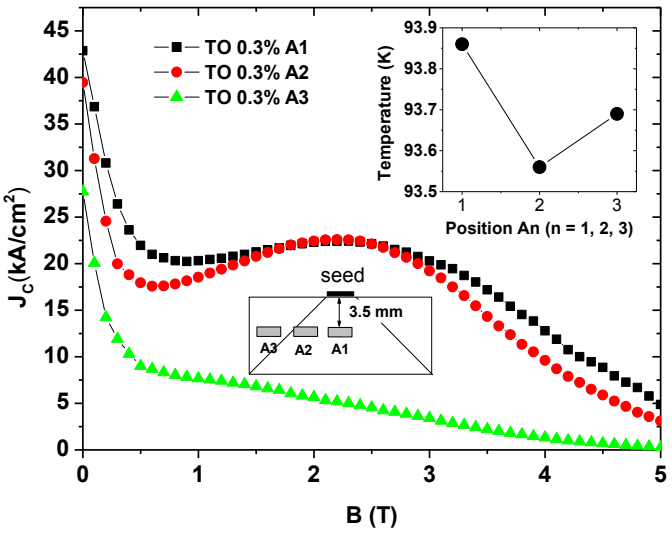

Figure 4-5 J_c – B curves of the specimens which locate at different positions A1, A2 and A3 for x = 0.3. The left inset illustrates the sample positions from which the rectangular tablets were taken. The right inset illustrates the onset T_c of each specimen.

J_c under low field (δl pinning) is enhanced for all doped samples, especially for x = 0.3 as shown in Fig. 4-3. This result is similar to that of $BaTiO_3$ addition in the same doping level. It could be attributed to the enhanced strains or dislocations owing to the disturbed regions by ion substitutions. Combining the J_c – B characterizations and the ion substitutions in the Cu-O chain, we suspect that those regions act as pancake like pinning centers [2]. Alternatively, TiO_2 addition may lead to the formation of $BaTiO_3$ because of the possible reaction between TiO_2 and superconducting matrix and cause the inadequate supply of Ba in the superconducting matrix. Recent study indicates that 0.4 mol% ZrO_2 addition in Gd123 results in $BaZrO_3$ [3]. Perovskite structure of ABO_3 is rather stable. In this way, the formation of $Gd_{1+x}Ba_{2-x}Cu_3O_y$ solid solutions is suppressed and thus also arises the enhancement of clustered strong superconducting phases. Owing to the similar perovskite structure between the added materials and the matrix, the enhanced vortex pinning under low field may originate from the ferroelectric $BaTiO_3$ particles, strains or dislocations.

In order to learn the homogeneity of vortex pinning in 0.3 mol.% doped sample, J_c – B curves measured from the positions cut along the a axis are shown in fig. 4-5. Better performance is realized in the position A1 and the pinning performance degrades along the a-axis. The specimen locates at A2 has a relatively strong peak effect. Correspondingly, the onset T_c shows the lowest value as shown in the right inset in fig. 4-5. However, this value is still higher than 93.5 K. The high transition temperature as well as the low but broadened peak effect is the typical feature of the dilute addition of TiO_2.

4.2.3 Conclusion

TiO_2 fine particles are effective additives for the enhancement of vortex pinning in the Gd-123 system. The dilute TiO_2 addition provides a positive contribution to the vortex pinning as well as the transition temperature. Ti tends to occupy Cu site in the CuO chain and leads to the formation of the high-T_c superconducting phases. On the other hand, those Ti substituted regions also contribute to the enhanced δl pinning owing to the enhanced strains, dislocations and the possible synthesized $BaTiO_3$. The enhancement of vortex pinning is realized in the addition range from 0.0 mol% to 0.3 mol%. The broadened peak effect may come from the pancake like vortices due to the specific ion substitutions. The extend B_{irr} could be attributed to the clustered strong superconducting phases.

4.3 Recrystallization of fine inclusions

By this comparative study of vortex pinning behaviors we first examined the possible state of the additions at high temperatures during the melting growth. We found that barium titanate exhibits very specific characteristics during the cooling process from the starting growth temperature. These specific characteristics are attributed to the semi-melting state which crystallized together with the solidification of the superconducting matrix and thus can be dispersed into smaller fragments due to the actions of anisotropic crystallization of the superconducting matrix. In the following texts, we propose such a scenario that has never been reported in previous literatures. This finding further leads to a significant discovery on the control of vortex pinning and this will be described in chapter 5.

As described in chapter 3 and section 4.2, the dilute doping is a crucial strategy for making fine and dense pinning sites in the textured RE-Ba-Cu-O bulk superconductors (RE denotes the rare earth elements such as Y, Gd, Nd, Sm etc.) [4-6]. Coherence length of RE-Ba-Cu-O superconductor is only several nanometers below 77 K, which is the scaling range of defect for the trapped vortex line [7]. Material processes generally result in the micrometer-sized particles or defects [8]. Therefore, the total pinning performance is low. After the special process of ball milling, the typical particle size, for example Gd211, can be reduced to tens nanometers [9]. Despite the inevitable Ostwald ripening, the vortex pinning has been improved. The disadvantage is that the nanometer-sized solid particles are easily pushed out due to the pushing effect [10]. Based on the secondary phase inclusions, dispersing small amount of exotic elements into the matrix, i.e. a dilute doping strategy, enables us to improve further the vortex pinning under the magnetic field [11]. Fine clustered weak superconducting phases were considered to be the main reason and many mechanisms are involved, such as oxygen deficiency, Ba-rich cluster, RE-Ba solid

solution and Cu site substitutions [5, 6, 12-16]. However, to our knowledge, there is still no experimental attempt so far on the investigation of the recrystallization of impurity during the melting growth. That is, the dopants are melted together with the matrix and recrystallized during the texturing of the single domain. The composition may not be the same as the initial material. Owing to the nature of liquid dispersion or the anisotropic growth of matrix, the recrystallization leads to the formation of fine particles other than the starting powder and we overcome the disadvantage of pushing effect. Here, the recrystallization of fine inclusions is investigated by employing the dopant $BaTiO_3$. The Ba site self-doping and the mixed BaO_2 and TiO_2 doping are performed as references.

4.3.1 Experimental procedure

$BaTiO_3$ was synthesized according to chapter 3 or ref. [17]. To reduce the particle size, commercial BaO_2 (3N), TiO_2 (3N), Gd211 (3N) and homemade $BaTiO_3$ powders were milled using Y_2O_3-ZrO_2 balls for 1 hour, 4 hours, 2 hours and 1 hours, respectively. Commercial Gd123 (3N) and milled Gd211 powders were mixed as precursor in a molar ratio 1: 0.4. 10 wt% Ag_2O (3N) was added to improve the mechanical properties and 0.5 wt% Pt (3N) was added to hinder the coarsening of Gd211. The precursor was ground for 4 hours in the automatic mortar and pestle. 0.1 mol% $BaTiO_3$, 0.1 mol.% TiO_2 + 0.1 mol.% BaO_2 and 0.1 mol.% BaO_2 in molar ratio to Gd123 was added to the samples and thoroughly reground by hand. The samples were pressed into pellets 20 mm in diameter and 10 mm in thickness under the pressure of 20 MPa. Nd123 thin film seed [Nd123 (500 nm)/MgO (100)] with a size of 2 mm × 2 mm × 0.5 mm was placed on the top center of each pellet. The pellets were placed onto Y-stabilized ZrO_2 supporting rods inside a conventional box furnace. The batch process of cold seeding melt-growth was adopted in air. The post-annealing in oxygen gas was performed as described in section 4.2.1 or ref. [17]. In the present experiments, the starting growth temperature T_{g1} was set to 8 ˚C above T_p. For $BaTiO_3$ doping, the starting growth temperature $T_{g1} = T_p + 2$ ˚C was taken for comparison as discussed below.

After the growth, the dimension of the bulks is about 8 mm thick and 16.5 mm in diameter. The representative view of the as-grown bulk is shown in fig. 4-5a. Figure 4-5b shows the top view after a slight polishing in which the thickness has become to 7.6 mm. For the trapped vortex study, the bulks were cooled down and magnetized in liquid nitrogen under 1 T. The trapped vortex density was mapped by using a Hall probe sensor with the gap of 0.5 mm from the top surface of the bulk.

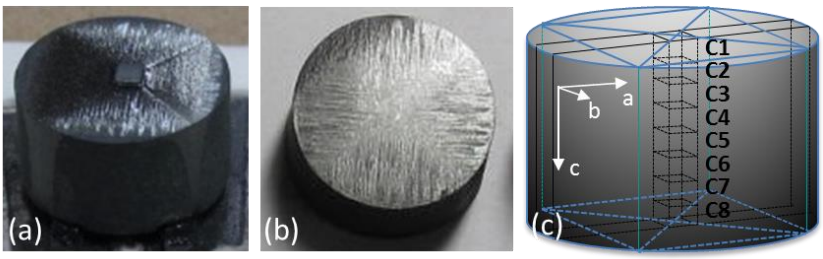

Figure 4-5 (a) Top view of the bulk with the addition of $BaTiO_3$. (b) Top view of the bulk after slight polishing provided for trapped filed mapping. (c). Illustration of the samples cut from different positions as C1-C8 from the single domain bulks. They were submitted to DC magnetization study.

For DC magnetization study, the samples of 2 mm × 2 mm × 0.9 mm in dimension were taken from the as-grown bulk. The positions from which the specimens are taken are illustrated in fig. 4-5c. DC magnetization was measured by using a SQUID magnetometer (Quantum Design, MPMS-XL) under the magnetic field 10 Oe applied parallel to the c-axis. The transition temperature was evaluated from the zero field-cooled (ZFC) magnetization curves. Magnetization hysteresis loops with magnetic field up to 5 T at a constant sweep rate of 0.07 T/min were obtained at 77 K. The values of the critical current density, J_c were deduced from the magnetization hysteresis loops by using the extended Bean's critical state model [18]. Scanning electron microscopy (SEM; JSM5600) was used to study the microstructure

4.3.2 Results and discussions

According to the cold seeding batch process, the conical trapped flux profiles exhibit the uniformly distributed contour lines as shown in figure 4-6a, 4-6b and 4-6c. These results confirm the well texturing of the single domain. The maximum trapped flux density, B_{max}, (the integrated trapped vortex, Φ) is 0.34 T (23.9 μWb), 0.35 T (23.9 μWb) and 0.37 T (24.6 μWb) for the BaO_2, $BaTiO_3$ and BaO_2+ TiO_2 doped bulks, respectively. Thus, the well textured single domain bulks allow us to investigate vortex pinning behaviors in detail.

The vortex pinning behaviors were examined by taken small specimens along the c-axis as shown in fig. 4-7 for $BaTiO_3$ doped sample. A serials of the second peaks was observed. It indicates that $BaTiO_3$ was melted during the melting growth and the clustered weak superconducting phases were formed. Secondly, the second peaks observed in the specimens taken from the positions of C3 to C6 show the similar maximum J_c with each other. The magnetic field at which the secondary peak of J_c becomes low as a function of depth along the growth direction of the c-axis and the pinning behaviors become stable starting from the position C5, i.e the J_c - B curves almost overlap with each other for C5 and C6.

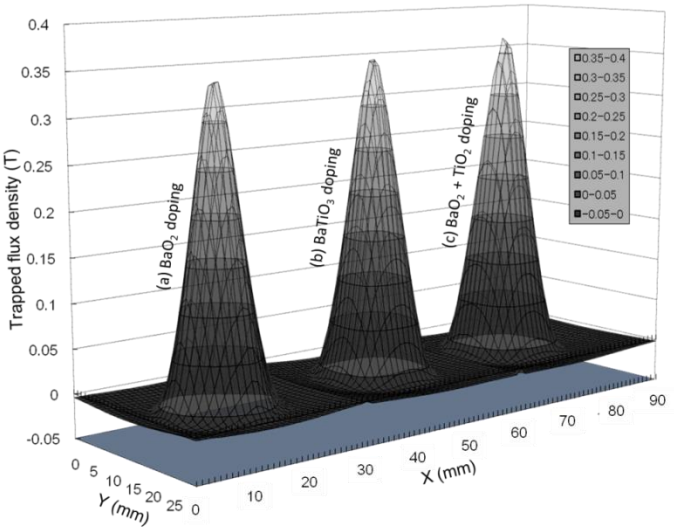

Figure 4-6 Trapped flux profile mapped on the (a) BaO_2 doped, (b) $BaTiO_3$ doped and (c) BaO_2 + TiO_2 doped single domain bulks, respectively.

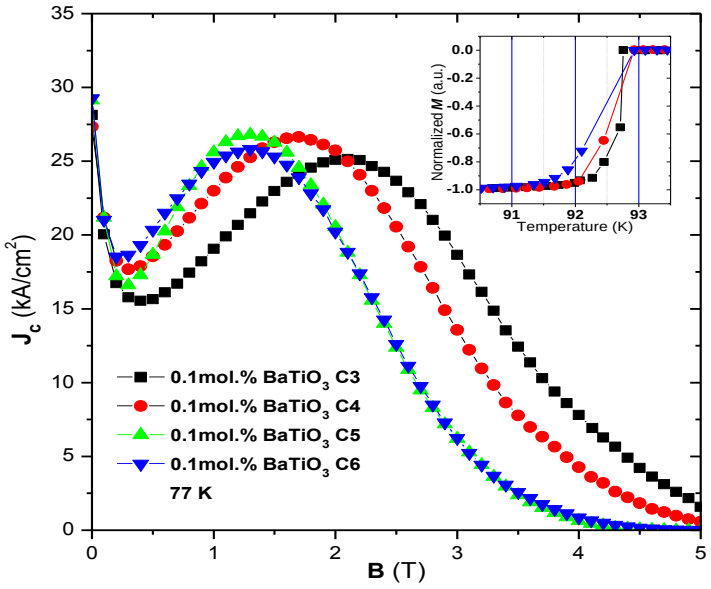

Figure 4-7 J_c as a function of B for the specimen taken from C3 to C6 positions in the bulk doped with $BaTiO_3$. Inset shows the corresponding superconducting transition curves of these specimens.

These behaviors suggest that the in-field pinning potential decreases along the c-axis and the density of the effective pinning sites remains almost unchanged. That is, the recrystallization rate of the compound related to $BaTiO_3$ is comparable with the matrix texturing rate and the distributions of these precipitations are rather homogeneous in the bulk. Thirdly, both the onset T_c and the transition width as shown in the inset of fig. 4-7 slightly increase in the specimens arranged along the c-axis, indicating that the gradient of the compositions of precipitations increases with decreasing growth temperature owing to the faster growth rate in the later growth stage. The almost the same J_c values in self-field

are originated from the homogeneously distributed Gd211 particles inside the matrix. Other doped samples show the qualitatively similar phenomena. The difference is the different evolution results of the pinning strength.

Figure 4-8a, 4-8b and 4-8c show the evolutions of vortex pinning behavior for the specimen taken from BaO_2, BaO_2 + TiO_2 and $BaTiO_3$ doped samples, respectively. Ba site self-doping, i.e. BaO_2 doping, shows an enhanced peak effect along the c-axis, but decreases for BaO_2 + TiO_2 doping, while they are almost the same with each other for $BaTiO_3$ doping. The observed evolutions reflect the differences of the absorption rates of additions by the growth front of matrix. For BaO_2 doping, effective dense and fine pinning sites are formed in the later growth stage, which shows an increased peak effect along the c-axis. This is a direct evidence of the nature of liquid dispersion which can be looked as a good reference for understanding of other doping related pinning behaviors as well as the possible melting states of the doping related precipitations. For BaO_2 + TiO_2 doping, the suppressed peak effect is obviously resulted from the contribution of the addition of TiO_2, which has an ability to suppress the peak effect as described in the section 4.2 or ref. 19. However, the suppression is not prominent for the specimen in position C3, which can be distinguished by comparing BaO_2 + TiO_2 doping with BaO_2 doping as shown in fig. 4-8b and 4-8a, respectively. That is, the gradient of the distribution of Ti ions is similar to that of Ba site self-doping along the c-axis. Presumably, such distribution is determined by the stoichiometry of crystallization of $GdBa_2Cu_3O_{7-\delta}$, because BaO_2 and/or TiO_2 doping effects originate from the ionic substitutions [19-21]. Therefore, the melted dopants density has a gradient in spatial distribution. This result is similar to the pushing or dragging effect reported in ref. [10]. There, it is noted that the role of the objects are solid particles.

Interestingly, $BaTiO_3$ doping does not seem to show such behavior as shown in figure 4-8c. The maximum values of the in-field total pinning strengths are almost the same, proving that $BaTiO_3$ doping related precipitations are crystallized simultaneously with the crystallization of matrix. It also indicates that despite the uncertain chemical reactions, $BaTiO_3$ provides independent cores whether in solid state or in colloidal state in the melting status of the matrix. That is, $BaTiO_3$ retains a specific state separated from the melting matrix and shows homogeneous recrystallization rates upon texturing. Presumably, such a characteristic state like a colloidal droplet with larger inner viscosity than the surrounding liquid at high temperature and can be divided into two or more fragments by the stretching forces with respect to the anisotropic growth of matrix. The present result inspired us to investigate $BaTiO_3$ doping effect by growing a new sample at a lower initial growth temperature with the same composition. Recrystallization of such special state may exhibit an outstanding role on the refinement of inclusions.

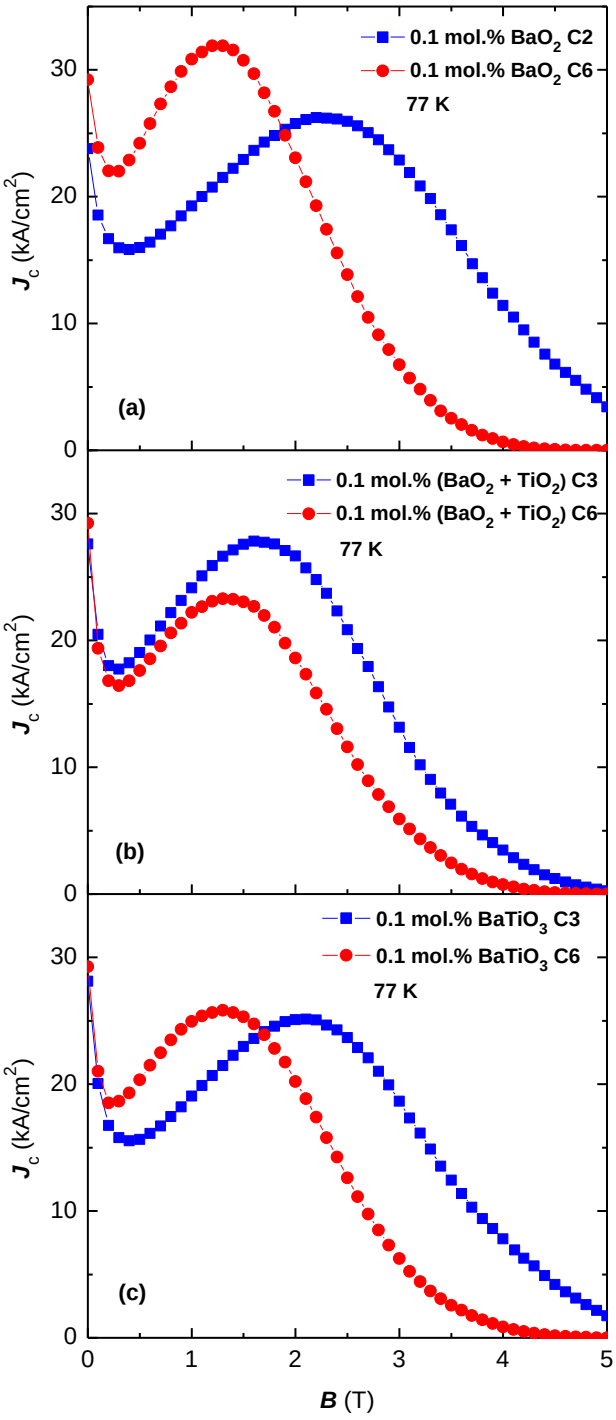

Figure 4-8 J_c as a function of B for the samples taken from C2 and C6 in the bulk doped with BaO_2 (a) and the specimens taken from C3 and C6 in the bulk doped with BaO_2 + TiO_2 (b) and $BaTiO_3$ (c).

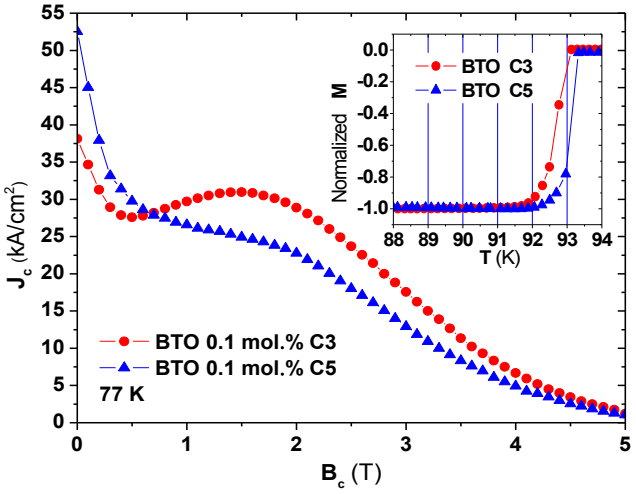

Figure 4-9 J_c as a function of B for the specimens taken from C3 and C5 positions of the bulk grown at the lower initial growth temperature with the addition of $BaTiO_3$. Inset shows the corresponding superconducting transition curves of these specimens.

Figure 4-9 shows the evolution of pinning behavior for the specimen taken from the sample grown with the starting growth temperature $T_{g1} = T_p + 2$ ˚C. Obviously, the pinning strength shows a remarkable increase under low field together with a decreased peak effect along the c-axis. This result indicates that the precipitations coming from $BaTiO_3$ doping may change from superconducting phases to normal conducting phases. This is an evidence of the recrystallization of finer inclusions from the colloidal droplets.

Otherwise, the composition should be more simple if $BaTiO_3$ retains solid state and chemical reactions happened in advance in the melting state of matrix. However, the property of $BaTiO_3$ doping related precipitation is determined instantaneously by the growth stages. Owing to the stretching forces generated by the anisotropic growth of matrix, the colloidal droplet has been divided into more smaller fragments imaginably and thus forming finer inclusions. On the other hand, BaO_2 doping provides a well reference for understanding the difference between colloid and liquid. Eventually, vortex pinning performance was improved prominently, the self-field J_c value reached up to 52.5 kA/cm^2 for the specimen taken from C5. In addition, thanks to the lower initial growth temperature, the onset transition temperature was also improved as shown in the inset in fig. 4-9. These results prove that the $BaTiO_3$ doping related precipitations are independent of the matrix, the positive effect of recrystallization of finer inclusions from the colloidal droplets is reasonably verified by growing the bulk at the lower initial growth temperature. Beside, Gd211 particle size was reduced too.

As shown in fig. 4-10, the average Gd211 particle size of $BaTiO_3$ doped sample with $T_{g1} = T_p + 2$ ˚C (fig. 4-10b) is obviously smaller than that of $BaTiO_3$ doped sample with $T_{g1} = T_p + 8$ ˚C (fig. 4-10a). Serious coarsening of Gd211 has been reduced. The dimension of

Gd211 particles are even reduced to several hundreds or tens nanometer as marked by the black arrows in fig. 4-10b. However, the self-field J_c values for the sample in position C3 were shifted from 28 kA/cm^2 in figure 3 to 38 kA/cm^2 in fig. 4-8c. This increase is smaller than the increased value observed in C5 under self-field in fig. 4-9. That is, the contribution of Gd211 on the enhancement of vortex pinning is finite [15], since the main Gd211 particles are still in the micrometer range. Therefore, the significantly increased pinning performance along the c-axis in low field was additionally attributed to the recrystallization of the finer $BaTiO_3$ doping related precipitations.

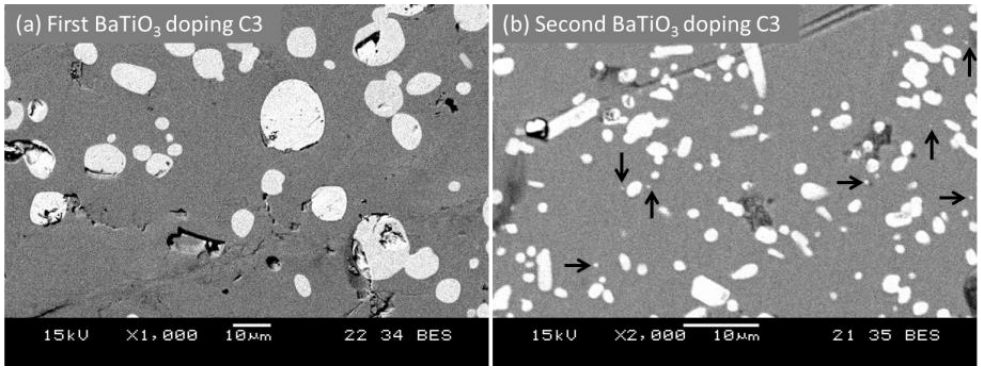

Figure 4-10 Scanning electron micrographs of the *a-b* plane for the specimens cut from the position C3 for (a) $BaTiO_3$ doped sample grown with the starting growth temperature T_{g1} = T_p + 8 ˚C and (b) $BaTiO_3$ doped sample grown with the starting growth temperature T_{g1} = T_p + 2 ˚C, respectively.

4.3.3 Conclusion

Single domain Gd–Ba–Cu–O bulk superconductors with dilute additions were successfully textured by using the top seeded melt growth. For the samples grown at high initial growth temperature, pinning strengths are not so large owing to the coarsening of Gd211 particles, but the trapped field exhibits a high conical profile for each bulk due to the homogeneously distributed pinning performance. Pinning evolution along the c-axis shows different pinning behaviors for the samples doped with different additions. It implies that $BaTiO_3$ retains a semi-melting state like a kind of colloid in the harsh ambient of the melting process which can be divided into more than one smaller fragment by the anisotropic growth of matrix and eventually forming the finer inclusions after recrystallization. Such scenario is supported by the sample grown at the lower initial growth temperature. Pinning performance was improved remarkably under low field together with decreased second peaks. Combined with the character of microstructure, the increased low-filed pinning performance was attributed to the recrystallization of finer inclusions and the reduced Gd211 particle dimension. It is worth to mention that the present conclusions not conflict with that in chapter 3 even ion substitutions occurred

because the possible chemical reactions mainly given modification of composition in local regions. In fact, the semi-melting state is originated from such reactions; otherwise the barium titanate should maintain its high melting point and act as normal pinning centers only. Therefore, ions exchanges have happened between dopant and matrix for the addition of $BaTiO_3$ and lead to the semi-melting state of the doping related products.

4.4 New understanding of peak effect

To date, the world-wide scientists attribute the peak effect to variety of mechanisms for instance oxygen vacancies, RE/Ba solid solutions, phase transition of vortex matter etc. However, those conclusions are mostly tailored only from specific samples and given a default scenario that those clustered weak superconducting phases are distributed randomly in the superconducting matrix. Scientific scenario of peak effect is actually still wrapped in mystery which obstructed the large-scale application of type-II superconductor. "How to control the vortex pinning in magnetic field" is hitherto still a big challenge. We deduced a clear scenario of the origin of peak effect by analysis of the specific characteristics of our samples in the following texts and given further direct evidences of this scenario in chapter 5, by which one could control the vortex pinning or critical current whether in zero, intermediate or high magnetic field and allows one to engineer practical superconducting applications with stable and high current-carrying ability.

4.4.1 Peak effect occurred in $BaTiO_3$-, TiO_2- and BaO_2-doped samples

To deduce the possible intrinsic mechanisms buried behind the J_c - B curves, it is necessary to examine carefully the vortex pinning features again with a new perspective. We believe that peak effect does not come only from the superconducting property of the doping related precipitations but the arrangements of those precipitations. As described in section 4.3.2, the difference between the evolutions of pinning performance is attributed to the different distribution of dopant. These differences are actually originated from the anisotropic crystal growth although this consideration was usually ignored in previous reports because of the complexity of the bulk system. In the following texts, we give a review of the peak effect occurred in the $BaTiO_3$-, TiO_2- and BaO_2-doped samples.

For BTO doping and BO+TO doping, the self-field J_c values are improved in contrast to the pure one as shown in fig. 4-11. The in-field J_c values are also improved, e.g. above 1 T for BO+TO-doped sample and above 1.5 T for BTO-doped sample. Therefore, BTO doping and BO+TO doping are all effective on the enhancement of flux pinning but with different pinning behaviors. The onset T_c of each specimen is lower than the expected value 93.5 K. However, the peak-field increases unusually with increasing of onset T_c

possibly due to liquid loss occurred during the melting process. The mixing BO and TO doping on the one hand compensates the inadequate supply of Ba and on the other hand causes ions substitution. Thus, the mixing doping leads to the highest second peak. BTO doping herein provides the similar contribution but with the highest onset T_c and the highest B_{irr}, suggesting clearly its specific characteristics on the mediation of flux pinning. If the increased onset T_c can be attributed to the compensation of liquid loss for the mixing BO and TO doping, such compensation has been enhanced further with the addition of BTO since it shows the highest onset T_c.

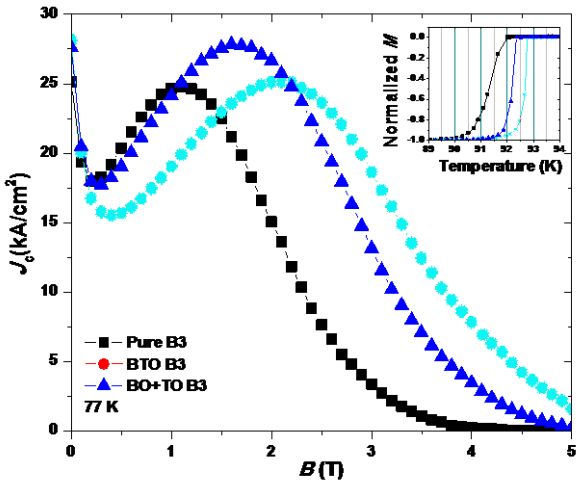

Figure 4-11 J_c – B curves for the specimens taken from B3 for the bulks grown in the HGT. Inset shows the corresponding superconducting transition temperatures.

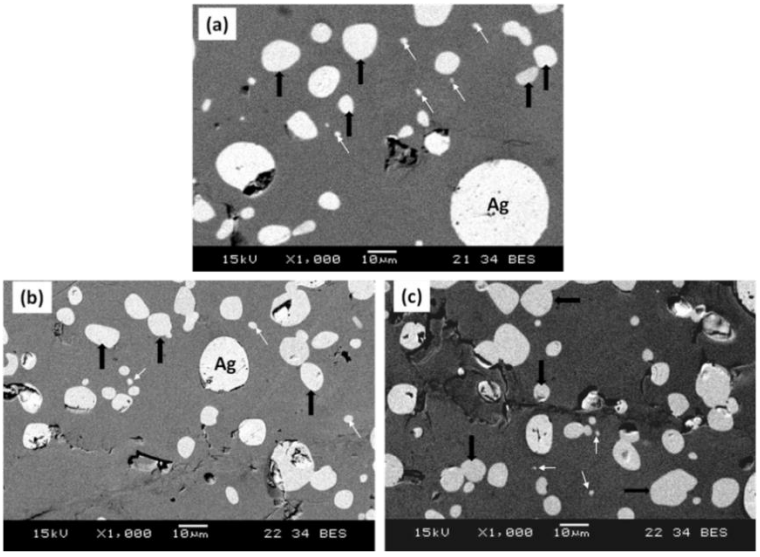

Figure 4-12 Microstructure of the specimen in position B3 cut from (a) pure bulk (b) BTO doped bulk and (c) BO+TO doped bulk, respectively.

The high starting growth temperature leads to the serious coarsening of Gd211 as shown in fig. 4-12. The large averaged diameter excess 5 μm has been observed as marked by the bold black arrows. Pt addition effect on suppressing the coarsening of Gd211

seemingly has been canceled out by the high growth temperature. The other group is the small ones as marked by the white arrows. They are still large and approximately excess 1 μm in diameter. Despite this large particle size they occupy only the minor proportion. Therefore, liquid loss and coarsening of Gd211 are the main origins of the deterioration of both J_c and T_c, whereas the deterioration has been suppressed with the present dilute additions.

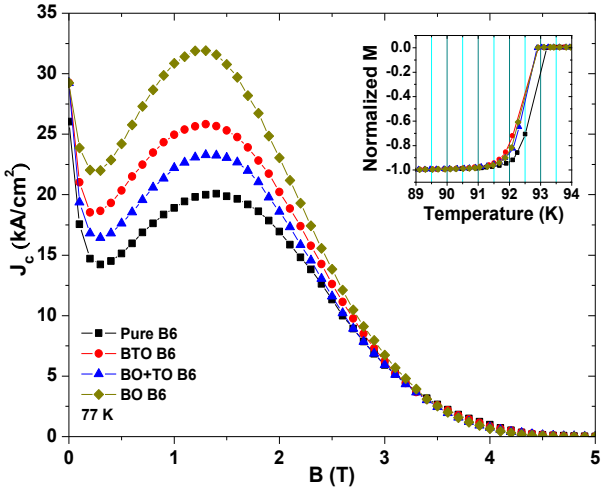

Figure 4-13 $J_c - B$ curves of the specimens in position B6 cut from all the bulks grown in the HGT. Inset shows the corresponding superconducting transition temperatures.

To highlight the contribution of each kind of addition further, J_c measured from the portion positioned at B6 were organized into one $J_c - B$ diagram as shown in fig. 4-13. BO-doped specimen was also added for the sake of comparison. The self-field J_c values are almost the same with that in position B3 and also almost the same with each other for the doped ones. Pushing effect can be ignored due to the serious coarsening of Gd211. The contributions of the additions are small too in self-field since the precipitations related to these additions are known as weak superconducting phases. Interestingly, $J_c - B$ curves show the similar behavior with the second peaks positioned in a narrow field ranged from 1.25 T to 1.5 T. The peaks are enhanced respectively with the addition of BO+TO, BTO and BO. In contrast to BO doping, second peak is suppressed for BO+TO doping due to the suppression effect of Ti [19]. BTO doping exhibits a compromise behavior with the peak higher than BO+TO doping and lower than BO doping. The composition of BTO doping related precipitations should be different with the joint BO+TO doping since BTO presumably reacts with the superconducting matrix as one material. Structure effect of the perovskite addition has been highlighted in section 4.3.2. On the other hand, the enhanced peaks in fig. 4-13 are obviously coming from the increased impurities provided by the additions. Whereas the different peak heights indicate that different precipitations provide different average pinning potentials. The total pinning potential is highly related to the

composition of precipitation. In spite of this consideration, another noteworthy feature is that these peaks seem to obey the same principle that needed to be clarified further carefully.

One can see that the second peaks in fig. 4-13 overlapped with each other in high magnetic field and in self-field for the doped specimens, while they are separated with each other from 0 T to 3 T, all these features imply that vortex pinning behavior is independent of the kind of dopant and may reflect importance of the crystalline itself for each specimen. We thus propose a possible scenario based on the anisotropic crystal growth. A fact is that fine and light precipitations or impurities are suspended in the liquids before starting growth. Anisotropic crystal growth involves the directional transport of liquid which has been revealed by the characteristic of the growth sectors and the crystalline stripes or the square of single domain as shown in fig. 4-5a and 4-5b. For this reason, the small and light additions suspended in the liquids will be steered into some kind of arrangement with a certain degree of order during the melting growth. Segregating the precipitations to grain boundaries most likely occurred since sub-grains of the textured sample were arranged usually into orderly arrays. Segregating heterogeneous nanoparticles or atoms to grain boundaries is a normal phenomenon in crystalline materials partly because grain boundaries are effective sinks for atomic defects and impurities [22-24]. The second peaks in fig. 4-13 can be understood by combining such a segregating scenario with matching effect between vortex lattice and geometric defect array or geometric pinning landscape. Scientists generally fall in confusion due to one phenomenon that the peak field usually increases with decreasing of temperature in RE-123 [25]. Such a behavior actually can also be solved by assuming that the spaces between the adjacent PCs decrease with decreasing of temperature. The spaces between the adjacent PCs have been mediated by point defects since point defects will be activated as effective PCs in low temperatures. Therefore, we have deduced for the first time a clear scenario that could be used to control the in-field pinning and thus control the current-carrying ability in magnetic field. In fact, such a scenario has been confirmed in our next experiment and will be described in chapter 5.

4.4.2 Discussions

Inspirations could be achieved easily if one would like to do a comparative study from fig. 4-2 and fig. 4-13. The peak effect exhibits similar but not the same characteristics. The relative low and broad in-field current-carrying ability or vortex pinning strength in fig. 4-2 highlight on the one hand the importance of superconducting characteristic of the inclusions which lead to the low and broad second peaks when they have higher transition temperatures and narrow and higher second peaks when they have weak superconducting

property. The relative low and broad second peaks in fig. 4-2 imply on the other hand the significance of ordered arrangement of the inclusions, especially the significance of the ordered arrangement of the nano-sized inclusions since pinning vortex lattice in high magnetic field and in high temperature require deeper pinning potentials. The individual defect is considered to provide only a weak pinning potential and unstable in trapping a vortex. Intensive pinning, i.e. regulation of vortex lines as well as vortex lattice into geometry, seems to be necessary. In spite of the pinning potential provided by some kind of defects, vortex pinning behavior will be determined by the forms of their arrangement. The relative low and broad second peaks appeared in fig. 4-2 may imply a scenario that nano-sized inclusions are arranged into columns in the ac plane and thus could provide the strong pinning potentials in high magnetic field. This is a reasonable hypothesis otherwise we could not understand the possible reasons behind the peak effect. The correctness of such hypothesis has been confirmed in chapter 5.

4.4.3 Conclusion

Now we could make a conclusion that so-called peak effect appeared in the RE-123 system is highly determined by two factors. One is that the relevant regions (chemical fluctuations) should exhibit superconducting property. The other is that the arrangement of those relevant regions should be arranged into some kind of patterns for providing high pinning potentials in magnetic field.

References

[1] Y. Nishi, S. Moriya and S. Tokunaga, *J. Mater. Sci. Lett.* **7** (1988) 359.

[2] G. Blatter, M. V. Feigel'man, V. B. Geshkenbein, A. I. Larkin, V. M. Vinokur, *Rev. Mod. Phys.* 66 (1994) 1125.

[4] C. Xu, A. Hu, M. Ichihara, M. Izumi, Y. Xu, N. Sakai, I. Hirabayashi, *Jpn. J. Appl. Phys.* 48 (2009) 023002.

[5] B. Li, D. Zhou, K. Xu, S. Hara, K. Tsuzuki, M. Miki, B. Felder, Z. Deng and M. Izumi, *Physica C* 482 (2012) 50.

[6] P. Diko, V. Antal, K. Zmorayová, M. Šefčiková, X. Chaud, J. Kováč, X. Yao, I. Chen, M. Eisterer and H. W. Weber, *Supercond. Sci. and Technol.* 23 (2010) 124002.

[7] Y. Ishii, J. Shimoyama, Y. Tazaki, T. Nakashima, S. Horii, K. Kishio, *Appl. Phys. Lett.* 89 (2006) 3.

[8] D. Larbalestier, A. Gurevich, D. M. Feldmann and A. Polyanskii, *Nature* 414 (2001) 368.

[9] K. Salama and S. Sathyamurthy, *Appl. Supercond.* 4 (1996) 547.

[10] R. Cloots, T. Koutzarova, J. P. Mathieu and M. Ausloos, *Supercond. Sci. and Technol.* 18 (2005) R9.

[11] M. Muralidhar, N. Sakai, M. Jirsa, M. Murakami, and I. Hirabayashi, *Appl. Phys. Lett.* 92 (2008) 162512.

[12] M. Muralidhar, S. Nariki, M. Jirsa, Y. Wu, and M. Murakami, *Appl. Phys. Lett.* 80 (2002) 1016.

[13] Y. Xu, A. Hu, C. Xu, N. Sakai, I. Hirabayashi, M. Izumi, *Physica C* 468 (2008) 1363.

[14] Y. Xu, M. Izumi, K. Tsuzuki, Y. Zhang, C. Xu, M Murakami, N. Sakai and I. Hirabayashi, *Supercond. Sci. and Technol.* 22 (2009) 095009.

[15] K. Xu, K. Tsuzuki, S. Hara, D. Zhou, Y. Zhang, M. Murakami, D. Nishio-Hamane and M. Izumi, *Supercond. Sci. and Technol.* 24 (2011) 085001.

[16] M. Muralidhar, N. Sakai, N. Chikumoto, M. Jirsa, T. Machi, M. Nishiyama, Y. Wu and M. Murakami, *Phys. Rev. Lett.* 89 (2002) 237001.

[17] B. Li, K. Xu, S. Hara, D. Zhou, Y. Zhang, M. Izumi, *Physica C* 475 (2012) 51.

[18] D. X. Chen and R. B. Goldfarb, *Journal of Applied Physics* 66 (1989) 2489.

[19] B. Li, K. Xu, S. Hara, D. Zhou, M. Izumi, *Physica C* 484 (2012) 112.

[20] A. Hu, H. Zhou, S. Nariki, N. Sakai, M. Murakami and I. Hirabayashi, *Supercond. Sci. and Technol.* 17 (2004) 545.

[21] C. Xu, A. Hu, N. Sakai, M. Izumi, I. Hirabayashi, *Supercond. Sci. and Technol.* 18 (2005) 229.

[22] W. D. Kingery, *J. Am. Ceram. Soc.* 57 (1974) 1.

[23] X. Bai, A. F. Voter, R. G. Hoagland, M. Nastasi, B. P. Uberuaga, *Science* 327 (2010) 1631.

[24] C. L. Jia, and K. Urban, *Science* 303 (2004) 2001.

[25] H. Küpfer, Th. Wolf, C. Lessing, A. A. Zhukov, X. Lançon, R. Meier-Hirmer, W. Schauer, and H. Wühl, *Phys. Rev. B* 58 (1998) 2886.

Chapter 5 Grid-like Nanowalls Formed by Inserting Nanoparticles into Grain Boundaries

5.1 Introduction

To this step, one may have an overall view now for the target of control of vortex pinning in the melt-textured Gd-Ba-Cu-O bulk samples. We have proposed a scenario in chapter 4 that weak superconducting phases and their ordered arrangement are fundamental parameters in control of the vortex pinning or the current-carrying ability in external magnetic field. The next goal herein is to make clear the possible pinning scenarios that may form in the superconducting matrix. We believe that the ordered arrangement of inclusions in the general Gd-123/Ag system may occur in local regions. Those local regions with geometric defect arrays may be dispersed further randomly in the superconducting matrix because of the interference of large secondary phases, pores and cracks and result in the symmetrical second peaks in the intermediate field at around 77 K. We did not made further explorations in this consideration but focused on a new and more fundamental issue --- "how to trap tunable vortex lattice by using only one pinning landscape".

5.2 Some relevant considerations

For carrying large current and reducing energy dissipation, engineering defects or pinning enters in high temperature superconductors (HTSs) to impede vortex motion is a long-standing issue [1,2]. The short coherence length of RE-Ba-Cu-O confines the dimension scale of defects within several tens nanometer. Some nanoparticles, e.g. YBa_2CuO_5, and nanorods, e.g. $BaZrO_3$, are well known as effective pinning centers in deposited films [3-7]. For these cases, the correlated pinning of columnar defects is stronger than the collective pinning of point defects, while the best pinning property corresponding to the synergetic combination of these two kinds of defects [5,6]. However, their random distribution leads to distorted vortex lines, thereof weakening the total pinning strength [8]. New pinning paradigm is no longer a simple, 'one vortex/one defect' challenge, but a 'vortex lattice/pinning landscape' puzzle [6]. We put the "vortex lattice/pinning landscape" puzzle boils down to the task of "stabilizing tunable vortex lattice with only one pinning landscape". Vortex matter exhibits rasterized behavior in intermediate-field [9,10]. Such behavior requires the pinning landscape being the three-dimensional geometric defect arrays (3D GDAs) to parallel vortex lines in the c-axis for collective/correlated pinning [6,10,11] and to accommodate vortex lattice in the ab-plane for commensurate pinning [8,12,13]. To date, in spite of the specific engineering of two dimensional geometric pattern in film [14], 3D GDAs are still absent in coated or textured RE-Ba-Cu-O superconductors.

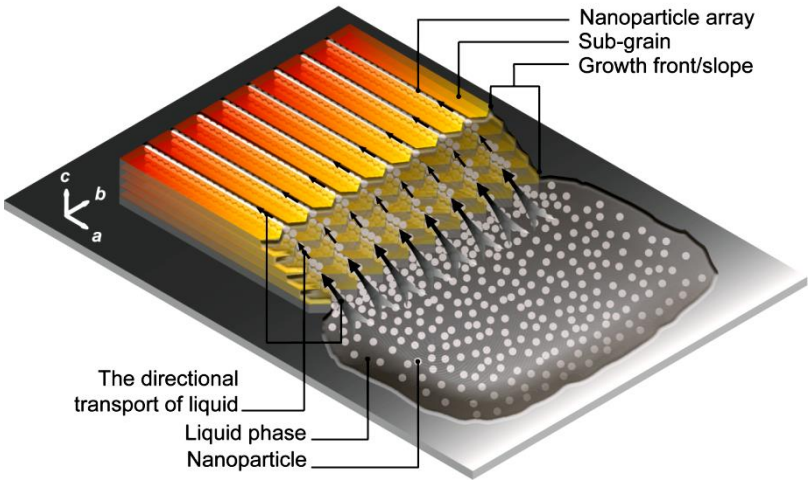

Figure 5-1 Schematic view of the scenario of inserting nanoparticles into grain boundaries in layered sub-grain arrays. The c-axis aligned linear nanoparticle arrays are assembled further into the grid-like nanowalls in the ac plane.

The hardness of engineering 3D GDAs is that there seems no passways to steer heterogeneous particles into orderly ranks. To approach the Holy Grail, we need the 'ordered channels' and the 'ordered driving forces'. Anisotropic solidification of RE-Ba-Cu-O superconductor involves the directional transported liquid, which hints the coexistence of 'ordered channels' and 'ordered driving forces'. Unfortunately, they were ignored in a long-term case and were usually masked by the large sized inclusions, typically in textured RE123/RE211/Ag bulk system, since the particles are too large to be driven. For this being widely studied system in the past two decades, the trapped field of the samples, 20 mm in diameter and 10 mm long, contained random defects, is usually 0.3- 0.5 T at 77 K [15,16], which is far from the estimated. The other record values mainly associate with large dimensions as well as low temperatures [17-19]. With chemical doping, J_c can be improved step by step with various sized inclusions [20,21], but further doping become invalid except reducing the particle dimension [22]. Nevertheless, this effort was easily canceled out by pushing effect and Ostwald ripening [23,24], consequently J_c values less exceed 10^5 A/cm^2 at 77 K. Pushing effect also leads to the spatial inhomogeneity of vortex pinning [25-27]. Engineering pinning centers in bulk system encountered more obstacles than that in the film. In fact, in spite of the hardness of reducing the defect dimension, their random distribution is hitherto being the top restriction for the further improvement of pinning performance in films and bulks. Bypassing these restraints and exploring new pinning paradigms, we believe that segregating nano-particles to grain boundaries (GBs) is a viable solution for approaching the 3D GDAs in textured bulk system. The 3D GDAs could be real-time portrayed by the 'ordered channels' and the 'ordered driving forces' associated with anisotropic crystal growth and eventually realizing the state-of-the-art pinning landscape.

Laminated structure and crystalline anisotropy of RE123 show rectangular sheet morphology for single crystal [28-31]. Superlamina [11,32-34] and banded structure [27,35] were found in textured bulks. All these features point to the fact that anisotropic crystal growth involves the directional transported liquid. We are more interested in the banded structure since GBs form weak links [36,37]. Turn this disadvantage into an advantage, filling GBs with nano-particles help to densify the matrix, improve the connectivity and simultaneously construct the 3D linear nanoparticle arrays. Imaginably, owing to the difference of solid and liquid, gaps/pores and immature GBs (IGBs) are commonly appeared in growth fronts (GFs). Corresponding to the banded structure, IGBs are supposed to resemble to sinks or capillary tubes depending on the local GFs. Continuing growth of the liquid-non-contacted GFs absorbs liquids through the sinks. Considering the liquid infiltration and the small width of sinks, capillary actions should be another kind of pump for liquid transportation. Nano-particles suspended in liquid are expected to be transported to the sinks through the liquid-contacted interfaces and to move continuously along the sinks driven by the 'ordered driving forces' of directional transported liquid, and settled down when liquids in sinks are not rich enough to support the particles floating because of the consumption of crystallization. After solidified fully, linear nanoparticle array will be buried inside the matrix. Such scenario has been shown in fig. 5-1. The linear particle arrays embedded in layered crystal assembled further grid-like nanowalls in the ac plane. Nevertheless, this scenario poses many severe experimental challenges. The final result will be determined jointly by the available nano-particles, the suitable particle densities, the geometry of IGBs and the growth rate of matrix, etc. More strictly, the particles should provide effective pinning potentials. In order to verify this scenario, two Gd-Ba-Cu-O prototype samples were textured: one was pristine and the other was $BaTiO_3$-doped. We first describe the experimental details in sections 5.3.

5.3 Experimental details

5.3.1 Cultivating textured bulk superconductors

Commercial Gd123 powder (TOSHIMA Co. Ltd, 99.9 %) acts as precursors. The two samples were made by using the top seeded melt growth (TSMG) technique as well as cold seeding method. Cultivating the pristine sample, Gd123 powder was pressed into a cylindrical pellet, 20 mm in diameter, in a uniaxial pressure of 20 MPa and was put into an alumina crucible. Nd123 thin film seed [Nd123 (500 nm) / MgO (0.5 mm)] with a size of 2 × 2 mm^2 was placed on the top surface of the pellet to nucleate the growth of a single domain inside a conventional box furnace. The pellet and seed arrangement were then heated rapidly to 1060 ℃, hold for 30 minutes, cooled rapidly to the starting growth temperature 1035 ℃,

and cooled slowly to 1020 ℃ at a rate of 0.2 ℃/h and finally furnace cooled down to room temperature. After the growth, a single domain with a size of 13.5 × 13.5 × 8 mm^3 was obtained as shown in fig. 5-2a. Making the nanoparticle-doped sample, 5.4 mol% $BaTiO_3$ was added to another precursor and mixed thoroughly. Melting point of the mixture determined by differential thermal analysis (DTA) is 1006 ℃. Similar to the procedure mentioned above, $BaTiO_3$-doped sample can be grown into a single domain with a starting growth temperature 1000 ℃ at a cooling rate of 0.2 ℃/h. Before further characterization, the samples were annealed in a flowing O_2 atmosphere (oxygen pressure: 0.1 MPa). The annealing temperature profile is as follows. The two samples were heated to 450 ℃ in 5 hours, hold for 40 hours, cooled to 350 ℃ in 140 hours, cooled to 300 ℃ in 30 hours, finally furnace-cooled to room temperature. After oxygen annealing, some white particles are observed on the surface of the pristine sample as shown in fig. 5-2d, whereas there is no difference for the doped sample as shown in fig. 5-5.

5.3.2 Characterizations

Rectangular specimen positioned ~ 1 mm away from seed was cut from the $BaTiO_3$-doped sample. The size of the doped specimen is approximately 1.5 × 1.5 × 0.5 mm^3. To observe the sink-shaped immature grain boundaries, one specimen was cut from the pristine sample ~ 1mm away from seed. The surface of the ab plane of pristine specimen was polished stepwise with sandpapers from coarse to fine, which has a final size of 1.96 × 2.00 × 0.93 mm^3. Microstructure observations were performed under a scan electron microscopy (SEM; JSM5600). SQUID magnetometer (Quantum Design, MPMS-XL) was used to measure DC magnetization. Magnetic field was applied parallel to the c-axis of the sample for all magnetization measurements. First, Zero-field-cooled magnetization was measured from 70 K to 90 K under 10 Oe to evaluate transition temperature. Second, magnetization hysteresis loop from -1 T to 5 T was measured at a constant sweep rate of 0.07 T/min at 40 K.

5.3.3 Calculation methods

Critical current density J_c was deduced from the magnetization hysteresis loop by using the extended Bean model: $J_c(H) = 20\Delta M(H)/a(1-a/3b)$. Pinning force density F_p was deduced from the $J_c - B$ diagram by using the formula: $F_p = J_c(H) \times H$.

5.4 Results and discussions

5.4.1 Crystal morphology of pristine sample

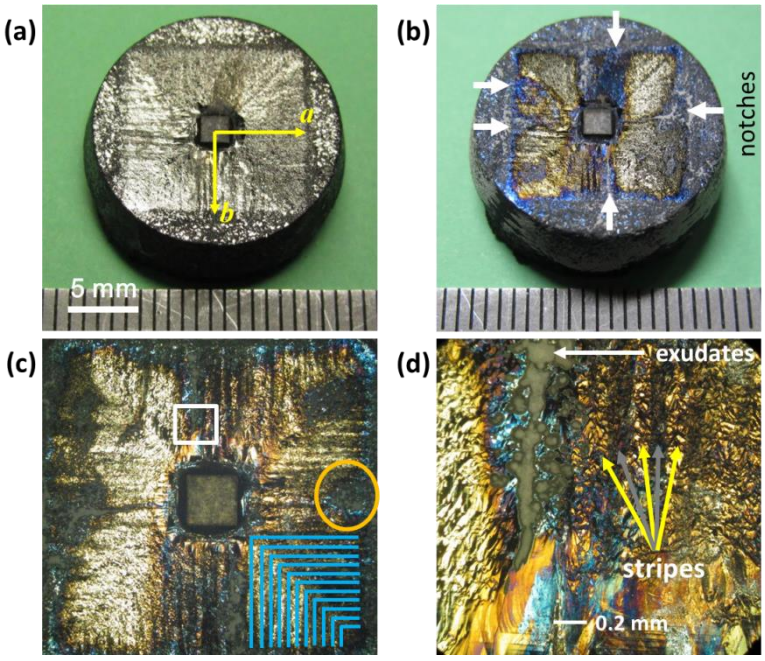

Figure 5-2 (a) – (d) show the top view of the single domain grown from the precursor composed of only Gd123. (a) The pristine single domain. **(**b) After oxygen annealing. (c) The annealed single domain under optical microscope. (d) The enlarged area locates in the white square in c under optical microscope.

Figure 5-2a shows the top view of the square single domain. The square shows four triangular growth sectors separated by the crossed looming diagonals. Looming banded structure or crystalline stripes (CSs) parallel to the a/b-axis were observed in each sector, suggesting the intrinsic crystalline anisotropy. After annealed in oxygen, as shown in fig. 5-2b, the square was modified, notches appeared, evidencing the weak welding (low angle GBs) of the laminated crystalline layers and of the macroscopic CSs. CSs can be seen more clearly under optical microscope as shown in fig. 5-1c. With respect to the diagonal, the adjacent CSs locate in the adjacent growth sectors assembled dendritic pattern and perpendicular with each other as marked by the white lines, suggesting that new CSs growing start from the diagonal. The diagonals become 90 ° GBs. The in-plane circular current flow will be hindered by these low and high angle GBs. Such stripes are the typical morphology of textured RE-Ba-Cu-O bulk superconductor, which hints the directionally transported liquid in melting growth. However, except known they are to be one origin of weak links, further explorations have less been done so far, since one cannot monitor the real-time melting growth spatially in the inside of the sample. Therefore, we will first describe a phenomenology interpretation of the directionally transported liquid from such kind of CSs.

5.4.2 Clues of directional transport of liquids

The region locates in the white square in fig. 5-2c was enlarged and shown in fig. 5-2d. Owing to the creeping up of liquid, the crystal-like solidified transition zone appeared around the seed. This is the first sign of liquid transportation. The periphery of the transition zone are the CSs with the alternate sharp contrast, which originates from the long-range propagation of anisotropic crystallization and the requirement of the lowest free energy of solidification. CSs are the second sign of liquid transportation. We know that solidification processing of RE-Ba-Cu-O material is complicated by the tendency of ceramic material to facet during solidification and by incongruent melting of the superconducting compounds [38]. Two factors are worth to be noted. One is the facet-type solidification, such as CSs, which provide the riverbed for liquid flow. The other is that the ternary equilibria in the RE-Ba-Cu-O freezing range involves the thermodynamic transportation of both the liquid phases (BaO + CuO) and the rear earth element released from RE211. Therefore, GFs are actually the power source of liquid transportation. In the present sample, with the extension of solidification, new long layered CSs are ripened and in turn guided the liquid transportation along the a/b-axis. The directional transported liquids are the source of the ‘ordered driving forces’ for moving the particles suspended in the liquid.

5.4.3 Evidence of sink-shaped immature grain boundaries

Next, we interpret the formation of sinks. Owing to the isotropic in-plane solidification of laminated crystal, immature CSs (ICSs) naturally breed IGBs, i.e. sinks. Such sinks can be deduced first from crystal morphology since it reflects the microscopic solidification procedure of crystal growth. One point is that the directional transported liquid unavoidably leads to the insufficient liquid supply in local, e.g. the center, the bottom and the edges of single domain. The loosing CSs were formed near the edges of the square and were melted during oxygen annealing due to the thermodynamic unstability. Consequently, CS vacancies appeared as shown in the circle in fig. 5-2c. Likewise, local insufficient liquid supply dynamically creates the microscopic in-plane ICSs, since the macroscopic CS is assembled with many microscopic ones, then the microscopic ICSs give birth to the microscopic IGBs/sinks. As described later, the microscopic ICSs and sinks have been clarified by means of the characteristics of microstructure.

Turn to solidification procedure of single domain growth, the diagonal growth vectors of the square or the cubic belong to resultant vector and mainly creating new CSs and expanding the dimension of single domain. Real growth vectors are oriented along the three axes. Corresponding to the oriented CSs, preferential liquid flow is running along the a/b-axis. They dynamically create new microscopic ICSs and IGBs. Limited by the

geometry of ICSs and the laminated crystal structure, final full growth compels liquid into IGBs. In other words, ICSs are growing up firstly but not fully: they first construct sinks and then the sinks are filled with the solidification of the liquids transported through the sinks. That is, solidification of Gd-Ba-Cu-O material involves two steps: first forming the long slim sink and second the slim sink to be filled with the solidification of liquids pumped from the periphery of the IGB arrays. This is the key for creating the 3D GDAs. Otherwise inserting particles into IGBs may be impossible. Finally, the exudates triggered by oxygen annealing in fig. 5-2d supports the existence of such sinks, which come from some bit particles transferred from inside to outside of the single domain through the slim channels buried in the matrix. Therefore, the sinks and the 'ordered driving forces' are considered to be the intrinsic features for melting growth of Gd-Ba-Cu-O superconductors.

5.4.4 Observation of sink-shaped immature grain boundaries

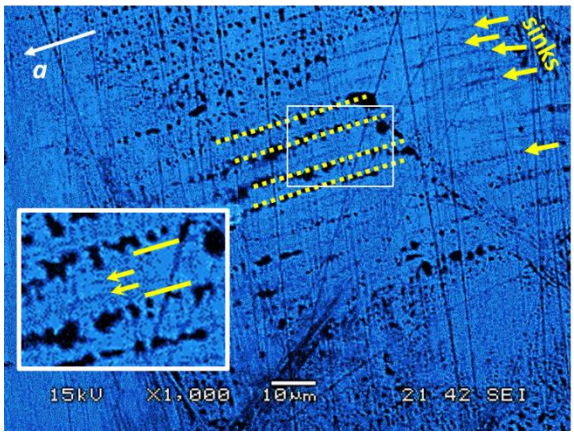

Figure 5-3 Characteristic of the low angle IGBs in ab-plane obtained from an insufficient growth region. The sinks were denoted with the white arrows. The dot lines denote the initial formation stage of low angle IGBs. The regions between the adjacent dot lines are the immature microscopic CSs. The region marked with the dotted rectangle in the rectangular was enlarged and shown in the inset, which shows how the CSs are formed and how the sinks are constructed. The two arrows in the inset denote the sinks being constructed. Pores assembled the initial formation stage of low angle IGBs. Two large Gd211 particles were also observed due to chemical segregation.

Given direct evidence of the existence of such sinks, microstructure of one insufficient growth region was shown in fig. 5-3, which is a good evidence for tracing back the history of melting growth. Consistent with the interpretations mentioned above, IGBs hundreds nanometer in width were observed as seen the dark line-like traces in front of the white arrows. Elongate areas between the adjacent sinks are the microscopic ICSs. Their micrometer widths are obviously much narrower than that of the macroscopic CSs shown in fig. 5-2d. The dot lines in fig. 5-3 show the initial formation stage of sinks. For clarity, the region in the dotted rectangle was enlarged and shown in the inset.

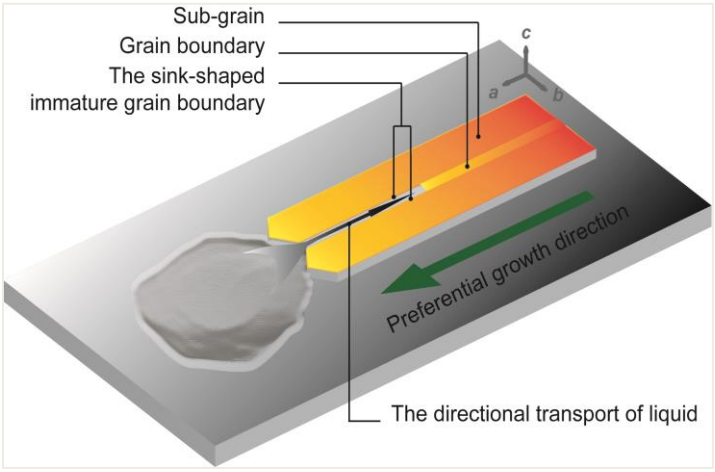

Figure 5-4 Schematic view of the two-steps solidification procedure.

Obviously, ICSs and IGBs/sinks are developed from the small solidified islands and pores. The two arrows denote the sinks are being constructed and closed step by step. From lower right corner to upper left corner, ripening of ICSs give birth to sinks as seen the front of the arrows. Full growth erases the sinks, the narrower ICSs emerged into a ripened wider one as seen the region between the two lines. Thus, present results confirmed the two-step solidification and clarified the existence of the IGBs/sinks. For clarity, the two-step solidification procedure is shown in fig. 5-4. Next, we describe how to fill them with heterogeneous particles for creating the 3D GDAs.

5.4.5 Some relevant considerations on selection of dopant

Segregating particles to IGBs, the particle size should be comparable with the width of sinks, meaning while, preferably have a smaller mass density for readily moving. In spite of possible chemical reactions occurred in melting process, ideal particles should be expelled by peritectic reaction of matrix and would be better if they are in a semi-melting state. $BaTiO_3$ particles may fulfill these strict requirements. Home-made $BaTiO_3$ particles show an average small size in a few hundreds nanometer. In contrast to the liquid phase, $BaTiO_3$ shows a smaller mass density which facilitates the readily moving along the narrow sinks and boosts vortex pinning on (001) interface due to the tendency of the bare CuO_2 layer appeared on the cleaved surface [39]. Most importantly, $BaTiO_3$ doped Gd-Ba-Cu-O superconductor exhibits the vigorous vortex pinning as shown in chapter 3 or ref. 26, showing a weak superconducting property. Further, the doping related precipitations show a trace of independence from the superconducting matrix. Similarly, large doping level of $BaTiO_3$ in YBCO seemingly converts into the new superconducting phase and also is independent of matrix [40]. Therefore, $BaTiO_3$ is considered to be a good candidate for engineering the 3D GDAs. The adjacent CSs and the intercalated superconducting precipitations in GBs may form sandwich structure as shown in fig. 5-1, which is speculated to trap vortices more effectively than random defects. Then, $BaTiO_3$-doped sample was textured for verifying the possibility of making linear nanoparticle arrays in Gd-Ba-Cu-O superconductor.

5.4.6 Crystal morphology of $BaTiO_3$-doped sample

Figure 5-5 shows the top view of a quarter of $BaTiO_3$-doped bulk sample. The single domain shows uniform crystal morphology without visible exudates on surface, indicating that the sinks buried in the pristine sample may have been filled with the addition. In contrast with fig. 5-2d, macroscopic CSs become finer, so that it is difficult to identify them clearly, e.g. the region between the dotted lines. The angle between the CSs and the diagonal was broadened as seen the solid lines on both sides of the diagonal. CSs return to approximately parallel to the a/b-axis when the position of CSs is far from the diagonal as seen the break line. These features reflect a dynamic modification of the orientation of CSs. The modification may not originate from the modified crystal structure but from the filled sinks, otherwise CSs should align uniformly or disappear. Microstructure characteristics described latter support such interpretation.

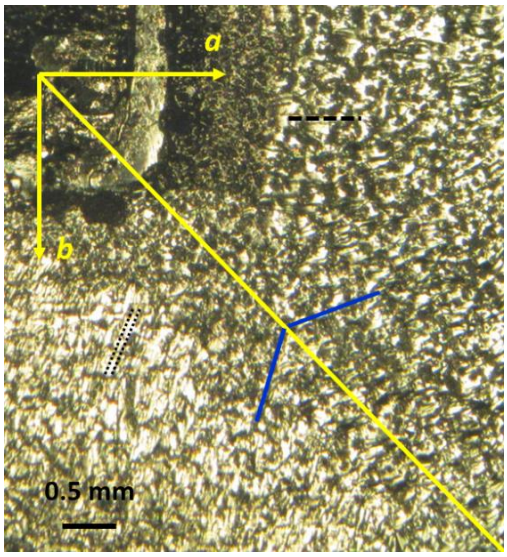

Figure 5-5 Top view of a quarter of $BaTiO_3$-doped sample after annealed in oxygen under optical microscope.

5.4.7 Direct observation of sink-shaped immature grain boundaries in doped sample

For the microscopic characteristics of $BaTiO_3$-doped sample, our first concern is to verify the microscopic ICSs and sinks. In fig. 5-6a, the laminated crystalline layers can be seen clearly. Each layer assembled with the neatly arranged ICSs, sinks are naturally formed between ICSs as seen the dark contrast lines. The region in the rounded rectangle reflects the initial stage of solidification, which is assembled with the small solidified islands and pores. Figure 5-6b shows the marginal GFs of the laminated layers, similar to the crystalline layer in fig. 5-6a, the marginal GFs are assembled with the neatly arranged ICSs too. The needle-like ICSs are also composed of the small solidified islands and pores as seen the lower portion of the GF of plateau1. From lower left corner to upper right

corner, ICSs become wider and wider as denoted with the break arrow, tracing the evolution of the ripening of ICSs. That is, the needle-like ICSs merged into the widened ICSs with the prism surface and formed sinks or roofs, the roofs being the inverse sink equivalently. All these features are similar to that in fig. 5-3, proving that $BaTiO_3$ doping does not destroy the solidification procedure of Gd-Ba-Cu-O superconductor. Therefore, the two-step solidification still acts the key role in $BaTiO_3$-doped sample. Such GF will guide the travelers into orderly ranks and will be described in the next paragraph. In addition, plateau1 is thicker than plateau2, posting the GFs assembled with many crystalline layers. Linear nanoparticle arrays are not found in fig. 5-6a since the two-step solidification was not completed, but they may partially be buried inside the matrix in fig. 5-6b.

5.4.8 Grid-like nanowalls formed by inserting nanoparticles into grain boundaries

The second concern is that whether the marginal GF acts as the tourist guide or not for the travelers into orderly ranks. Excitingly, such case has been observed in the developed GFs. Figure 5-6c shows the linear particle arrays steered by the ‘ordered channels’ and the ‘ordered driving forces’. The lower half corner poses a gradient of crystal layers, and a slope appeared in the rounded rectangle which is the marginal GF of crystalline layers. Interestingly, the accumulated precipitations are dispersed like comet tails from upper to lower of the slope, showing that the white particles are vigorously transported to the sinks or roofs aligned along the a-axis, and thus verified the feasibility of driving heterogeneous particles into orderly ranks. The dispersions also confirmed that the marginal GFs are the power source of the ‘ordered driving forces’. Phenomenologically, the precipitations resemble some kind of colloid or in the semi-melting state in melting process and thus have been elongated like comet tails both on the slope and on the different crystal layers as seen in the inset in fig. 5-6c. Therefore, the feasibility of driving heterogeneous particles into orderly ranks was clarified both on the marginal GF and on the ab-plane. To see the important role of the marginal GF more clearly, a developed marginal GF obtained in another region was shown fig. 5-6d. Linear nanoparticle arrays show a longer propagation and a more homogeneous diameter, indicating that further growth is conducive to the formation of long uniform linear nanoparticle arrays. Inasmuch as the full growth, the sinks have been sealed. Meaning while, in contrast to the slope appeared in fig. 5-6c, the particles are transported here from lower to upper of the slope which can be identified from the moving traces such as the comet tails locate in the lower left corner, while the directions of liquid flow are always toward the a-axis, suggesting that one laminated CS has two marginal GFs, one point to the outside of the single domain, and the other running its inside.

According to the inset in fig. 5-6c, the particles can be transported to the ab-plane, but the particles seem to be just adhered to the surface of the crystalline layers. Then, the third concern is that whether the particles have been buried uniformly inside the low angle GBs. In fact, it has been realized unbelievably as a high probability event in present sample. Figure 5-6e shows the regular arranged linear nanoparticle arrays embedded in the ab-plane. The white looming lines are the low angle GBs filled with the precipitations. In contrast with the linear nanoparticle arrays appeared in the marginal growth front, here the precipitations are seemingly act as little linkers between the adjacent CSs as seen the edges of a CS marked by arrows, and the nano-particle-lines are further extended over 60μm with a uniform diameter ~ 200 nm, proving unambiguously the successful segregation of nano-particls to the low angle GBs, the sandwich structure being achieved.

For this reason, CSs can be broken individually from another as seen the forth region between the arrows. Thanks to the broken CSs, the single crystalline layer can be identified too. Three apparent layers were signed with L1, L2 and L3 respectively. The thickness of the single layer, estimated from the scaling bar, is ~ 500 nm. The nearest parallel particle-lines embedded in the adjacent layers in ab-plane are also aligned along the c-axis as seen the back and the forth of the white arrow, assembling, from the three dimension view, the local **grid-like naowalls** in the ac-plane. Therefore, the 3D GDAs have been created successfully in present $BaTiO_3$-doped Gd-Ba-Cu-O superconductor.

In addition, the linear particle arrays propagate from lower left corner to upper right corner in fig. 5-6e, and CSs were broadened continuously, showing a modification of the evolution of CSs due to the filling effect, which also has been evidenced by the comet-tail-like pattern of the accumulations as shown in fig. 5-6c. This may be the reason why the macroscopic CSs oriented its alignments in changing directions in fig. 5-5. The broadened space of the in-plane particle arrays in fig. 5-6e may arise, on the one hand, from the local insufficient amount of precipitations, on the other hand, from the invisible particle arrays buried inside GBs. The denser and deeper arranged linear nanoparticle arrays were found in fig. 5-6f. The depth of the visible laminated crystal, estimated from the broken edge located in the upper right corner, is ~ 10 μm. One can see that the white dense linear nanoparticle arrays mainly 1 – 3 μm in spaces appeared in each the visible plateau, the adjacent particle arrays locate in the adjacent layers are also aligned along the c-axis as denoted by the two arrows, indicating the high feasibility of engineering the 3D linear nanoparticle arrays in a large scale. The c-axis alignments are originated from the c-axis aligned marginal GF of the laminated CS columns and its guidance role for the travelers. To our knowledge, this result is the first one of engineering the 3D GDAs in textured Gd-Ba-Cu-O bulk superconductor.

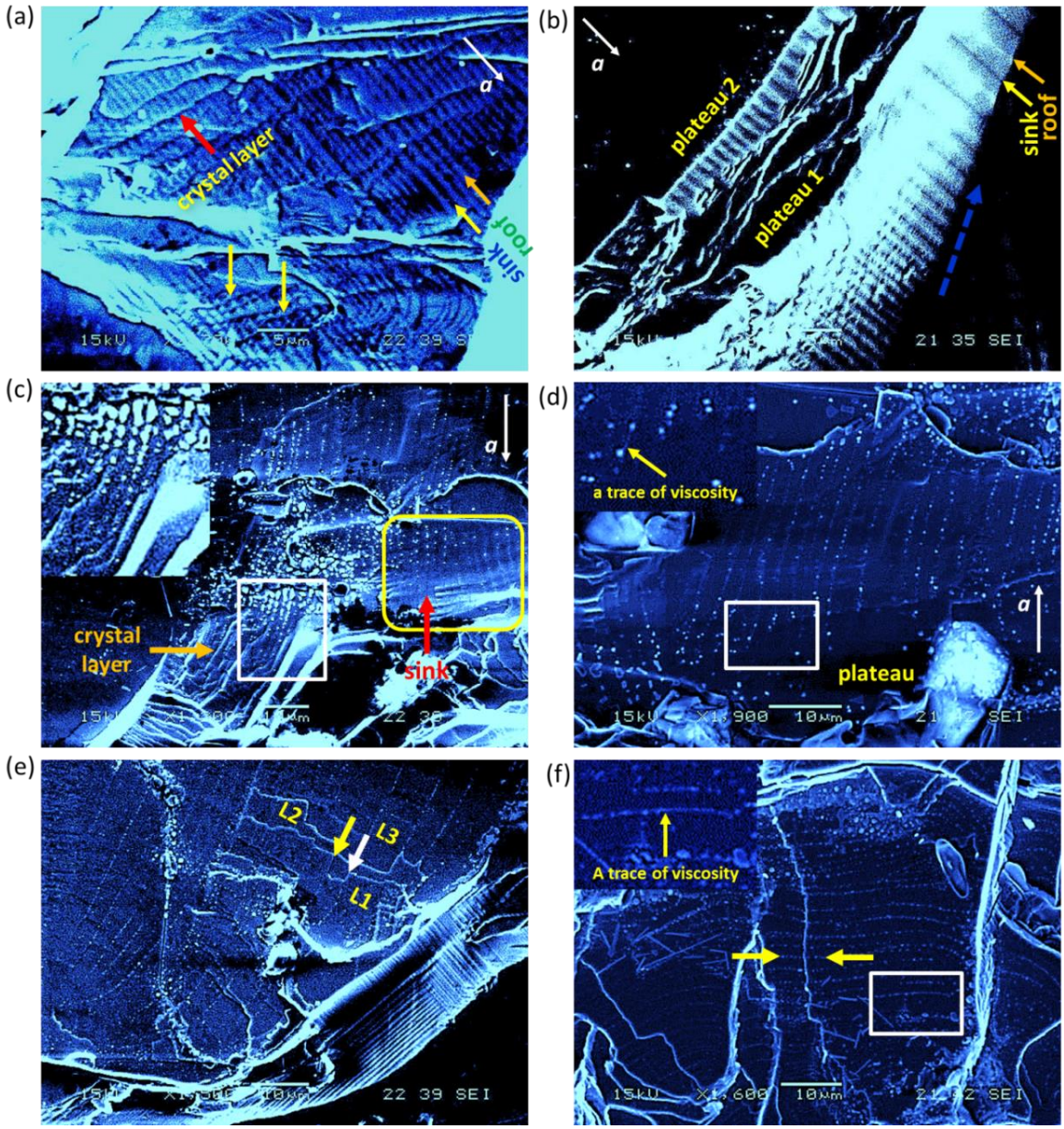

Figure 5-6 Microstructure of $BaTiO_3$-doped sample annealed in oxygen. The c-axis growth direction is perpendicular to the layer toward to the outside of paper for all specimens. **(**a) Characteristic of ICSs and sinks appeared in ab-plane in an insufficient growth region. (b) Characteristic of the sinks, ripening of the microscopic CSs and the orderly super ranks appeared on the marginal growth front of laminated crystal layers. (c) Linear nanoparticle arrays as well as the moving traces of the white particles driven by the 'ordered driving forces' of the directional transported liquid both on growth front and on ab-plane. Inset is the enlargement of the region marked by the rectangle. (d) The linear nanoparticle arrays embedded in a single plane. Inset is the enlargement of the region marked by the rectangle, showing a trace of viscosity of the white particles. (e) Regular arranged linear particle arrays embedded in the laminated crystal. (f) Dense 3D nano-particle arrays embedded in multilayer verified the correctness of driving the heterogeneous particles into orderly ranks in a deep scale along c-axis. Similar to (d) inset confirmed the viscosity of the semi-melting state.

In summary of material processing, the solidifying of the specific laminated marginal GF leads to the directional liquid transportation which is the source of the ‘ordered driving forces’ for particles suspended in liquid. The ‘ordered driving forces’ separates the accumulated precipitations into fine particles and segregates them to the IGBs. After full solidification of ICSs, 3D linear nanoparticle arrays are formed inside the textured Gd-Ba-Cu-O bulk superconductor. The semi-melting $BaTiO_3$ doping related precipitations provide the good dispersibility for compelling them into the order ranks. Further evidences of such sort of precipitation can be found in the insets in fig. 5-6d and 5-6f respectively, the traces of viscosity have been found there. $BaTiO_3$ doping not destroys the growth regime of the host material. $BaTiO_3$ doping related precipitation is expelled by the host matrix. These two features ensured the success engineering of 3D GDAs.

5.5 Vortex pinning and critical current

Such 3D GDAs are obviously conducive to the intensive pinning of the longitudinal aligned defects and the commensurate pinning of the horizontal aligned geometric defect arrays. Figure 5-7 shows the physical properties of the specimen with and without $BaTiO_3$. With the addition $BaTiO_3$, hysteresis loop is broadened as shown in fig. 5-7a, showing the enhanced current penetrability and the improved vortex trapping ability. Especially, contrasting with the decreased behavior of the reference in the range 2 – 5 T, the near linearly increased tendency of the doped one is extended from 1 T to 5 T (see the arrows), reflecting the excellent high-field magnetic property. As mentioned above, $BaTiO_3$ convert into the superconducting phase in YBCO, similar result was found here too, transition temperature decreased and was broadened below - 0.7 as shown in fig. 5-7b since the intercalated precipitations are independent of matrix, indicating the weak superconducting property of the doping related precipitations. Further, a small jump appeared around 76.5 K as indicated with the arrow in fig. 5-7b, hinting the filler transforms from superconducting phases to nonsuperconducting phases. In other word, sandwich structure assembled of three superconducting layers with the grid-like thin one in center has been constructed locally in low temperature, which contributes to the enhanced vortex pinning in low field [41]. With the increasing of external field, the intercalated superconducting phases were forced into non-superconducting ones to trap the new emerged vortex, and thus contribute to the high-field pinning and simultaneously compensate the inadequate in-plane pinning strength of ‘pure GBs’ [41]. Consequently, critical current density J_c, as shown in fig. 5-7c, was improved totally from 0 T to 5 T. The peak value with an up shifted peak position 3.3 T. In contrast to the random defects, present 3D GDAs should collimate vortex lines and regulate vortex lattice, meaning while, may impede the vortex phase transition and delay the pinning relaxation due to the ‘vortex lattice/pinning landscape’ interaction. All these factors give rise to the high-field vortex pinning. Consequently, pinning force density F_p as shown in fig. 5-7d was improved over threefold at 3.8 T.

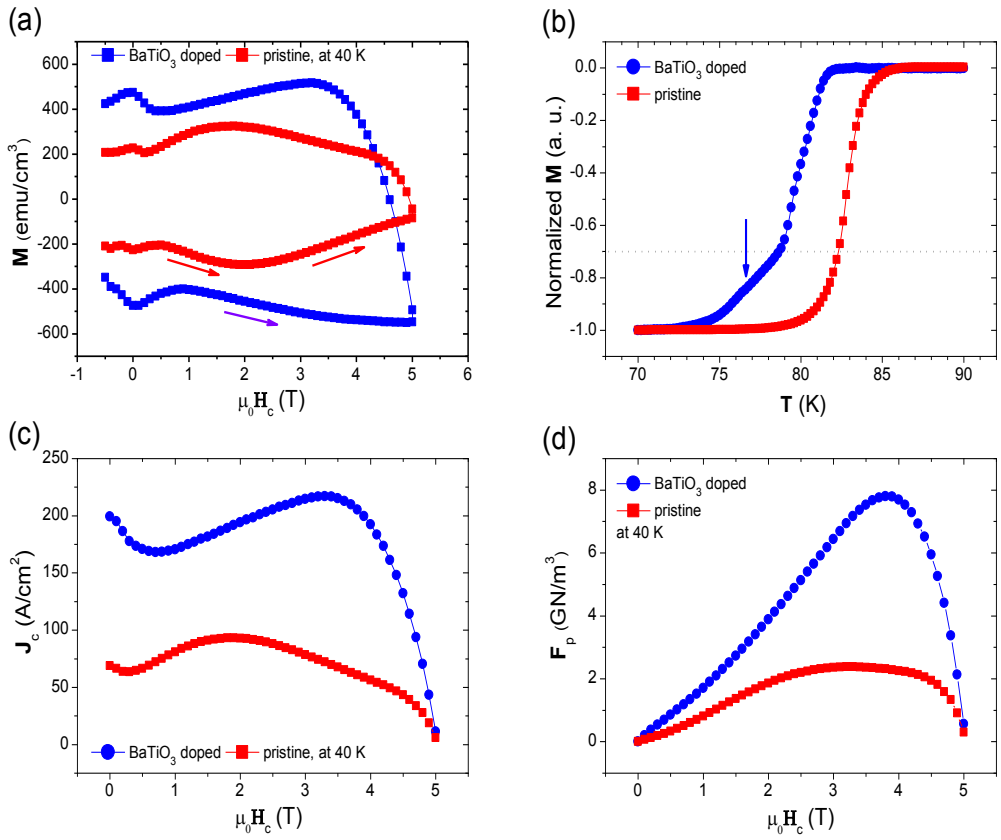

Figure 5-7 The comparison of the corresponding magnetic properties measured from the specimen with and without the addition $BaTiO_3$. (a) Magnetization hysteresis loops measured at 40 K (half of each loop was shown only). (b) Temperature dependence of the normalized magnetization. (c) Field dependence of critical current density deduced from (a). (d) Field dependence of pinning force density deduced from (c) with the formula: $F_p = J_c \times B$.

The peak positioned at 3.3 T reached to 2.2×10^5 A/cm^2, more than twice of the reference 9.3×10^4 A/cm^2 positioned at 1.9 T. F_p shown in fig. 2d increases near linearly with increasing of external field from 0 T to 3.8 T and reached to the maximum value of 7.8×10^9 N/m^3 at 3.8 T, more than three times of the reference 2.4×10^9 N/m^3 positioned at 3.3 T. Vigorous vortex pinning has been achieved in a wide range of magnetic fields because the tunable vortex lattice has been immobilized by the formation of grid-like nanowalls. The huge contribution of the 3D GDAs on the enhancement of vortex pinning or critical current density has been confirmed unambiguously. Therefore, the grid-like nanowalls can be classified as a new vigorous pinning landscape which is better than random defects and effectively contributes to the high-field pinning performance.

5.6 Vortex trapping model

Vortex pinning dynamic induced by the competition between the pinning wall and the external field is summarized in a simple model as shown in fig. 5-8a. Confined by the grid-like nanowalls, vortex lines should also be arranged preferentially into the vortex walls, while the mutual exclusions between the adjacent vortices force themselves further into the uniformly arranged vortex array along GBs, finally forming a unique three-dimensional geometric vortex lattice.

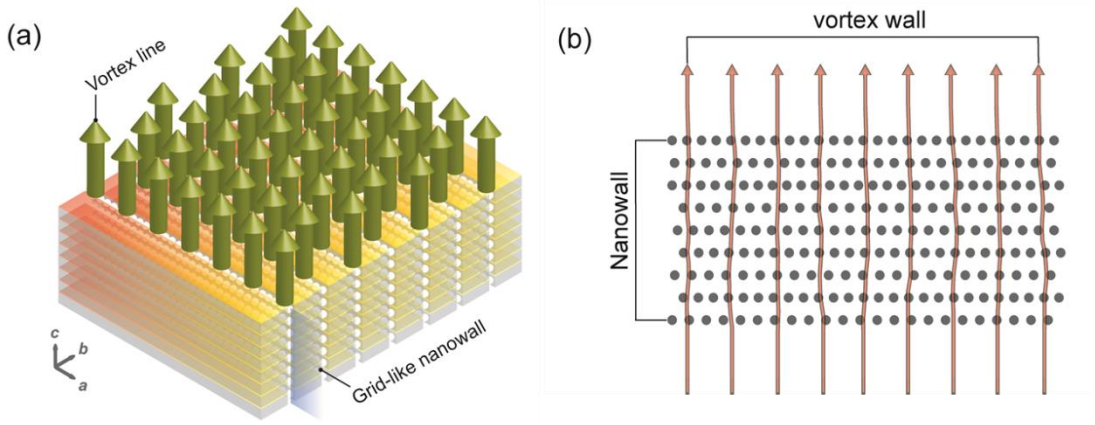

Figure 5-8 (a) Schematic view of the vortex line arrays pinned by the three-dimensional grid-like nanowalls. (b) Schematic view of a vortex wall pinned by a grid-like nanowall.

Increasing external field, new vortices will be trapped into the nanowalls, and new uniform vortex wall could be formed after a relaxation, since the grid-like nanowall consists of the superimposed nanoparticle arrays, projects a solid line in the ab plane, which provides variable spatial periodicities for matching with the tunable vortex lattice as shown in fig. 5-8b. The present arrangement of nanoparticles shows pseudo continuity in the ac plane and periodicity in the ab plane. We name this feature as semicontinuity. It allows us to immobilize tunable vortex lattice by using only one kind of pinning landscape. In addition to the possible uniformly arranged vortex walls, interstitial sites between the adjacent nanowalls are also capable of trapping excess vortices. In this way, the grid-like nanowalls maintain high pinning potentials in a wide range of magnetic fields, thereof showing great potentials on boosting the large scale applications of high-T_c superconductor. Therefore, our findings provide a new practical route for achieving high critical current in high magnetic field.

5.7 Conclusion

We have proposed a practical scenario of how to trap tunable vortex lattice by using only one pinning landscape and at the same time given its experimental demonstration. The 3D grid-like nanowalls have been achieved by exploiting the ‘ordered driving forces’ of the directional transported liquid. By means of the addition of $BaTiO_3$, the doping related precipitations have been inserted elaborately into neatly arranged grain boundaries in textured Gd-Ba-Cu-O bulk superconductor and formed the grid-like nanowalls in the ac plance. Thanks to the grid-like nanowalls, the high-field critical current density J_c and the high-field pinning force density F_p have been enhanced strikingly. The enhanced pinning performance was attributes to the synergetic combination of collective pinning of the longitudinal aligned defects and commensurate pinning of the horizontal aligned geometric defect arrays. Eventually, a scientific model of trapping tunable vortex with one pinning landscape has been proposed. This finding opens a new perspective for achieving the high current-carrying ability especially in high magnetic field and provides a new basis for understanding the ‘vortex lattice/pinning landscape’ puzzle. The present result also proved that the in-field pinning or so-called peak effect is highly related to two factors: weak superconducting phases and their ordered arrangement, confirmed the scenario proposed in chapter 4. The present novel pinning landscape shows a great potential on boosting the large-scale applications of tapes, wires and bulks. In this way, the main obstacle of low current-carrying ability in external magnetic field can be removed.

References

[1] A. P. Malozemoff, *Nat Mater* 6 (2007) 617.

[2] D. Larbalestier, A. Gurevich, D. M. Feldmann, A. Polyanskii, *Nature* 414 (2001) 368.

[3] T. Haugan, P. N. Barnes, R. Wheeler, F. Meisenkothen, M. Sumption, *Nature* 430 (2004) 867.

[4] J. L. MacManus-Driscoll, S. R. Foltyn, Q. X. Jia, H. Wang, A. Serquis, L. Civale, B. Maiorov, M. E. Hawley, M. P. Maley and D. E. Peterson, *Nat Mater* 3 (2004) 439.

[5] P. Yang and C. M. Lieber, *Science* 273 (1996) 1836.

[6] B. Maiorov, S. A. Baily, H. Zhou, O. Ugurlu, J. A. Kennison, P. C. Dowden, T. G. Holesinger, S. R. Foltyn and L. Civale, *Nat Mater* 8 (2009) 398.

[7] P. Mele, K. Matsumoto, T. Horide, A. Ichinose, M. Mukaida, Y. Yoshida, S. Horii and R. Kita, *Supercond Sci Tech* 21 (2008) 032002

[8] A. V. Silhanek, A. Leo, G. Grimaldi, G. R. Berdiyorov, M. V. Milošević, A. Nigro, S. Pace, N. Verellen, W. Gillijns, V. Metlushko, B. Ilić, X. Zhu and V. V. Moshchalkov, *New J Phys* 14 (2012) 053006.

[9] A. A. Abrikosov, *Soviet Physics JETP* 32 (1957) 1142.

[10] G. Blatter, M. V. Feigel'man, V. B. Geshkenbein, A. I. Larkin and V. M. Vinokur, *Rev Mod Phys* 66 (1994) 1125.

[11] M. Muralidhar, N. Sakai, N. Chikumoto, M. Jirsa, T. Machi, M. Nishiyama, Y. Wu and M. Murakami, *Phys Rev Lett* 89 (2002) 237001.

[12] A. I. Larkin and Y. N. Ovchinnikov *J Low Temp Phys* 34 (1979) 409.

[13] C. Reichhardt, C. J. Olson and F. Nori, *Phys Rev B* 57 (1998) 7937.

[14] K. Harada, O. Kamimura, H. Kasai, T. Matsuda, A. Tonomura and V. V. Moshchalkov, *Science* 274 (1996) 1167.

[15] R. Weinstein, D. Parks, R. P. Sawh and K. Davey, *Supercond Sci Tech* 23 (2010) 115015.

[16] N. H. Babu, Y. H. Shi, K. Iida and D. A. Cardwell, *Nat Mater* 4 (2005) 476.

[17] W. K. Yeoh, S. K. Pathak, Y. H. Shi, A. R. Dennis, D. A. Cardwell, N. H. Babu, K. Iida and M. Strasik, *Supercond Sci Tech* 22 (2009) 065011.

[18] M. Tomita and M. Murakami, *Nature* 421 (2003) 517.

[19] S. Nariki, N. Sakai and M. Murakami, *Supercond Sci Tech* 18 (2005) S126.

[20] B. Li, D. Zhou, K. Xu, S. Hara, K. Tsuzuki, M. Miki, B. Felder, Z. Deng and M. Izumi, *Physica C* 482 (2012) 50.

[21] N. H. Babu, Y. H. Shi, S. K. Pathak, A. R. Dennis and D. A. Cardwell, *Physica C* 471 (2011) 169.

[22] M. Chudy, M. Eisterer, H. W. Weber, J. Veterníková, S. Sojak and V. Slugeň, *Supercond. Sci. and Tech.* 25 (2012) 075017.

[23] R. Boistelle and J. P. Astier, *J Cryst Growth* 90 (1988) 14.

[24] R. Cloots, T. Koutzarova, J. P. Mathieu and M. Ausloos, *Supercond Sci Tech* 18 (2005) R9.

[25] Y. Xu, K. Tsuzuki, S. Hara, Y. Zhang, Y. Kimura and M. Izumi, *Physica C* 470 (2010) 1219.

[26] B. Li, K. Xu, S. Hara, D. Zhou, Y. Zhang and M. Izumi, *Physica C* 475 (2012) 51.

[27] C. X. Xu, A. M. Hu, N. Sakai, M. Izumi and H. Hirabayashi, *Supercond. Sci. Tech.* 18 (2005) 1082.

[28] X. Yao and Y. Shiohara, *Supercond. Sci. Tech.* 10 (1997) 249.

[29] R. Liang, P. Dosanjh, D. A. Bonn, D. J. Baar, J. F. Carolan and W. N. Hardy, *Physica C* 195 (1992) 51.

[30] X. Yao and H. Hu, *Prog Solid State Ch* 32 (2004) 219.

[31] X. Yao and Y. Shiohara, *Mat Sci Eng B-Solid* 53 (1998) 11.

[32] M. Muralidhar, N. Sakai, M. Jirsa, N. Koshizuka and M. Murakami, *Appl Phys Lett* 85 (2004) 3504.

[33] M. Muralidhar, N. Sakai, M. Jirsa, N. Koshizuka and M. Murakami, *Appl Phys Lett* 83 (2003) 5005.

[34] M. Muralidhar, N. Sakai, M. Nishiyama, M. Jirsa, T. Machi and M. Murakami, *Appl Phys Lett* 82 (2003) 943.

[35] Y. Shi, N. H. Babu, K. Iida, W. K. Yeoh, A. R. Dennis and D. A. Cardwell, *Supercond Sci Tech* 22 (2009) 075025.

[36] D. Dimos, P. Chaudhari, J. Mannhart and F. K. LeGoues, *Phys Rev Lett* 61 (1988) 219.

[37] S. E. Babcock, X. Y. Cai, D. L. Kaiser and D. C. Larbalestier, *Nature* 347 (1990) 167.

[38] M. J. Cima, M. C. Flemings, A. M. Figueredo, M. Nakade, H. Ishii, H. D. Brody and J. S. Haggerty, *J Appl Phys* 72 (1992) 179.

[39] H. W. Zandbergen, *Physica C* 194 (1992) 287.

[40] K. Chan Joong, K. Ki Baik, L. Kyu Won, L. Chong Tak, H. Gye Won, C. In Soon and W. Dong Yeon, *Mater Lett* 11 (1991) 241.

[41] G. S. Mkrtchian and V. V. Shmidt, *Zhurnal Eksperimental noi i Teoreticheskoi Fiziki* 68 (1975) 186.

Chapter 6 Study of the Hybrid Magnet Assembled with Bulks and Tapes

6.1 Introduction

Improving trapped magnetic flux in type-II superconductors involves many kinds of technologies. We have done fundamental explorations from the view point of material science. Enlightening significance of control of vortex lattice in magnetic field has been described in chapter 5. Alternatively, optimization of the trapped flux performance involves assembling technique based on the developed RE-Ba-Cu-O bulk superconductor. For instance by changing the angles between two bulk slices as described in following text, the jagged trapped flux profile of a superconductor caused generally by grain boundaries or cracks is smoothed. In particular, the total trapped flux is improved too. To achieve high trapped magnetic flux, it is also interesting to assemble bulks and tapes into hybrid superconducting magnet. By means of such study, important factors of making hybrid magnet can be clarified. In this chapter, we focus on the issues of how to use the developed bulks and tapes efficiently in practical devices.

6.2 Some relevant considerations

We have applied a high-temperature superconductor (HTS) Gd-123 bulk (60 mm diameter, 19 mm thickness) as a pole-field magnet in synchronous rotating machinery [1]. The bulk magnets are used equivalently as the conventional permanent magnet in motor. The key issue is how to introduce the intensified flux into the rotor. General techniques enhancing the total trapped magnetic flux are cooling the superconductor down to lower temperatures [2], making lager HTS bulk [3] and optimizing the magnetizing process [4]. However when experiencing a pulsed field, bulks suffer from thermal instability below 77 K resulting from inhomogeneous critical current density and leading to hotspots during magnetization. For lower applied pulsed field, magnetic flux was penetrated and trapped in the growth sector region, and for higher applied pulsed field, the magnetic flux was trapped more preferentially in the growth sector boundary, when assuming a higher J_c is in the growth sector boundary of a bulk [5].

A stack of coated conductors has relatively uniform J_c both radially and axially and so does not suffer from this thermal instability upon pulsed magnetization. The superior mechanical strength of a stack of tapes due to the high tensile strength of the metal alloy substrates (typically Hastelloy R or Ni-W) should also allow higher limits for trapped fields. This would be advantageous for replacing bulks which are used to trap very high fields [6] and also in machines which experience high rotational stress such as magnetic bearing designs using magnetized rotor bulks [7]. Finally the growth of thin films to form superconducting tapes is not as limited in size as bulks given that a buffered metal substrate provides the texture for the (RE)BCO rather than a localized seed crystal. This is particularly true for tapes in which the texture is introduced by thermo-mechanical

processing of the metal substrate (e.g. rolling assisted biaxially textured substrates, RABiTS R), and where non-vacuum deposition techniques are used, e.g. chemical solution deposition (CSD) and ink-jet printing [8].

Large (RE)BCO bulks can be manufactured with high quality [3] but it is a challenge to maintain high J_c far away from the seed crystal which lies at the center compared to wide (RE)BCO tapes with uniform J_c [9]. Field cooling of square annuli cut from large 40 mm wide tape manufactured by American Superconductor has been performed in liquid nitrogen [10]. Using field cooling at 77 K, trapped fields of up to 1.4 T have been achieved for a 24 mm diameter GdBCO bulk [11], and 3 T for a larger 65 mm bulk [12]. The highest trapped field using pulsed magnetization below 77 K is currently 5.2 T in a large 45 mm bulk [13]. The best critical current performance values (per tape width) for existing (RE)BCO tapes include 600 Acm^{-1} for long 600 m lengths (Fujikura) [14] and greater than 1000 Acm^{-1} for shorter samples (THEVA) [15], at 77 K and in self-field. A comparison between standard commercial (RE)BCO tape and a standard commercial bulk of similar diameter to the tape width supports the broader concept of composite superconducting bulks which do not necessarily need to be composed of (RE)BCO tape to have superior trapped field performance than existing bulks [16]. Modeling has predicted that structures composed of bulk (RE)BCO and metallic components can also achieve enhanced trapped fields due to higher thermal stability [17].

Enhancing the thermal stability of bulk superconductor and improving the total trapped flux, we propose a practical strategy that cutting bulks into thin slices and stacking these slices by changing their orientations and further attaching tapes to each slice, i.e. assembling a hybrid magnet. In this way, thermal conductance can be improved by means of the metallic components of the tapes, whereas trapped field is benefit from the advantages of both bulks and tapes simultaneously.

6.3 Experimental details

6.3.1 Material

Experiments were carried out by using the Gd-123 bulk slices provided by Nippon Steel & Sumitomo Metal. The parameters are listed in table 6-1. Gd-123 tapes are made by Fujikura, the relevant parameters are listed in table 6-2.

Table 6-1 Parameters of the disc-shaped Gd-123 bulk superconductors

Sample No.	B_t (T) at 77 K	Material	Shape
Gd5439-1	0.65	Gd-Ba-Cu-O	Disc-shaped Φ 60 mm × 3 mmt
Gd5439-2	0.70		
Gd5439-3	0.60		
Gd5436-3	0.55		
Gd5524-3	0.55		
Gd5437	1.55		Φ 60 mm × 19 mmt

Table 6-2 Parameters of the Gd-123 tape superconductor

Material of each layer	Thickness	length	width	Critical current
Cu (oxygen-free)	100 μm	5 m	10 mm	> 500 A Measured value 600 A (77 K, self-field, 1 μV/cm)
Sn	2-4 μm			
Ag	8.0 μm			
$GdBa_2Cu_3O_x$	1.8 μm			
CeO_2	0.4 μm			
MgO	5 nm			
Y_2O_3	30 nm			
Al_2O_3	100 nm			
Ni based alloy	100 μm			

6.3.2 Trapped field measurement method

By using field cooling method, we first measured the trapped fields of Gd5439-1 and Gd5439-2 and further measured the trapped fields by changing the angles of growth sector boundaries between the adjacent disc-shaped superconductors. One arrangement is set to be 0 °and the other is 45 °. The cooling field is 2 T. The measured gap between top surface and Hall sensor is 0.5 mm. The detailed measurement process can be described briefly as follows. The disc-shaped superconductor was attached to the bottom surface of an insulation square groove, then put the groove into a 5 T superconducting magnet to undergoes a field cooling process by introducing slowly the liquid nitrogen. The sample was buried in liquid nitrogen approximately in 10 minutes, and then filled the groove. The filled groove was remained for 30 minutes in magnetic field, then the field was reduced to zero. Waiting for 15 minutes, we started to measure the trapped field with a Hall sensor controlled automatically by a computer as shown in fig. 6-1.

Figure 6-1 Schematic view of trapped field measurement in our laboratory.

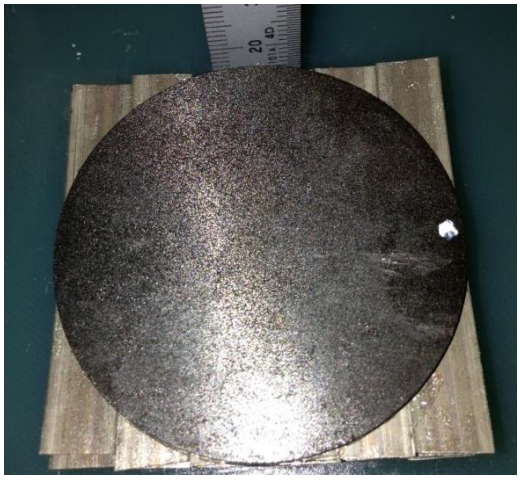

Figure 6-2 Image of the hybrid magnet consists of five disc-shaped bulks and four layers of the single-layer tapes arranged parallel to each other.

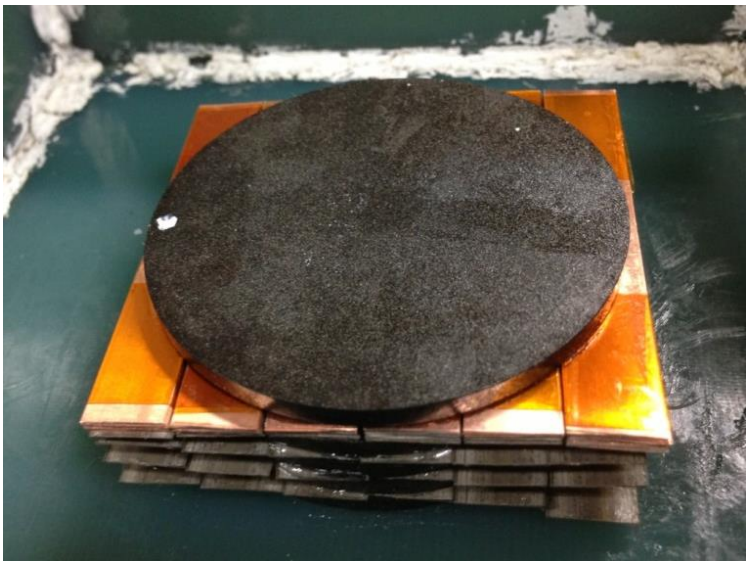

Figure 6-3 Image of the hybrid magnet consists of one multilayer tapes.

6.3.3 Assembling of hybrid magnet

Assembling the hybrid magnet, the superconducting tape was cut into small fragments using a scissor. The length of each fragment is 60 mm. One layer of the tapes consists of six fragments with total width of 60 mm. Those disc-shaped bulks and tapes are assembled alternatively into hybrid magnet as shown in fig. 6-2. To optimize the trapped field profile, the angles between the adjacent bulks are rotated 45 ° successively. In addition, hybrid magnet consists of multilayers of tapes was also made as shown in fig. 6-3.

6.3.4 Assembling of stacked coated conductors

To learn the possible trapped flux performance of the stacked coated conductors, the fragments 60 mm in length were cut further into smaller fragments 20 mm and 10 mm in length. Three magnets consist of 60 layer tapes has a size of 60 mm × 10 mm × 14 mm, 20 mm × 10 mm × 14 mm and 10 mm × 10 mm × 14 mm respectively. The stacked tapes were reinforced by using Teflon tapes as shown in fig. 6-4. Similar to the bulk superconductors, the stacked coated conductors has ability of trapping magnetic flux too and show potentials for replacing the bulk superconductors in future due to its high pinning performance.

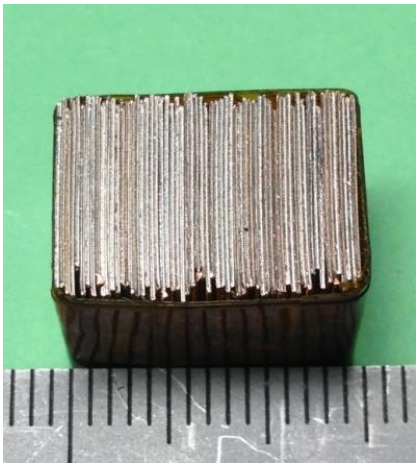

Figure 6-4 Image of the stacked coated conductors with a size of 10 mm × 10 mm × 14 mm. It has ability of trapping magnetic flux similar to the bulk superconductors.

6.4 Results and discussions

6.4.1 Superimposed effect of the stacked bulk superconductors

Figure 6-5 shows the trapped flux profile measured from the sample Gd5439-1. Consistent with table 6-1, the maximum value of the trapped flux density is 0.65 T. Four growth sections can be identified from the square-like contour lines closed to the center. However, the square-like contour lines far away from the center exhibit jags due to the cracks appeared in the superconducting matrix during the melting growth. Those cracks given a negative contribution to current flow and thus lead to the deterioration of the total pinning performance.

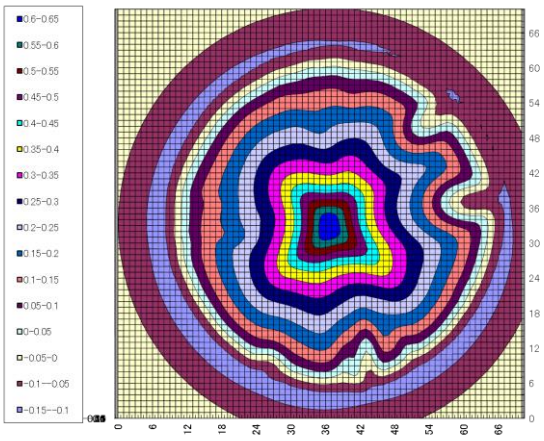

Figure 6-5 The two-dimensional trapped flux profile measured from the sample Gd5439-1.

Figure 6-6 shows the two-dimensional trapped flux profile measured from the stacked samples of Gd5439-1 and Gd5439-2 without misorientation. The maximum value of the trapped flux density is 1.05 T. One can see that the large jags are reduced by such a stacking process. Rotating the samples to an angle of 45 °, the jags are reduced slightly further. The curved contour lines located between the two parallel black lines in fig. 6-6 are turned into straight line as shown that in fig. 6-7. In addition, the maximum value of the trapped flux density is 1.06 T for rotating with an angle 45 °. The longitudinal trapped flux profiles were extracted from these two figures and shown in fig. 6-8.

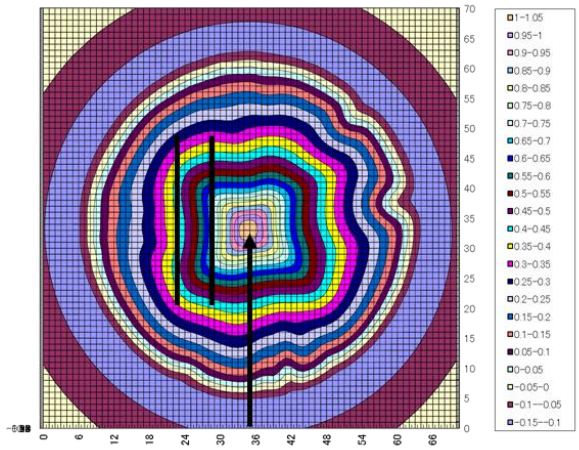

Figure 6-6 The two-dimensional trapped flux profile measured from the stacked samples of Gd5439-1 and Gd5439-2. Gd5439-2 was put under Gd5439-1 with a rotate angle 0 °.

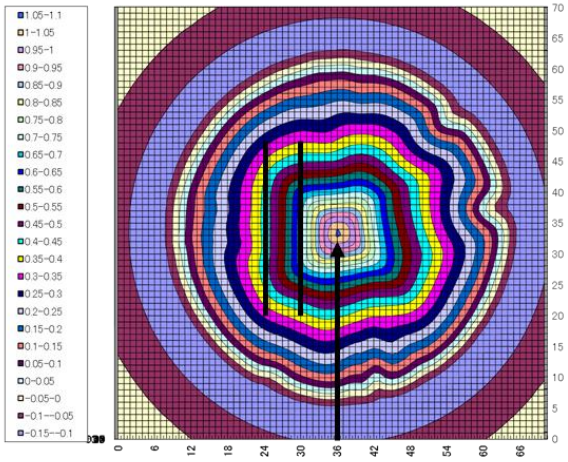

Figure 6-7 The two-dimensional trapped flux profile measured from the stacked samples of Gd5439-1 and Gd5439-2. Gd5439-2 was put under Gd5439-1 with a rotating angle 45 °.

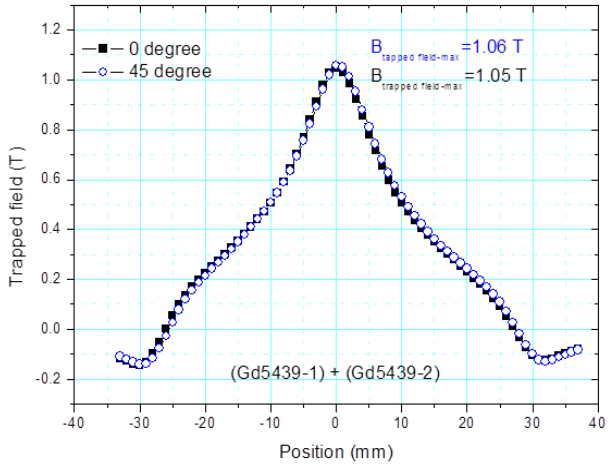

Figure 6-8 The longitudinal trapped flux profiles extracted from fig. 6-6 and fig. 6-7 as indicated with the upward black arrows in fig. 6-6 and 6-7.

6.4.2 Superimposed effect of the stacked bulks and tapes

To study the superimposed effect of the stacked bulks and tapes, we measured the trapped field of three hybrid magnet as shown in fig. 6-9. The three configurations are shown in the insets in fig. 6-10. In contrast to fig. 6-6 and fig. 6-7, the square-like contour lines are modified into circular ones as seen in fig. 6-9a, indicating a positive superimposed effect that is beneficial for practical applications. The possible reasons come from on the one hand the compensation of the spatial distribution of magnetic flux provided by each superconducting slice and on the other hand the magnetic coupling between the adjacent slices due to their inhomogeneous current-carrying abilities in growth sectors and in growth sector boundaries. Of cause, pinning properties are modified too since the small regions of each slice are affected unavoidably by the magnetic fields provided by other slices.

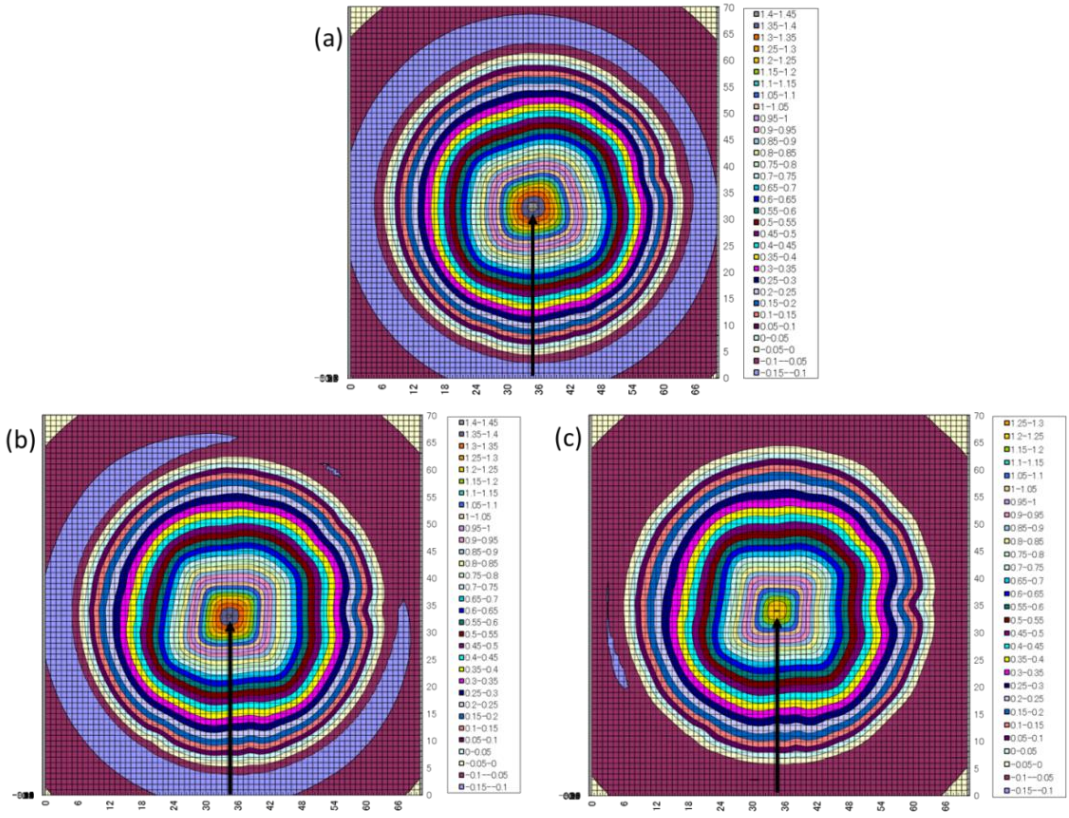

Figure 6-9 The two-dimensional trapped flux profile measured from (a) five stacked bulks; (b) five stacked bulks isolated with single layer tapes; (c) five stacked bulks isolated with multilayer as well as single layer tapes. The configurations were shown in the inset in fig. 6-10.

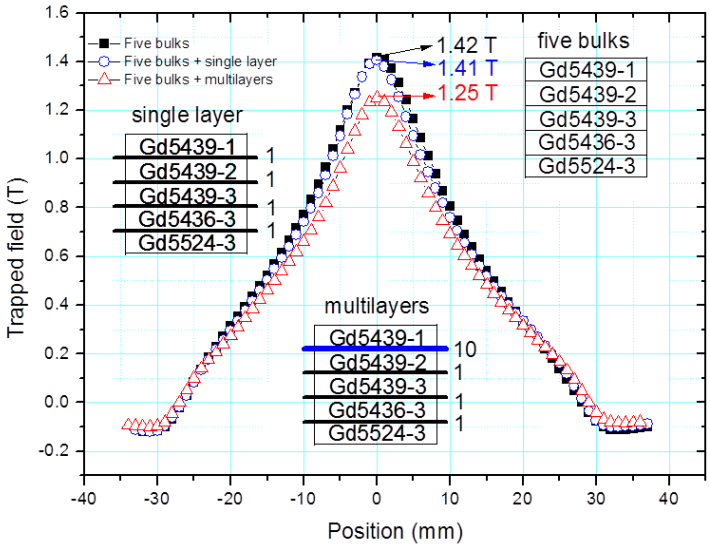

Figure 6-10 Longitudinal trapped flux profiles extracted from fig. 6-9 as indicated with the upward black arrows in fig. 6-9. Insets show the configurations of the stacked bulks and tapes. The upper right inset is the stacked bulks; the left inset is the alternatively stacked bulks and single layer tapes; the lower one is a hybrid magnet with ten layers of tapes attached to the top bulk slice.

The jags of the periphery contour lines become larger when inserting more tapes into the bulks as seen from fig. 6-9a to 6-9c, indicating that the coated superconductors provided weak volume pinning performance compared to the bulks. For this reason, the maximum value of trapped flux density becomes smaller when inserting more layers of tapes as seen the reduced peak in fig. 6-10. The peak value of 1.42 T trapped in the stacked five bulks has changed to 1.41 T and 1.25 T in the hybrid magnet with single layer tapes and multilayers tapes. One can see from table 6-2, the total thickness of the tape is 212.335 ~ 214.335 μm, while the superconducting thickness is 1.8 μm which is 0.85 % of the total thickness. Therefore, although the superconducting layer has high critical current density, this high performance has been balanced out by the large total thickness of the nonsuperconducting layers. In contrast to the slices, the coated conductor shows weak trapped flux performance and thus leads to the decreased peak values in fig. 6-10.

6.4.3 Bulk magnet assembled with stacked tapes

Examining the trapped flux performance of the tapes, we performed the mapping of trapped flux upon bulk magnet assembled with stacked tapes. Bulk magnets stacked with 60 layers of tape 60 mm, 20 mm and 10 in length are shown in fig. 6-11 and fig. 6-4 respectively. The three-dimensional trapped flux measured from these bulk magnets are shown in fig. 6-12, fig. 6-13 and fig. 6-14. The cooling field is 1 T. Measured gap is 0.5 mm. The maximum value of the trapped flux density is 0.17 T which is approximately

equal to each other for the bulk magnet with the length of 60 mm and 20 mm, indicating the homogeneity of the current-carrying ability of the tapes.

The size of current loop in each layer of tape approximately equals to 10 mm × 60 mm and 10 mm × 20 mm respectively in these two magnets. However, further reduce the length to 10 mm, the maximum value of the trapped flux density is reduced to 0.11 T. The reason is that the cutting process given a deterioration of the well textured superconducting layer which leads to small current loops less than 10 mm × 10 mm circled in each layer of tape.

One can imagine that the maximum value of the trapped flux density should equal to 0.17 T too if periphery of the superconducting layers are not destroyed. This value is almost the same with that in normal textured bulk Gd-123 superconductors given a size of 10 mm × 10 mm × 10 mm. One also can imagine that the maximum value of the trapped flux density should excess 0.5 T easily if the volume ratio of the superconducting layer could be improved. Therefore, replacing textured bulks with stacked tapes, the tapes should be made with the relative high superconducting volume without deterioration of pinning property. It is reasonable to assume that the protective layers covered above the superconducting layer could be eliminated if one proposed to make stacked magnet with tapes exclusively. The thickness of the substrate could be reduced too. Because the stacking process given a natural protection to the superconducting layer.

Last the trapped flux of the single-layer tape was measured as shown in fig. 6-15. Error values are partially coming from the measured gaps. The maximum value of the trapped flux density is ~ 30 mT for the measured gap of 0.4 mm and ~ 20 mT for the measured gap of 0.5 mm. The two-dimensional trapped flux was shown in fig. 6-16, by which one can see the effect of cutting process on the deterioration of superconducting layer from the distorted upper or bottom contour lines of two dimensional trapped flux profiles.

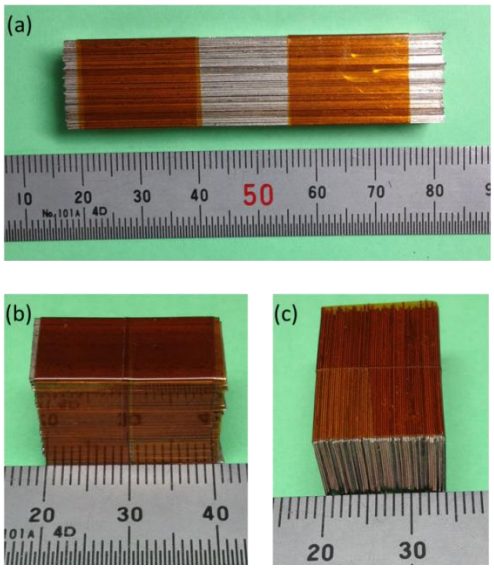

Figure 6-11 Bulk magnet assembled with 60 layers of tape (a) 60 mm in length; (b) and (c) 20 mm in length.

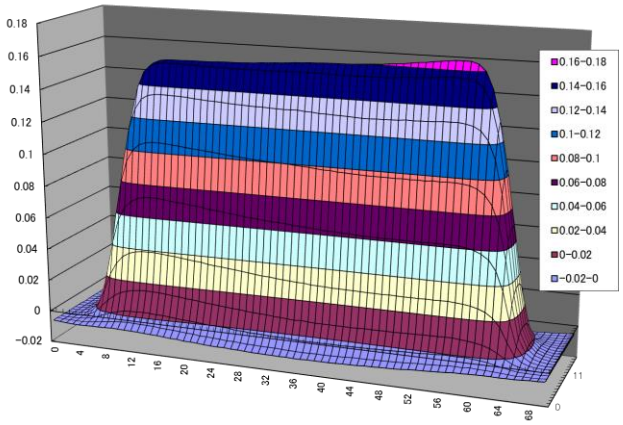

Figure 6-12 The three-dimensional trapped flux measured from the bulk magnet assembled with 60 tapes 60 mm in length.

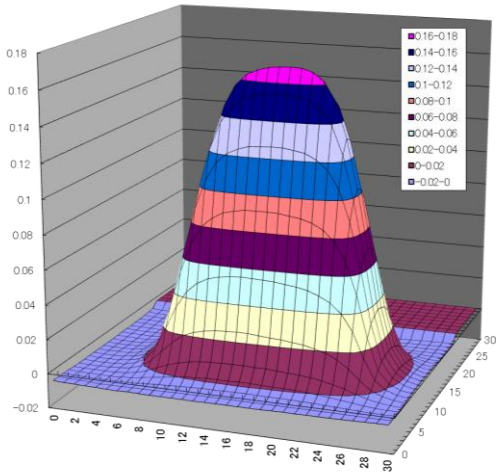

Figure 6-13 The three-dimensional trapped flux measured from the bulk magnet assembled with 60 tapes 20 mm in length.

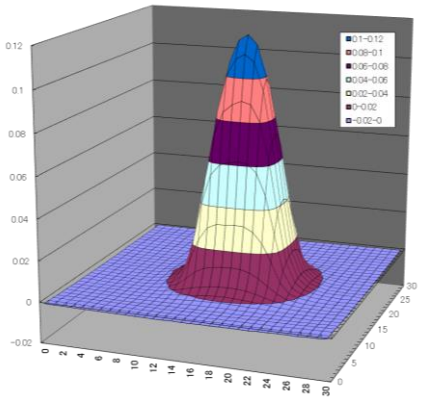

Figure 6-14 The three-dimensional trapped flux measured from the bulk magnet assembled with 60 tapes 10 mm in length.

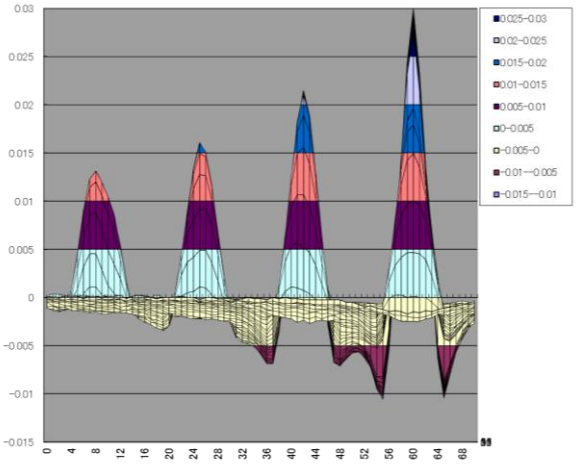

Figure 6-15 The trapped flux profiles measured from four single-layer tapes. The length of the tape arranged from left to right is 10 mm, 20 mm, 40 mm and 60 mm respectively. Error value is ~ 0.005 T.

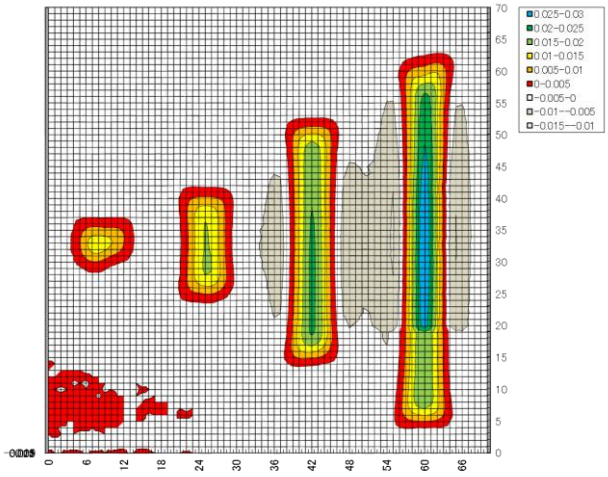

Figure 6-16 The two-dimensional trapped flux profiles measured from four single-layer tapes. The length of the tape arranged from left to right is 10 mm, 20 mm, 40 mm and 60 mm respectively. Error value is ~ 0.005 T.

6.5 Conclusion

Superimposed effect of the stacked bulk superconductors and/or the stacked coated superconductors has been studied. Trapped flux performance is optimized by rotating the stacked bulks to an angle 45 °. Trapped flux performance and the contour lines become better and better with increasing of number of the stacked bulks. However, the performance is reduced when introducing coated conductors into the bulks. The reason is that the superconducting layer occupies only a very small volume ratio in the tape. The high critical current density has been balanced out by the small volume ratio of superconducting layer. Presumably, bulk magnet assembled with the stacked coated conductors could replace the textured bulk superconductors if the high superconducting volume ratio could be achieved without deterioration of the current-carrying performance. By the same consideration, trapped flux performance of the hybrid magnets could be improved too. By means of the alternatively arranged bulks and tapes, disadvantages of the weak thermal conductance of the melt-textured bulk superconductor could be eliminated when undergoes a pulsed magnetization process. Therefore, we have proposed and clarified the relevant key parameters for achieving high trapped flux performance by combining both textured bulk and coated superconductors, which shows possible potentials for promotion of large-scale applications of the type-II superconductor.

References

[1] Miki M, Tokura S, Hayakawa H, Inami H, Kitano M, Matsuzaki H, Kimura Y, Ohtani I, Morita E, Ogata H, Izumi M, Sugimoto H and Ida T, *Superconductor Sci. Technol.* 19 (2006) S494.

[2] B. Felder, M. Miki, Z. Deng, K. Tsuzuki, N. Shinohara, M. Izumi and H. Hayakawa, *IEEE Trans. Appl. Supercond.* 21 (2011) 2213.

[3] Sakai N, Nariki S, Nagashima K, Miryala M, Murakami M and Hirabayashi I, *Physica C* 460-462 (2007) 305.

[4] Ida T, Matsuzaki H, Akita Y, Izumi M, Sugimoto H, Hondou Y, Kimura Y, Sakai N, Nariki S, Hirabayashi I, Miki M, Murakami M, Kitano M , *Physica C* 412-414 (2004) 638.

[5] H. Fujishiro, T. Naito, M. Oyama, *Physics Procedia* 36 (2012) 687.

[6] M. Tomita and M. Murakami, *Nature* 421 (2003) 517.

[7] A Patel, R Palka and B A Glowacki, *Supercond. Sci. Technol.* 24 (2011) 015009.

[8] I Van Driessche, J Feys1, S C Hopkins, P Lommens, X Granados, B A Glowacki, S Ricart, B Holzapfel, M Vilardell, A Kirchner and M B ̈acker, *Supercond. Sci. Technol.* 25 (2012) 065017.

[9] S Hahn, S B Kim, M C Ahn, J Voccio, J Bascunan and Y Iwasa, *IEEE Trans. Appl.Supercond.* 20 (2010) 1037.

[10] S Hahn, J Voccio, S Bermond, D K Park, J Bascunan, S B Kim, T Masaru and Y Iwasa *IEEE Trans. Appl. Supercond.* 21 (2011) 1632.

[11] S Nariki, N Sakai and M Murakami, *Physica C* 378 (2002) 631.

[12] S Nariki, N Sakai and M Murakami, *Supercond. Sci. Technol.* 18 (2005) S126.

[13] H Fujishiro, T Tateiwa, A Fujiwara, T Oka and H Hayashi, *Physica C* 445 (2006) 334.

[14] K. Kakimoto, M. Igarashi, S. Hanyu, Y. Sutoh, T. Takemoto, T. Hayashida, Y. Hanada, N. Nakamura, R. Kikutake, H. Kutami, Y. Iijima, T. Saitoh, *Physica C* 471 (2011) 929.

[15] M D ̈urrschnabel, Z Aabdin, M Bauer, R Semerad, W Prusseit and O Eibl, *Supercond. Sci. Technol.* 25 (2012) 105007.

[16] A Patel, S C Hopkins and B A Glowacki, *Supercond. Sci. Technol.* 26 (2013) 032001.

[17] A Patel and B A Glowacki *Supercond. Sci. Technol.* 25 (2012) 125015.

Chapter 7 Summary and Future Perspectives

7.1 Summary

Immobilizing magnetic vortices in type-II superconductor—a problem that has plagued scientists trying to engineer real-world applications for decades has been solved partially from the view point of comprehensive consideration. The fundamental technique is to make dense and tiny artificial defects in the superconducting matrix, by which negative n-s interfacial energy provides potential well for trapping vortex. However, such fundamental consideration was focused so far one pinning center only. Vortex matter exhibits actually rasterized behavior in intermediate magnetic field, nevertheless, this invisible matter has its own behaviors independent of exact superconductor materials. Therefore, researchers have to consider first the fundamental law of vortex matter as well as the basic properties of different kinds of real materials, and then perform exact strategies to meet the requirement of the practical applications.

Our target is to develop high efficient motors and generators by employing the type-II bulk superconductors in which the high critical current density and high pinning property are necessary. To date, high critical current density is mainly achieved in zero magnetic fields in previous studies. This high performance is suppressed exponentially with increasing of external magnetic field. It is desirable to maintain this high performance in high magnetic field since the type-II superconductor work in magnetic field in Maglev, motors and generators, etc. Some results show high pinning performance in low temperature and high magnetic field, but the fundamental reasons behind this phenomenon remain in mystery. No available clear scenario could be followed. The prototype applications of type-II superconductor are thus carried out mostly in laboratory. To promote the large-scale applications, my target in the past three years is to learn and explore the fundamental relationships between material and vortex matter, critical current density and pinning property as well as pinning behavior and arrangement of defects. We have obtained significant findings toward future practical superconducting devices.

As a novice, I performed basic studies in the first year of my Ph.D program, focused on the doping effect of variety of additions, and particularly performed the experiment of chemical doping with the dilute addition of $BaTiO_3$. The two optimal doping levels of 0.1 mol.% and 0.3 mol.% highly attracted my attention. By means of this experiment, the fundamental relationships mentioned above were discussed. We found the composition of the doping related precipitations change with changing of growth conditions as well as doping levels. A novel reaction mechanism relevant to ions exchange was proposed, which equivalent to partial ions substitution.

Following this finding, TiO_2 doping effect was performed for clarifying the relationship between peak effect and characteristic of doping related precipitations.

Enhanced superconducting property was found and attributed to ion substitution in Cu-O chain. Peak effect was suppressed slightly, but it was broaden prominently in magnetic field. In contrast to $BaTiO_3$ doping, the impact of the element of Ba was eliminated in TiO_2-doped sample. Higher B_{irr} was attributed to the microscopic high-T_c superconducting regions. These two experiments made us to believe that clustered superconducting regions serve the peak effect or in-field pinning.

From the comparative study with the additions of $BaTiO_3$, BaO_2 and TiO_2, two scenarios were proposed: recrystallization mechanism of the doping related precipitations was proposed for achieving nano-sized inclusions; geometric arrangement of the doping related precipitations will be formed due to the anisotropic crystallization. The superconducting regions buried in the matrix, the recrystallization mechanism as well as the geometric arrangement of the doping related precipitations made us to believe that vortex pinning can be controlled by steering pinning centers into geometric patterns.

Keep this point in mind, we pursued the detailed growth mechanism of Gd-Ba-Cu-O bulk superconductor and found that the superconducting matrix grows in the manner of sub-grain arrays and involves a complementary growth process which can be summarized as a two-steps solidifications procedure. By means of this finding, inserting nanoparticles into grain boundaries was proposed and we obtained for the first time geometric defect arrays by doping with the addition of $BaTiO_3$. The doping related precipitations show weak superconducting property, and are arranged into grid-like nanowalls in the ac plane. Those grid-like nanowalls near parallel to each other and arranged periodically in the ab plane. Such layout serves uniform critical current density in a wide range of magnetic fields, confirmed the hypothesis mentioned above. That is, critical current density can be controlled by making the geometric pinning landscape. In a word, we proposed a scenario of how to control the tunable vortex lattice induced by external magnetic fields and has been confirmed unambiguously by the experiment. Such a scenario shows great potentials in promotion of large-scale applications of the type-II superconductor.

In addition to the exploration performed from the material science, we also studied the superimposed effect of the superconducting material by assembling bulks and tapes into hybrid magnet in the last section. New perspective of engineering high trapped flux performance was proposed and key factors were clarified. The bulks assembled with the stacked coated superconductor could replace the melt-textured bulks with many advantages when the superconducting volume ratio is high enough without deterioration its current-carrying ability and with low cost. In addition to improve the current-carrying performance of each kind of material, making hybrid magnet could be adopted alternatively as a compromising strategy.

7.2 Future perspectives

Based on our findings, mixed results of vortex pinning emerged in the past decades could be clarified. Practical strategy of how to make geometric superconducting pin arrays could be extending further by which one could achieve variety of curves in the J_c - B diagram to meet the requirement of different superconducting devices. The biggest challenge on making the geometric pinning landscape lies imaginably in the synthesis technique of superconducting nanoparticles as well as the relevant technique of how to arrange them conveniently into geometric patterns. Whereas the best way currently is to exploit grain boundaries since crystal growth naturally provides the “ordered channels” and the “ordered driving forces” in nano-scale and simultaneously favors to meet the requirement of large-scale engineering. Our original consideration is to make the possible superconducting super-lattices with different chemical potentials to meet the requirement of rasterized vortices. If this consideration could be turned into reality, the ultimate high current-carrying ability could be achieved persistently. At present, engineering the grid-like superconducting nanowalls in tapes or wires is worth doing. Because deposit techniques and coated techniques allow one to engineer simultaneously different kind superconductors. Be means of such experimental design, high critical current density could be maintained from self-field to high magnetic field which is considerably to extend the broad applicability of superconductors in practical applications.

Acknowledgements

I am especially thankful to Prof. Mitsuru Izumi at Tokyo University of Marine Science and Technology. This work has been accomplished under his kind guidance and support. His help and support are not limited in my study, but also extended to my daily life in Japan. Thanks to him, I could accomplish my thesis within three years. A special thank goes to the Institute for Solid State Physics (ISSP), The University of Tokyo, where SEM and SQUID measurements could be conducted. I am grateful to the Grant-in-Aid for Scientific Research (B) (KAKENHI, Grant No. 21360425 and No. 2311003). I also would like to express my appreciation to Nippon Steel & Sumitomo Metal.

I would like to thank my thesis referees, Prof. M. Shima, Prof. K. Iwamoto and Prof. H. Ohnuki from Tokyo University of Marine Science and Technology for a review and qualification of my thesis and giving valuable comments.

I would like to thank the support from Dr. D. Hamane and Mr. T. Yamauchi for the joint research activity in ISSP, The University of Tokyo.

Thanks my colleagues of Laboratory of Applied Physics, Tokyo University of Marine Science and Technology, Dr. Y. Zhang (Shanghai University of Electric Power), Dr. Caixuan Xu (GE Momentive Co. Ltd.), Dr. Y. Xu (Shanghai University of Electric Power), Dr. K. Xu (Qujing Normal University), Dr. H. Wang (The University of Tokyo) graduated several years ago, for their advice and help through the study and life in Japan. I would like to thanks Mr. S. Hara, Mr. D. Zhou, Dr. K. Tsuzuki, Dr. Z. Deng, Dr. B. Felder, Dr. M. Miki and other students for their kind advice and assistance both in my studies and life in Japan. Thanks all the people who give me help in the past three years.

Finally, I would like to express a deep appreciation to my parents, my brothers, my sisters, my wife and other members of my family. They gave me continuous encouragement and valuable suggestion in my life and study during last three years in Japan.

List of Publications

1) **Beizhan Li**, Kun Xu, Shogo Hara, Difan Zhou, Yufeng Zhang, Mitsuru Izumi, "Enhanced pinning effect in air-processed Gd-123 bulk superconductors with $BaTiO_3$ addition", ***Physica C*** 475, 51-56 (2012).

2) **Beizhan Li**, Difan Zhou, Kun Xu, Shogo Hara, Keita Tsuzuki, Motohiro Miki, Brice Felder, Zigang Deng and Mitsuru Izumi, "Materials process and applications of single grain (RE)–Ba–Cu–O bulk high-temperature superconductors", ***Physica C*** 482, 50-57 (2012).

3) **Beizhan Li**, Kun Xu, Shogo Hara, Difan Zhou, Mitsuru Izumi, "TiO_2 doping effect on flux pinning properties of bulk $GdBa_2Cu_3O_{7-\delta}$ superconductors", ***Physica C*** 484, 112-116 (2013).

4) **Beizhan Li**, Difan Zhou, Shogo Hara, Kun Xu and Mitsuru Izumi, "The effect of recrystallization of fine inclusions on the enhancement of flux pinning in textured Gd-Ba-Cu-O bulk superconductors", ***IEEE Trans. Appl. Supercond.*** 23, 8001804 (2013).

5) **Beizhan Li**, Difan Zhou, Kun Xu, Keita Tsuzuki, Jincang Zhang and Mitsuru Izumi, "Flux pinning behaviors of textured Gd-Ba-Cu-O superconductor mediated by the additions of $BaTiO_3$, TiO_2 and BaO_2", ***Physica C*** 2013 (already published online, DOI: 10.1016/j.physc.2013.06.017)

6) **Beizhan Li**, Jincang Zhang, Mitsuru Izumi, "Grid-like Nanowalls Formed by Inserting Nanoparticles into Grain Boundaries in Gd-Ba-Cu-O Bulk Superconductor in textured Gd-Ba-Cu-O bulk superconductor", ***Science*** 2013 (submitted)

7) Difan Zhou, **Beizhan Li**, Shogo Hara, Kun Xu, Keita Tsuzuki, Motohiro Miki, Brice Felder, Mitsuru Izumi, "Process Technology and Superconducting Properties of Bulk HTS With Multi-RE Elements" ***IEEE Trans. Appl. Supercond.*** 23, 6800104 (2013).

8) Difan Zhou, Shogo Hara, **Beizhan Li**, Kun Xu, Jacques Noudem, and Mitsuru Izumi, "Significant improvement of trapped flux in bulk Gd-Ba-Cu-O grains fabricated by a modified top-seeded melt growth process", ***Supercond. Sci. Technol.*** 26, 015003 (2013).

9) Hara Shogo, Difan Zhou, **Beizhan Li**, Mitsuru Izumi, "Doping Effect of Fe-Ni Alloy Particles on Flux Pinning in Gd-Ba-Cu-O Bulk Superconductor" ***IEEE Trans. Appl. Supercond.*** 23, 7200804 (2013).

10) Difan Zhou, Kun Xu, Shogo Hara, **Beizhan Li**, Zigang Deng, Keita Tsuzuki, and Mitsuru Izumi, "MgO buffer-layer-induced texture growth of RE-Ba-Cu-O bulk", ***Supercond. Sci. Technol.*** 25, 025022 (2012).

11) Kun Xu, Difan Zhou, **Beizhan Li**, Shogo Hara, Keita Tsuzuki, Yufeng Zhang, Yan Xu, Mitsuru Izumi, "Superconductivity: Recent Developments and New Production Technologies; Chapter 5", ***Nova Science***, (2012).

12) Kun Xu, Difan Zhou, **Beizhan Li**, Shogo Hara, and Mitsuru Izumi, "Investigation of microstructure and superconducting properties in the Fe-B magnetic particles doped $GdBa_2Cu_3O_{7-\delta}/Ag_2O$ and $GdBa_2Cu_3O_{7-\delta}$/nano-Ag superconducting bulks", ***Physics Procedia*** 36, 557-562 (2012).

List of Presentations

1) Applied superconductivity conference, **Beizhan Li,** poster presentation, "Effect of recrystallization of impurities on the enhancement of flux pinning in textured Gd-Ba-Cu-O bulk superconductors", Portland, ***U.S.A***, October 7-12, 2012.
2) 24th international symposium on superconductivity, **Beizhan Li,** poster presentation, "TiO_2 addition effect on flux pinning properties of bulk $GdBa_2Cu_3O_{7-\delta}$ superconductors", Tokyo, ***Japan***, Octorber 24-26, 2011.
3) 23th international symposium on superconductivity, **Beizhan Li,** no presentation, Tsukuba, ***Japan***, November 1-3, 2010.
4) The 6^{th} international conference on the physical properties and applications of advanced materials, **Beizhan Li,** poster presentation, "a more effective dopant for enhancement of flux pinning in air-processed Gd123 bulk superconductors compare with the doping effect of TiO_2", Shanghai, ***China***, October 11-15, 2011